MAGNETOHYDRODYNAMIC SHOCKS NEAR ROTATING BLACK HOLES

by

Darrell Jon Rilett

A dissertation submitted in partial fulfillment
of the requirements for the degree

of

Doctor of Philosophy

in

Physics

MONTANA STATE UNIVERSITY — BOZEMAN
Bozeman, Montana

November 2003

© Copyright

by

Darrell Jon Rilett

2003

All Rights Reserved.

APPROVAL

of a dissertation submitted by

Darrell Jon Rilett

This dissertation has been read by each member of the dissertation committee, and has been found to be satisfactory regarding content, English usage, format, citations, bibliographic style and consistency, and is ready for submission to the College of Graduate Studies.

Sachiko Tsuruta, Ph. D.

Approved for the Department of Physics

William A. Hiscock, Ph. D.

Approved for the College of Graduate Studies

Bruce R. McLeod, Ph. D.

STATEMENT OF PERMISSION TO USE

In presenting this dissertation in partial fulfillment of the requirements for a doctoral degree at Montana State University — Bozeman, I agree that the Library shall make it available to borrowers under rules of the Library. I further agree that copying of this thesis is allowable only for scholarly purposes, consistent with "fair use" as prescribed in the U. S. Copyright Law. Requests for extensive copying or reproduction of this thesis should be referred to University Microfilms International, 300 North Zeeb Road, Ann Arbor, Michigan, 48106, to whom I have granted "the exclusive right to reproduce and distribute my dissertation in and from microform along with the non-exclusive right to reproduce and distribute my abstract in any format in whole or in part."

Signature _____

Date _____

ACKNOWLEDGEMENTS

I would like to thank the following individuals:

Dr. Sachiko Tsuruta, for having the patience to tolerate me and guide me through the process; Dr. Masaaki Takahashi, the source of knowledge for this topic and without whom this dissertation would not exist; Keigo Fukumura, for countless discussions, questions to which I had no answers, initially, and for the never ending independent code checks; Dr. William Hiscock and Dr. Joseph Dreitlein, archetypes for "Physicist" and valuable sources of inspiration and motivation, without knowing it; Dr. Gregory Reinemer, longtime friend, who allowed me to watch his long and painful dissertation process; his insights and perseverance gave me hope in my own efforts; my committee members, all nine of them, for knocking down bureaucratic walls; Margaret Jarrett, Rose Waldon, and Jeannie Gunderson, who took care of administrative details so I didn't have to; finally, my thanks to Annie, who came last and now is first.

TABLE OF CONTENTS

1. INTRODUCTION 1

A Brief Overview of AGN 1

2. DEVELOPMENT OF THE SHOCK EQUATIONS 10

Introduction 10
Basic Equations of General Relativistic Plasma Flow 10
The Conditions for MHD Accretion Onto a Kerr Black Hole 19
Relativistic Bernoulli equation 21
Split-Monopole Field 23
Light Surfaces 24
Inner and Outer Alfvén Radius 26
Fast and Slow Magnetosonic Points 28
Injection and Separation Points 30
Types of MHD Shocks 33
MHD Shocks in Kerr Geometry 33
The Jump Conditions 34
Dimensionless Parameters and Their Relations 38

3. CATEGORIZATION OF MHD SHOCKS 46

Introduction 46
The ξ vs. ζ Parameter Space 47
Slow Magnetosonic Shocks 48
Fast Magnetosonic Shocks 52
Types of Accretion Flows 53

4. SLOW MAGNETOSONIC SHOCKS IN THE EQUATORIAL PLANE 64

Introduction 64
Effects of Black Hole Spin 65
Magnetization Effects 79
Type II Shocks 83
Type III Shocks 85
Asymptotic Limit 87
Summary 89

5. SLOW MAGNETOSONIC SHOCKS IN THE POLAR REGION 91

Introduction 91
Behavior of Critical Points 92
Shocks Near The Polar Axis 100
Angular Momentum Distribution 101

TABLE OF CONTENTS – CONTINUED

6. SWITCH-OFF SHOCKS AND MULTIPLE ALFVÉN POINT FLOWS 109

Introduction 109
Multiple Inner Alfvén Points 109
Switch-Off Shocks 118

7. FAST MAGNETOSONIC SHOCKS 126

Introduction 126
Fast Shock Results 127
Comparison with Previous Results 130

8. CONCLUSION 137

Summary 137
Future Work 138

APPENDICES 141

A. Derivation of Type II Shock Properties 142
B. Switch-off Shocks 146
C. Kerr Spacetime, ZAMO's and Units 148

BIBLIOGRAPHY 153

LIST OF TABLES

Table		Page
2.1	Types of MHD Shocks: Fast, Slow and Intermediate	33
3.1	Slow shock categories for positive black hole spin	61
3.2	Additional relationships for slow shock categories, positive spin	61
3.3	Slow shock categories for negative black hole spin	62
3.4	Additional relationships for slow shock categories, negative spin	62
3.5	Fast shock categories for positive black hole spin	62
3.6	Additional relationships for fast shock categories, positive spin	63
4.1	Conserved Flow Parameters	67
4.2	Important Radial Locations	67
4.3	Parameter set for seven cold trans-fast MHD accretion solutions, variable spin	68
4.4	Parameter set for a magnetically dominated Type I accretion solution	82
4.5	Parameter set for similar Type I flows but different magnetic energy components	83
4.6	Parameter set for seven Type II flows, all subcategories	85
4.7	Parameter set for Type III MHD accretion solutions	87
4.8	Parameter set for cold trans-fast MHD accretion solutions in the asymptotic limit	89
6.1	Initial data and critical points for two MIAP accretion flows	111
6.2	Parameter set for Type I MIAP shocks	116
6.3	Comparison of switch-off shock to general shock	125

LIST OF FIGURES

Figure Page

2.1 Friedrichs diagram of the three plasma wave velocities 20

2.2 Preshock cold trans-fast MHD accretion solution 23

2.3 Schematic of Typical Inflow and Outflow 32

2.4 Accretion flows with a shock front 34

2.5 Illustrations of slow and fast shocks in the M^2 vs. r plane 45

3.1 Shock Category: ξ vs. ζ for slow shock, Case 1 49

3.2 Shock Category: ξ vs. ζ for slow shock, Case 2 50

3.3 Shock Category: ξ vs. ζ for slow shock, Case 3 51

3.4 Shock Category: ξ vs. ζ for fast shock, Case 5 53

3.5 Shock Category: ξ vs. ζ for fast shock, Case 6 54

3.6 Maximum and minimum Ω_F and flow types 56

3.7 Relation of $\Omega_F \tilde{L}$ to r_A for Type I and III flows 56

3.8 Relation of $\Omega_F \tilde{L}$ to r_A for Type II flows 57

4.1 Polytropic index as a function of temperature 66

4.2 Fractional error in Service's approximation to the polytropic index 66

4.3 The compression ratio as a function of preshock radial velocity 69

4.4 The polytropic index as a function of preshock radial velocity 70

4.5 The number density ratio for Type I and VI shocks 71

4.6 The time-component four-velocity ratios for Type I and VI shocks 71

LIST OF FIGURES – CONTINUED

Figure Page

4.7 Alfvén Mach number ratio for Table 4.3 shocks 73

4.8 ζ vs. radial velocity for Table 4.3 shocks 73

4.9 Preshock magnetization vs. radial velocity for Table 4.3 shocks 74

4.10 Preshock specific angular momentum for Table 4.3 shocks 75

4.11 Temperature of the postshock flow 75

4.12 Preshock ZAMO azimuthal magnetic field vs. shock location 76

4.13 Postshock ZAMO azimuthal magnetic field vs. shock location 77

4.14 Energy of the accreting flow, in the ZAMO frame 78

4.15 Preshock magnetic energy fraction in the ZAMO frame 79

4.16 Postshock magnetic energy fraction in the ZAMO frame 80

4.17 Preshock plasma toroidal velocity in the ZAMO frame 80

4.18 Postshock plasma toroidal velocity in the ZAMO frame 81

4.19 Large magnetization slow shock example 82

4.20 Varying magnetization slow shock example 84

4.21 Type II slow shock solutions - compression ratio 86

4.22 Type II slow shock solutions - toroidal velocity 86

4.23 Type II slow shock solutions - magnetization 87

4.24 Type III slow shock solutions 88

4.25 Asymptotic Limit: ξ, Γ, and Θ 89

5.1 Polar plots of r_L, r_A and $r_{\rm sp}$ for Type I flows 96

LIST OF FIGURES – CONTINUED

Figure Page

5.2 Polar plots of r_L, r_A and $r_{\rm sp}$ for Type IIa flows 97

5.3 Polar plots of r_L, r_A and $r_{\rm sp}$ for Type IIb flows 98

5.4 Polar plots of r_L, r_A and $r_{\rm sp}$ for Type IIc flows 98

5.5 Polar plots of r_L, r_A and $r_{\rm sp}$ for Type III flows 99

5.6 Maximum Ω_F for $a = 0.7$ 101

5.7 First examples of polar shocks 102

5.8 Example of strong polar shock 103

5.9 Critical points for angular momentum distribution $\tilde{L} = 2.5 \sin^2 \theta$ 106

5.10 Critical points for angular momentum distribution $\tilde{L} = 4.56 \sin^2 \theta$ 107

5.11 Polar plot showing magneto- to hydro- dominated flow 108

6.1 Wind equation solution for MIAP flows 112

6.2 The $N = 0$ and $D = 0$ curves for MIAP flows 112

6.3 Close-up if MIAP flow at inner Alfvén point 113

6.4 Close-up if MIAP flow at outer Alfvén point 113

6.5 Example of MIAP shocks 114

6.6 Additional results for MIAP shocks 115

6.7 Compression ratio for two MIAP shocks, varying E and L 117

6.8 Postshock temperature for two MIAP shocks, varying E and L 117

6.9 Parameter space for switch-off shocks 124

7.1 Fast shock: ξ vs. radial velocity 131

LIST OF FIGURES – CONTINUED

Figure Page

7.2 Fast shock: Preshock magnetization 132

7.3 Fast shock: amplification of toroidal magnetic field 133

7.4 Fast shock: Preshock magnetic energy 134

7.5 Fast shock: Postshock temperature 134

7.6 Fast shock: Polytropic index 135

CONVENTIONS

Natural units are used throughout this dissertation, where $c = G = k_B = \hbar = 1$, except where otherwise noted. In addition, the black hole mass and fluid particle mass are both set equal to one. When conventional units are required, SI (*Systéme International*) units will be employed. Rules and style conventions for printing and using units will also follow the SI, according to Taylor (1995).

The metric signature is -2. For all spacetime tensor indices, Greek indices range over temporal and spatial coordinates, taking the values 0 to 3; Latin indices range over only the spatial coordinates, 1 to 3. The Einstein summation convention is use throughout, with repeated indices summed over. The semi-colon is used to denote the metric compatible covariant derivative, e.g.

$$F^{\alpha}_{\ \beta;\nu} = F^{\alpha}_{\ \beta,\nu} + \Gamma^{\alpha}_{\lambda\nu} F^{\lambda}_{\ \beta} - \Gamma^{\lambda}_{\beta\nu} F^{\alpha}_{\ \lambda} \ ,$$

where

$$\Gamma^{\alpha}_{\mu\nu} = \frac{1}{2} g^{\alpha\beta} (g_{\beta\mu,\nu} + g_{\beta\nu,\mu} - g_{\mu\nu,\beta})$$

and the comma represents the usual partial derivative. The anti-symmetry operator is defined by

$$T_{[\mu\nu]} = \frac{1}{2} (T_{\mu\nu} - T_{\nu\mu}) \ .$$

ABSTRACT

The theory of general relativistic magnetohydrodynamic standing shock formation is analyzed for accreting MHD plasma in a rotating, stationary, and axisymmetric black hole magnetosphere. All postshock physical quantities are expressed in terms of the relativistic compression ratio. The compression ratio is a solution of a seventh degree polynomial, incorporating the jump conditions, that is to be solved simultaneously with an equation for the polytropic index of the postshock plasma. Then the downstream state of the shocked plasma is determined entirely in terms of preshock quantities. Slow and fast magnetosonic shock solutions are analyzed for both equatorial and non-equatorial accretion flows. Shock categories for fast and slow shocks are developed, based on conserved quantities. These categories relate the initial conditions of a preshock flow to the spin of the black hole and can be used as a predictor of shock strength and location. We show that shocks may produce a hot region close to the horizon that could be applied to the generation mechanism of the iron fluorescence line from a Seyfert nucleus.

CHAPTER 1

INTRODUCTION

'All the models have a massive object at the center, such as a black hole, and an accretion disk and polar outflow, but the detailed shape and arrangement of these things are still being worked on.' – David Westpfahl

A Brief Overview of AGN

There are estimated to be approximately 130 billion galaxies in our universe. Most of these galaxies have at their center a supermassive black hole (SMBH). The term SMBH generally refers to black holes with a mass greater than $10^5 M_\odot$. When a SMBH accretes material, a substantial fraction of the gravitational binding energy of the infalling matter can be radiated away. The nucleus of the galaxy then increases enormously in luminosity and becomes visible as a so-called AGN, or active galactic nucleus. Compelling theoretical arguments support this idea of an AGN being powered by accretion of matter onto a SMBH (Rees 1998). Observational evidence includes water maser mappings with the VBLA (Very Long Baseline Array) and kinematical gas analyses with HST (The Hubble Space Telescope) (e.g., Kormendy & Richstone 1995 and references therein). Maia, Machado & Willmer (2002) report that a survey of the local universe determined that 2.6% of galaxies host AGNs. According to the "standard unified scenario" an AGN reveals itself as either a quasar or a Seyfert nucleus[1] during the early stages of its lifetime when the

[1] A Seyfert galaxy consists of a bright nucleus characterized by a non-stellar continuum and high ionization emission lines.

accretion rate is high and the black hole is spinning up.[2] In later stages, when the rate of accretion decreases and the black hole begins losing its rotational energy by spinning down, it evolves to a radio galaxy (see Moderski & Sikora 1996 for a discussion of SMBH hole spin evolution).

A major component of the AGN engine is thought to be a magnetosphere surrounding the SMBH. Early work on magnetic field configurations around black holes was done by several authors (Wald 1974; King, Lasota & Kundt 1975; Karas 1989). The magnetohydrodynamic (MHD) flow around a black hole has been studied using analytical methods (Phinney 1983; Camenzind 1986a; Camenzind 1986b; Camenzind 1987; Punsly & Coroniti 1990a; Punsly & Coroniti 1990b). In the early 1990s, Takahashi et al. (1990, hereafter TNTT90), Nitta, Takahashi & Tomimatsu (1991) and Hirotani et al. (1992) investigated both inflow and outflow of material in black hole magnetospheres. Their approach was a unified general relativistic MHD description of both the matter accretion process and the electromagnetic process in the magnetosphere. Relaxing the force-free limit, these authors explored the roles of interactions between the accreting fluid matter and electromagnetic fields.

For winds and jets, the Weber-Davis model applicable to neutron star magnetospheres was modified for black holes (Weber & Davis 1967; Sakurai 1985; Fendt & Greiner 2001). These models all assume some magnetic field configuration; recently Khanna (1998b) has specifically addressed the generation of magnetic fields in the vicinity of black holes. Yokosawa (1993) numerically calculated the dynamical evolution of MHD accretion in a

[2]The theoretical maximum spin is $a = 1$, the astrophysical limit, due to captured radiation emitted from an accretion disk, is $a \approx 0.998$, (Thorne 1974). But Gammie, Shapiro & McKinney (2003) have shown that the inclusion of MHD effects may give a maximum spin of $a \approx 0.9$.

Kerr space-time with a weak-field limit.

The idea of using the rotational energy of a black hole to power a wind was examined by Ruffini & Wilson (1975). These authors assumed the weak magnetic field limit, allowing the plasma motion to be geodesic. A limitation of this model is that it was very inefficient at extracting energy. The so-called "BZ-model," in which the magnetic field dominated the dynamics, addressed this problem (Blandford & Znajek 1977; Znajek 1977; Thorne, Price & Macdonald 1986; see, e.g., Begelman, Blandford & Rees 1984 for a comprehensive review). The BZ model has been a popular and widely researched mechanism for extracting a black hole's energy. But see Punsly (2001) and references therein for detailed arguments claiming its failure, Komissarov (2001) for counterarguments and Punsly (2003) for a rebuttal.

Nevertheless, the BZ model has been an important step in understanding the magnetosphere in the Kerr background space-time using the force-free limit. For example, Okamoto (1992) studied the evolution of force-free black hole magnetospheres including extraction of the black hole's rotational energy via the BZ process. The next logical step was to extend these magnetospheric studies to accretion-powered AGNs—especially to Seyfert nuclei where the accretion rate is relatively moderate. Recent observations of a Seyfert galaxy (Wilms et al. 2001) have been interpreted as direct evidence of energy extraction from a spinning black hole via magnetic fields. Koide (2003) has done numerical simulations indicating a new mechanism for magnetic extraction of a black hole's rotational energy via a torsional Alfvén wave.

X-ray irradiation of relatively cold material in the vicinity of a black hole provides a useful probe of the region very close to the horizon. Detailed X-ray spectroscopy of

AGN have revealed important characteristic features, particularly the Kα fluorescent line of iron. For a comprehensive review of relativistic iron line studies for both accreting stellar mass black holes and accreting supermassive black holes see Reynolds & Nowak (2003). Recent *ASCA*[3] observations have provided evidence that the iron lines observed from some Seyfert nuclei are emitted from regions very close to the central black hole (e.g., Tanaka et al. 1995; Nandra et al. 1997).

Iwasawa et al. (1996) interpreted the behavior of the Seyfert galaxy MCG 6-30-15, deduced from a long *ASCA* observation, as an indication that the black hole is rotating extremely fast, near the maximum limit. Reynolds & Begelman (1997) pointed out that such an extremely fast rotation contradicts the standard unified scenario. Instead, these authors showed that if an X-ray point source located somewhere above the hole on the rotation axis illuminates the infalling gas within the inner accretion disk radius, a Schwarzschild (or low spin) hole is consistent with that observation. However, the mechanism for generating these X-rays was left unspecified. More recently, Wilms et al. (2001), with new data from *XMM-Newton*[4], concluded that MCG 6-30-15 must posses a rapidly rotating black hole. In their model the source of the X-ray illumination was the disk corona.

The disk-corona connection has been investigated thoroughly. Haardt & Maraschi (1993) modelled the X-ray emission from radio-quiet AGN. They found that X-rays are produced via inverse Compton emission in a hot corona embedding a colder accretion disk. Maraschi & Haardt (1996) reviewed the current status of disk-corona models and discussed

[3]The Advanced Satellite for Cosmology and Astrophysics. Japan's fourth cosmic X-ray satellite, launched in 1993.

[4]The European Space Agency's X-ray Multi-Mirror satellite.

the dependence of the X-ray spectrum on the coronal parameters. A difficulty with the coronal model is that a thermal, Maxwellian distribution is assumed. But particle-particle collisions are rare in the hot, low-density corona. Ghisellini, Haardt & Svensson (1998) address this by assuming cyclo-synchrotron absorption as the thermalization mechanism. Petrucci (2001) point out that simple slab-corona models fail to fit the observed X-ray spectra. Recently, Merloni & Fabian (2003) attempted to address the problem with corona models by investigating the inner boundary condition on the accretion disk and its effect on the coronal emissivity profile.

These issues clearly point to the importance of investigating, for accretion-powered AGNs also, the basic physics in the vicinity very close to a black hole—especially the regions between the inner boundary of the accretion disk and the event horizon. As a first step toward such an investigation, therefore, we explore MHD shock formation in accreting plasma in black hole magnetospheres. These studies may provide valuable insight to problems such as how X-ray sources can be created near the event horizon.

Hydrodynamic shocks around black holes have been investigated numerically (Wilson, 1972; Chang & Ostriker, 1985) and analytically (Lu et al., 1997; Lu & Yuan, 1998). Classical studies of spherical accretion in the adiabatic limit (Bondi, 1952) do not admit shocks (McCrea, 1956). However, preheating of the infalling gas by radiation from below (Chang & Ostriker, 1985) can alter the properties of the infalling gas and allow for shocks. Babul, Ostriker & Mészáros (1989) proposed a standing hydrodynamic shock model for the radiation mechanism of the hard X-rays and γ-rays in quasars.

The path to MHD shocks in a Kerr spacetime began with de Hoffman & Teller (1950), who first derived the analogues of the Rankine-Hugoniot equations for an infinitely con-

ducting fluid. Helfer (1953) followed with a systematic interpretation of their results and demonstrated that weak magnetic fields in interstellar clouds will be amplified. Strong fast magnetosonic MHD shocks in the Crab nebula wind were analyzed by Kennel & Coroniti (1984). Camenzind's series of papers, cited above, culminated in a derivation of special relativistic MHD shock relations for magnetized jets (Appl & Camenzind 1988, hereafter AC88). It is their work that has been specialized to accreting flows in the Kerr spacetime, a much more complicated situation. Recently, Yokosawa (1994) performed numerical calculations on the formation processes of shock waves in MHD accretion. Yokosowa concluded that shock waves formed in the vicinity of the event horizon may produce a large amount of X-ray emission.

We consider the central engine of an AGN to be a rotating black hole surrounded by a magnetosphere, where accreting plasma and outgoing winds/jets are assumed to exist. We formulate the MHD shock conditions in the Kerr geometry for such plasma. The formation of shocks in the accreting flow is dependent upon the existence of multimagnetosonic points, while for outgoing plasma a submagnetosonic solution is allowable. This is because, for instance, the accreting flows initially ejected from the plasma source with low velocity must be terminally superfast magnetosonic at the event horizon. At the shock front, the flow transits from super-magnetosonic to sub-magnetosonic, so that the accreting flows undergoing a shock must pass through a magnetosonic point on each side of the shock front. This situation is quite similar to the case of hydrodynamical accretion onto a black hole (e.g., Chakrabarti 1990a; Sponholz & Molteni 1994; Lu et al. 1997; Lu & Yuan 1998).

The transmagnetosonic MHD flow solution was discussed by Takahashi (2000a). Along a magnetic field line, five physical quantities are conserved: the total energy E, the angular

momentum L, the angular frequency of the magnetic field line Ω_F, the particle number flux per magnetic flux tube η, and the entropy S (see, e.g., Camenzind 1986a). When these conserved quantities are specified at the plasma source, the location of the fast/slow magnetosonic points and the Alfvén point are determined.

Takahashi (2000a) obtained multi-magnetosonic point solutions and found two regimes of accretion flows—'hydro-like' and 'magneto-like'. The hydro-like accretion would transit to magneto-like accretion by shock formation. However, we postpone the problem of joining these two types of solutions across a shock front. The reason is that in order to do so we would have to carry out a detailed parameter search for trans-magnetosonic MHD flows. That is, a matching set of five physical field-aligned quantities in both upstream and downstream solutions would need to be determined—not a trivial situation.

This work is meant as a starting point for our long-range investigation of shock conditions for accretion flows in the Kerr geometry. Therefore, here we will only solve the cold trans-fast MHD equations for upstream accretion and discuss the shock properties at the shock fronts. Because the plasma is heated up at the shock front, the postshock accretion should be treated by a hot MHD accretion model (Takahashi 2002). This research will not solve explicitly the hot trans-magnetosonic solutions for postshock accretion but instead treat the shock front location as a free parameter. However, by joining the preshock and postshock solutions, the shock location will be severely restricted.

The main purpose of this research is to explore the effects of rotation and general relativity on the MHD shock conditions for accreting plasma in a black hole magnetosphere. In order to do so, we present in Chapter 2 the basic equations for MHD accretion in the Kerr geometry. Then we extend the work for special relativistic MHD jets by AC88, by

deriving the shock conditions for general relativistic MHD accretion onto a Kerr black hole. As the next step, our shock conditions are applied to the accreting MHD plasma flows as described in detail by TNTT90. Following AC88, all of our postshock physical quantities are expressed in terms of the relativistic compression ratio, ξ. This compression ratio is the solution of a polynomial of seventh degree. Due to the additional factors, namely black hole rotation and general relativistic effects, the mechanism of solution is far more complicated and tedious than in AC88.

In Chapter 3, before presenting shock solutions, we derive various categories of shock solutions as a function of the parameter space consisting of the conserved quantities, black hole attributes and specified magnetosphere. The categories depend on the allowed flow types given by TNTT90 and a simple quadratic equation in the compression ratio. The shock categories not only lend predictive capabilities without the need for extensive computations, they also aid in the numerical search for solutions.

In Chapter 4 we present some examples of representative physically relevant shock solutions found for acceptable accretion flows onto the event horizon. Our results are presented for equatorial flows and slow magnetosonic shocks. Since for the cold case the injected preshock accretion is super-slow magnetosonic in any case, we can consider only the shock conditions, without considering the critical condition for the slow magnetosonic point. Generalizing to non-equatorial flows, polar shocks are discussed in Chapter 5. Because shocks are a local phenomenon, shocks near the rotation axis are not qualitatively different than equatorial shocks. But the types of shocks allowed and the shock location are both very much a function of the polar angle.

Two special situations in MHD shock formation are considered in Chapter 6: switch-off

shocks and multiple Alfvén point flows. A switch-off shock, in which the postshock toroidal magnetic field component vanishes, occurs at the Alfvén point. An analysis of the jump conditions evaluated at the Alfvén point results in a simplified "fifth" degree equation in the compression ratio, ξ_A. Then a comparison is made between switch-off shocks and similar, normal slow shocks occurring very close to the Alfvén point. A non-trivial aspect of MHD accreting flows is the possibility of two inner Alfvén radii under certain conditions. Given these circumstances, the adjustment of just one conserved quantity selects which Alfvén radius becomes the Alfvén point. The type of shock that forms is then very sensitive to only one parameter.

Most of this research applies to slow magnetosonic shocks. But the derivation in Chapter 2 makes no distinction on the kind of shock allowed. It follows that with moderate adjustment in the numerical code, fast magnetosonic shocks can also be investigated. This we do in Chapter 7, albeit rather briefly. Fast shocks will generally take place quite close to the horizon and, based on the category analysis of Chapter 3, tend to be rather weak. Finally, a summary of our results and a discussion of future work is presented in Chapter 8.

CHAPTER 2

DEVELOPMENT OF THE SHOCK EQUATIONS

'A child of five could understand this. Fetch me a child of five.' – Unknown

Introduction

Before we can discuss the behavior of MHD shocks around SMBHs we need to develop a model for such shocks. Before we can develop a theory of shocks we need to know the conditions for plasma accretion onto a black hole. Before we can state the conditions for plasma accretion we need to express the physics of general relativistic MHD flow. Due to the extreme complexity of the physics, we will make many simplifying assumptions in the development of our model. These assumptions permit five conserved quantities in the model—an asset that will be used to full advantage.

Basic Equations of General Relativistic Plasma Flow

In this section we summarize the basic equations pertaining to MHD flows in Kerr geometry. This formulation is a general-relativistic extension of the Newtonian Weber-Davis model (Weber & Davis, 1967) and special-relativistic wind model by Kennel, Fujimura & Okamoto (1983). It was first derived by Takahashi et al. (1990) and different aspects have been explored in (Nitta, Takahashi & Tomimatsu 1991; Hirotani et al. 1992; Punsly 2001; Takahashi 2002). Although specializing to the Schwarzschild metric would be simpler, it is expected that Kerr black holes are more relevant for astrophysics. In any event, we

can always take the Schwarzschild limit if we like. A stationary and axisymmetric magnetosphere, aligned with the spin axis of the black hole is assumed. This will allow us to take advantage of the globally conserved quantities, energy and angular momentum. The flow's self-gravity is ignored: the flow is certainly too tenuous to have any effect on curvature and its self-gravity will be much weaker than magnetic forces. The one-fluid approximation is assumed; see Khanna (1998a) for an MHD description of a two-component plasma in the Kerr metric. We also require infinite conductivity for the plasma flow. The background metric is given by the Boyer-Lindquist coordinates, setting $c = G = 1$,

$$\begin{aligned} ds^2 &= \left(1 - \frac{2mr}{\Sigma}\right) dt^2 + \frac{4amr\sin^2\theta}{\Sigma} dt\, d\phi \\ &\quad - \left(r^2 + a^2 + \frac{2a^2 mr\sin^2\theta}{\Sigma}\right)\sin^2\theta\, d\phi^2 - \frac{\Sigma}{\Delta}\, dr^2 - \Sigma\, d\theta^2 \ , \end{aligned} \tag{2.1}$$

where $\Delta \equiv r^2 - 2mr + a^2$, $\Sigma \equiv r^2 + a^2\cos^2\theta$, and m and a denote the mass and angular momentum per unit mass (spin) of the black hole, respectively. For the remainder of this dissertation, the black hole mass will be set to one ($m = 1$) and the radial distance (r) will be scaled by the black hole mass. The black hole spin will also be scaled by the mass. Occasionally, such as the following equation, the "m" will be explicitly shown, for clarity. In these coordinates the symmetries defined by the two Killing vector fields $\vec{\kappa} = \partial_t$ and $\vec{\chi} = \partial_\phi$ are manifest. The existence of the Killing fields $\vec{\kappa}$ and $\vec{\chi}$, representing stationarity and axisymmetry of the spacetime lead to two conserved quantities, energy and angular momentum (Wald 1984). There are two event horizons, given by the roots of the equation

$\Delta = 0$. The outer horizon, r_H is given by

$$r_H = m + \sqrt{m^2 - a^2} \ . \tag{2.2}$$

The static limit, or outer boundary of the ergosphere, is the solution of $g_{tt} = 0$ and given by

$$r_{\rm st} = m + \sqrt{m^2 - a^2 \cos^2 \theta} \ . \tag{2.3}$$

The motion of magnetized plasma around a black hole is obtained from the equations of motion (conservation of total energy and momentum):

$$T^{\alpha\beta}_{\ \ ;\beta} = 0 \ , \tag{2.4}$$

where the energy-momentum tensor for a perfect fluid is the sum of a fluid part

$$T^{\alpha\beta}_{\rm fl} = (\rho + P) u^\alpha u^\beta - P g^{\alpha\beta} \ , \tag{2.5}$$

and an electromagnetic part

$$T^{\alpha\beta}_{\rm em} = \frac{1}{4\pi} \left(F^\alpha_{\ \lambda} F^{\lambda\beta} + \frac{1}{4} g^{\alpha\beta} F^2 \right) \ , \tag{2.6}$$

and $F^2 = F^{\alpha\beta} F_{\alpha\beta}$. The fluid is perfect in the sense that dissipative effects, such as heat conduction and viscosity, are neglected. Here, ρ and P are the total energy density and the pressure of the plasma, respectively. The electromagnetic field $F^{\alpha\beta}$ satisfies Maxwell's

equations

$$F_{[\alpha\beta;\delta]} = 0 \ , \tag{2.7}$$

$$F^{\alpha\beta}{}_{;\beta} = -4\pi j^{\alpha} \ , \tag{2.8}$$

with j^{α} the electric 4-current. The flow obeys the conservation law for particle number:

$$(nu^{\alpha})_{;\alpha} = 0 \ , \tag{2.9}$$

where n is the proper particle number density and u^{α} is the fluid 4-velocity. We also assume the MHD condition

$$u^{\beta}F_{\alpha\beta} = 0 \ . \tag{2.10}$$

This condition implies the vanishing of the proper electric field (i.e., the electric field in the rest frame of the plasma). Equivalently, this is called the "frozen-in" condition because the frozen-flux theorem of Alfvén applies: In a perfectly conducting fluid, magnetic field lines move with the fluid: the field lines are 'frozen' into the plasma. Bekenstein & Oron (1978) give the necessary conditions for this assumption to be valid. By choosing ideal MHD we eliminate Joule heating so there is no exchange of energy between the electromagnetic field and the *internal* degrees of freedom of the plasma. There are interactions between the field and fluid, of course. In the magnetically dominated limit, Hirotani et al. (1992) showed that approximately 10% of the rest-mass energy and a significant fraction of the initial angular momentum are transported from the fluid to the magnetic field during the infall.

We assume the polytropic equation of state

$$P = K\rho_0^{\Gamma} \ , \tag{2.11}$$

where $\rho_0 = m_p n$ is the rest mass density, m_p is the rest mass of the particle and K is a constant. By neglecting dissipative effects and cooling in the plasma, the flow is adiabatic with a relativistic specific enthalpy of the form (see, for example, AC88)

$$\mu = m_{\rm p} + \frac{\Gamma}{\Gamma - 1}\frac{P}{n} \ . \tag{2.12}$$

The postshock fluid is expected to have a wide range of velocities, from relativistic to non-relativistic. To be consistent, the relation for Γ must account for this. Following AC88, we make the assumption that the fluid particles have a generalized Maxwell-Boltzmann velocity distribution valid for a simple relativistic gas.[1] For pioneering research and extensive discussion on relativistic gases see Jüttner (1911); Synge (1957); Israel (1963). In this case it can be shown (see AC88; Lightman, et al., 1975, §§5.23-5.35) that

$$\Gamma(\Theta) = 1 + \left[\frac{1}{\Theta}\left(\frac{K_1(1/\Theta)}{K_2(1/\Theta)} - 1\right) + 3\right]^{-1} \tag{2.13}$$

where $K_{1,2}(1/\Theta)$ are the modified Bessel functions given by

$$K_n(\alpha) = \int_0^{\infty} \exp\left[-\alpha \cosh\left(n\beta\right)\right] \mathrm{d}\beta \ , \tag{2.14}$$

[1]By "simple" we mean a group of particles with a continuous distribution of velocities, all having the same proper mass.

and $\Theta \equiv kT/m_{\rm p}c^2$. $\Gamma(\Theta)$ approaches the appropriate nonrelativistic and ultrarelativistic values of 5/3 and 4/3 as T varies from 0 to ∞, respectively.[2] Relativistic hydrodynamic shocks in a Synge gas were studied by Lanza, Miller & Motta (1985).

The magnetic field and electric field seen by a distant observer are defined in terms of the Faraday tensor as

$$B_\alpha \equiv \frac{1}{2}\eta_{\alpha\beta\gamma\delta}k^\beta F^{\gamma\delta} \tag{2.15}$$

$$E_\alpha \equiv F_{\alpha\beta}k^\beta \tag{2.16}$$

where $\kappa^\alpha = (1,0,0,0)$ is the time-like Killing vector and $\eta_{\alpha\beta\gamma\delta} \equiv \sqrt{-g}\,\epsilon_{\alpha\beta\gamma\delta}$.

Given the above assumptions, the flow streams along a magnetic field line; a flowline is also a field line. This is expressed by a magnetic stream function $\Psi = \Psi(r,\theta)$ that measures the magnetic flux between the rotational axis and a given field line. The stream function is closely related to the toroidal component of the vector potential; it is constant on a particular field line but can vary from line to line (Uchida 1997a,b). These same assumptions yield five constants of the motion. The MHD condition (2.10), the required symmetries of the flow and Maxwell's equations (2.8) generate the first conservation law (Bekenstein & Oron 1978)

$$\Omega_F(\Psi) \equiv -\frac{F_{tr}}{F_{\phi r}} = -\frac{F_{t\theta}}{F_{\phi\theta}}\ . \tag{2.17}$$

The constant $\Omega_F(\Psi)$ may vary from flowline to flowline and represents the angular velocity of the field line. By combining the MHD condition, Maxwell's equations and particle

[2]A gas obeying equations (2.12)-(2.14) is often referred to as a non-degenerate Fermi-Dirac gas, a non-degenerate electron gas, or simply, a Synge gas.

number conservation, we obtain a second conserved quantity

$$\eta(\Psi) = \frac{-\sqrt{-g}nu^r}{F_{\theta\phi}} = \frac{-\sqrt{-g}nu^\theta}{F_{\phi r}} \ , \tag{2.18}$$

which corresponds to the particle number flux through a flux tube. $\eta(\Psi)$ also is constant along a flowline but can have different values on different flowlines.

Useful expressions for the magnetic and electric field components, given in Boyer-Lindquist coordinates, are:

$$B_\phi = (\Delta/\Sigma)\sin\theta F_{\theta r} \tag{2.19}$$

$$B_r = (-G_t/\Delta\sin\theta)F_{\theta\phi} \tag{2.20}$$

$$B_p^2 \equiv -(1/\rho_w^2)\left[g^{rr}(\partial_r\Psi)^2 + g^{\theta\theta}(\partial_\theta\Psi)^2\right] \tag{2.21}$$

$$E_\theta = -\sqrt{-g}\,\Omega_F B^r/G_t \tag{2.22}$$

$$E_r = \sqrt{-g}\,\Omega_F B^\theta/G_t \tag{2.23}$$

where $G_t \equiv g_{tt} + g_{t\phi}\Omega_F$, $\rho_w^2 \equiv g_{t\phi}^2 - g_{tt}\,g_{\phi\phi} = \Delta\sin^2\theta$ and the poloidal components of the magnetic field are given by $B_p^2 \equiv -(B_r B^r + B_\theta B^\theta)/G_t^2$.

From the conservation of total energy and momentum (2.4) and the Killing equation $\psi_{\mu;\nu} + \psi_{\nu;\mu} = 0$, where ψ^μ is a Killing vector, it follows that $(\psi_\mu T^{\mu\nu})_{;\nu} = 0$. Thus, for any stationary and axisymmetric system, we define the conserved energy flux

$$\mathcal{E}^\mu = T^{\mu\nu}\kappa_\nu = T_t^\mu = (T_t^\mu)_{\rm em} + (T_t^\mu)_{\rm fluid} \tag{2.24}$$

and angular momentum flux

$$-\mathcal{L}^{\mu} = T^{\mu\nu}\chi_{\nu} = T^{\mu}_{\phi} = (T^{\mu}_{\phi})_{\rm em} + (T^{\mu}_{\phi})_{\rm fluid} \ , \tag{2.25}$$

where χ^{ν} is the axial Killing vector with Boyer-Lindquist components (0,0,0,1), and the electromagnetic part and fluid part are labelled by "em" and "fluid", respectively. The fluid and electromagnetic parts of the radial component of energy flux, $\mathcal{E}^{r}$, are

$$\mathcal{E}^{r}_{\rm fluid} \equiv (T^{r}_{t})_{\rm fluid} = \mu n u^{r} u_{t} \ , \tag{2.26}$$

$$\mathcal{E}^{r}_{\rm em} \equiv (T^{r}_{t})_{\rm em} = -\frac{B_{\phi}E_{\theta}}{4\pi\sqrt{-g}} = \frac{B_{\phi}B^{r}\Omega_{F}}{4\pi G_{t}} \ , \tag{2.27}$$

and the fluid and electromagnetic parts of the radial component of angular momentum flux, $\mathcal{L}^{r}$, are

$$-\mathcal{L}^{r}_{\rm fluid} \equiv (T^{r}_{\phi})_{\rm fluid} = \mu n u^{r} u_{\phi} \ , \tag{2.28}$$

$$-\mathcal{L}^{r}_{\rm em} \equiv (T^{r}_{\phi})_{\rm em} = -\frac{B_{\phi}}{4\pi g_{tt}}\left(\frac{g_{t\phi}E_{\theta}}{\sqrt{-g}} + B^{r}\right) = -\frac{B_{\phi}B^{r}}{4\pi G_{t}} \ , \tag{2.29}$$

where we have used relation (2.22).

We can express the radial energy and angular momentum fluxes as $\mathcal{E}^{r} = nu^{r}E$ and $\mathcal{L}^{r} = nu^{r}L$, respectively, where E and L are the total energy and the total angular momentum of the MHD flow seen by a distant observer, defined by

$$E \equiv \mu u_{t} - \frac{\Omega_{F}B_{\phi}}{4\pi\eta} \ , \tag{2.30}$$

$$L \equiv -\mu u_\phi - \frac{B_\phi}{4\pi\eta} \ . \tag{2.31}$$

Also, η can be written as

$$\eta = -\frac{nu^r}{B^r} G_t \ , \tag{2.32}$$

where we are considering the situation $u^r < 0$ and $B^r > 0$; that is, the value of η should be understood to be positive and negative on ingoing flowlines and outgoing flowlines, respectively. The quantities E and L are conserved along stream lines, which coincide with magnetic field lines (Camenzind 1986a). The final conserved quantity is K in the polytropic equation of state, (2.11), which is related to the specific entropy; a constant entropy implies a constant K.

In preparation for solving the jump conditions, it is convenient to express quantities in terms of the conserved variables and the Alfvén Mach number, defined by

$$M^2 \equiv \frac{4\pi\mu n u_p^2}{B_p^2} = \frac{4\pi\mu\eta u_p}{B_p} \ , \tag{2.33}$$

where u_p is the poloidal velocity defined by $u_p^2 \equiv -(u^r u_r + u^\theta u_\theta)$. The energy and angular momentum of the fluid are then

$$\mu u_t = \frac{M^2 E - eG_t}{M^2 - \alpha} \ , \tag{2.34}$$

$$\mu u_\phi = -\frac{M^2 L + eG_\phi}{M^2 - \alpha} \ , \tag{2.35}$$

where $e \equiv E - \Omega_F L$ is the total energy seen by a corotating observer with the magnetic

field line (also a conserved quantity),

$$G_\phi \equiv g_{t\phi} + g_{\phi\phi}\Omega_F = g_{\phi\phi}(\Omega_F - \omega) , \tag{2.36}$$

$$\alpha \equiv g_{tt} + 2g_{t\phi}\Omega_F + g_{\phi\phi}\Omega_F^2 = G_t + G_\phi\Omega_F , \tag{2.37}$$

and $\omega \equiv -g_{t\phi}/g_{\phi\phi}$ is the angular velocity of the zero angular momentum observer (ZAMO) with respect to a distant observer (ZAMO's are described in Appendix B). Note that $\alpha^{-1/2}$ is the "gravitational Lorentz factor" of a plasma, rotating with angular velocity Ω_F in the Kerr geometry. The definition includes both the effects of the gravitational redshift and the relativistic bulk motion of the plasma in the toroidal direction. The locations of the Alfvén points (r_A, θ_A) along a magnetic field line, where $\theta = \theta(r; \Psi)$, are defined by

$$M^2 = \alpha \,\big|_{\substack{r=r_A \\ \theta=\theta_A}} . \tag{2.38}$$

The significance of Alfvén points will be discussed in more detail later. The toroidal component of the magnetic field can be expressed as

$$B_\phi = 4\pi\eta \frac{G_\phi E + G_t L}{M^2 - \alpha} . \tag{2.39}$$

The apparent singularity of B_ϕ at the Alfvén point will also be addressed later.

The Conditions for MHD Accretion Onto a Kerr Black Hole

In the MHD model, the plasma is treated as a continuous conducting fluid (Landau

& Lifshitz, 1984). The MHD fluid approximation is generally a good approximation for the AGN environment. While the equations of neutral gas dynamics permit only one type of wave (the sound wave), MHD allows for three independent types of wave modes: the slow, the Alfvén and the fast wave. MHD waves are strongly anisotropic: the wave speed depends strongly on the angle between the direction of wave propagation and the direction of the magnetic field (see Figure 2.1). The Alfvén (or intermediate) speed is greatest when the wave propagates parallel to the field and goes to zero for perpendicular propagation. The Alfvén or shear wave is mechanically transverse, noncompressive and decoupled from the sonic mode.

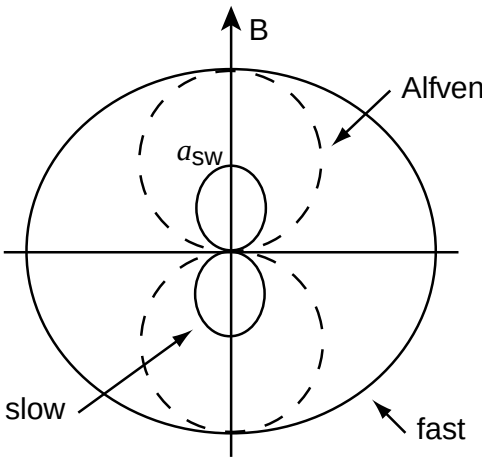


Figure 2.1: The Friedrichs or phase polar diagram of the three plasma wave velocities. The intermediate (Alfvén) and slow speed go to zero when the wave propagates perpendicular to the field. For parallel propagation the slow speed is the same as the relativistic sound speed (a_{sw}) defined in equation (2.62).

The fast wave and slow wave are often referred to as magneto-acoustic modes because they couple to the sound speed (c.f. [2.59] and [2.60]). The slow wave propagates fastest parallel to the magnetic field direction but vanishes in the perpendicular direction. The fast wave has virtually the same speed in all directions with a small increase due to the sound speed for perpendicular propagation. Both fast and slow waves are longitudinal

and compressive but they have different compressional properties. The magnetic field decreases across slow compression waves but increases across fast compression waves. This behavior persists for MHD shocks.

These three characteristic modes generate critical points at which the accreting plasma must satisfy specific conditions in order to complete the journey from the injection point (the source of the plasma) to the horizon. In this section these conditions are presented, along with other physically relevant points the plasma encounters during the fall to the black hole.

Relativistic Bernoulli equation

The conservation laws allow two components of the 4-velocity to be written in terms of the flow parameters E, L, Ω_F, η, M and μ. The solution for the poloidal velocity then follows from the normalization condition and can be written

$$(1 + u_p^2) = \frac{-u_t^2}{\rho_w^2}(g_{\phi\phi} + 2lg_{t\phi} + l^2 g_{tt}) \ , \tag{2.40}$$

where $\ell \equiv -u_\phi/u_t$ is the specific angular momentum of the plasma[3]. Substitution of equations (2.34) and (2.35) give the final form of the poloidal wind equation, sometimes referred to as the relativistic Bernoulli equation,

$$(1 + u_p^2) = (E/\mu)^2[(\alpha - 2M^2)f^2 - k] \ , \tag{2.41}$$

[3]Technically, the relativistic generalization of the specific angular momentum $j = \Omega(r\sin\theta)^2$.

where

$$f \equiv -\frac{G_\phi + G_t \tilde{L}}{\rho_w (M^2 - \alpha)} , \tag{2.42}$$

$$k \equiv (g_{\phi\phi} + 2 g_{t\phi} \tilde{L} + g_{tt} \tilde{L}^2)/\rho_w^2 , \tag{2.43}$$

and $\tilde{L} \equiv L/E$. The relativistic specific enthalpy can be written as (see Camenzind 1987; Takahashi 2000a)

$$\mu = m_p \left[1 + h_I \left(\frac{u_p^I B_p}{u_p B_p^I} \right)^{\Gamma - 1} \right] , \tag{2.44}$$

where

$$h_I \equiv \frac{\Gamma}{\Gamma - 1} \frac{P_I}{n_I m_p} , \tag{2.45}$$

and the "I" indicates quantities evaluated at the point where plasma is injected from the plasma source (i.e., the injection point). In this way the fifth constant of motion, entropy, can be replaced by h_I. In the cold limit ($P = 0$), $h_I \to 0$ and $\mu \to m_p$.

Figure 2.2 illustrates typical solutions for the poloidal flow equation (2.41) for a monopole geometry in the equatorial plane, where the plasma is cold ($P = 0$) with given parameters E, L and Ω_F in the Schwarzschild spacetime. The flow originates at the injection point, which must lie radially inward of the separation point (the region separating inflow from outflow, c.f. [2.63]), and then successively passes through the Alfvén point, the fast magnetosonic point, the light cylinder and then the horizon. In general, the slow magnetosonic point would be located between the injection point and the Alfvén point, but for cold flows this critical point vanishes. A slow magnetosonic shock must be located between the plasma injection radius ($r = r_{\rm I}$) and the Alfvén radius ($r = r_{\rm A}$), if the shock

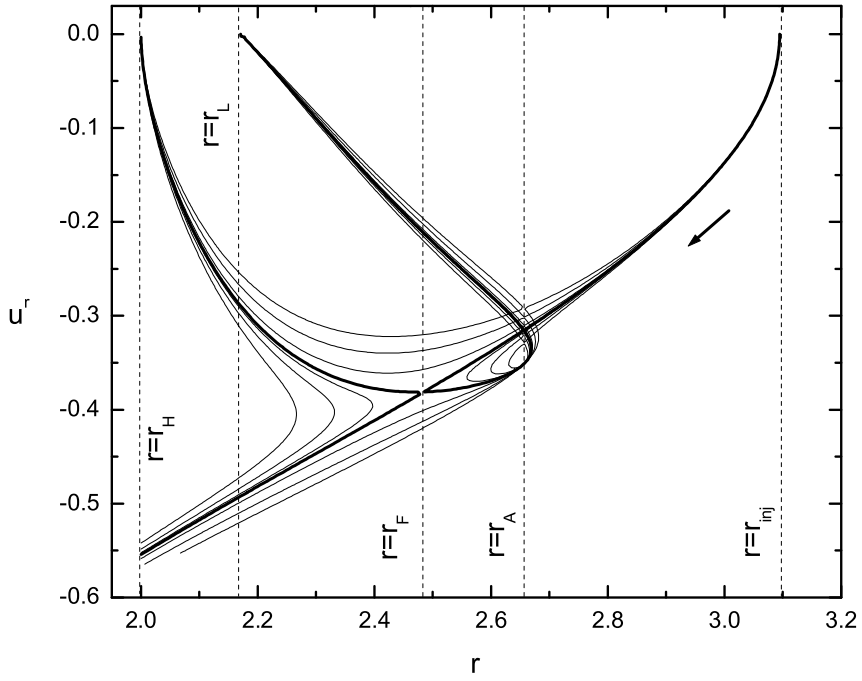


Figure 2.2: A preshock cold trans-fast MHD accretion solution ($\eta = \eta_{\rm F}$; bold curve with arrow). The solution attached to the event horizon $r = r_{\rm H}$ with zero-velocity is unphysical. The other solutions ($\eta \neq \eta_{\rm F}$; thin curves) are also unphysical because the flows do not go through the fast point with the fast magnetosonic speed. The radii of $r = r_{\rm F}$, $r = r_{\rm L}$, $r = r_{\rm A}$ and $r = r_{\rm inj}$ are the locations of the fast magnetosonic point, the light surface, the Alfvén point and the injection point, respectively. A slow magnetosonic shock would be possible somewhere between the plasma injection radius and the Alfvén radius. The radial distance is scaled by the black hole mass.

conditions are to be satisfied. After a slow magnetosonic shock, the heated postshock flow falls into the black hole, once again passing through a slow magnetosonic point, the Alfvén point and a fast magnetosonic point. The radius of the light surface, $r = r_{\rm L}$, and the Alfvén radius do not change after the shock formation (see next section); because the flow is no longer cold, a slow magnetosonic point does exist.

Split-Monopole Field

The complete description of MHD accretion requires the specification of the magne-

tosphere surrounding the black hole. To determine the magnetic field configuration, the equation for cross-field momentum balance must be solved. This Grad-Shafranov equation is the equation of motion projected perpendicular to the magnetic surfaces. The stream equation, describing magnetic surfaces $\Psi(r,\theta)$ in the vicinity of a rotating black hole, was first formulated by Nitta, Takahashi & Tomimatsu (1991). It has not yet been solved except in simplified situations (see, e.g., Beskin, Kuznetsova & Rafikov 1998 for a review; for a recent solution, see Tomimatsu & Takahashi 2001). To avoid the extreme mathematical difficulty of the complete MHD system, we can consider vacuum solutions of the magnetic stream function as a practical approximation. In this work we have chosen the split-monopole field (see, for example, Michel 1973a,b) which has a stream function of the form

$$\Psi(\theta) = A - B\cos\theta \ , \tag{2.46}$$

where A and B are arbitrary constants. Then $\partial_r\Psi = 0$ and $\partial_\theta\Psi = B\sin\theta$ so that the poloidal magnetic field is simply (c.f. [2.21])

$$B_p = \frac{B_{\rm inj}}{\sqrt{\Delta\Sigma}} \ , \tag{2.47}$$

where $B_{\rm inj}$ is the poloidal magnetic field at the plasma injection source.

Light Surfaces

A consequence of the ideal MHD assumption is that magnetic field lines rigidly rotate, producing two light surfaces in the black hole magnetosphere. A light surface is the position at which plasma particles would rotate with the speed of light (details can be found

in Znajek 1977). The outer light surface is the same as found in pulsar magnetosphere models, (Goldreich & Julian, 1969). The inner light surface is unique to black holes, due to the existence of a horizon. The locations of the light surfaces are given by (see, e.g., Blandford & Znajek (1977); TNTT90),

$$\alpha(r_L) = 0 \ . \tag{2.48}$$

The existence of an inner light surface can be most easily seen by considering a Schwarzschild black hole. Then the light surface condition becomes $0 = g_{tt} + g_{\phi\phi}\Omega_F^2$. In the limit of zero mass this reduces to $0 = 1 - r^2 \sin^2\theta$, giving the outer light surface. For non-zero mass however, the condition becomes $r - 2/m - r^3\Omega_F^2$, in the equatorial plane. For acceptable ranges of Ω_F an inner light surface forms, located close to the horizon.

The light cylinders are of no dynamical importance, since the flow decouples from the magnetic field before it reaches the light cylinder (Ardavan, 1976a). But this also implies that there are regions in which the plasma flow is restricted. Only in the region between the light cylinders can plasma co-rotate with the magnetic field lines. Outside this region a centrifugal slingshot is in effect, ensuring that charges outside the outer light cylinder flow outward and charges inside the inner light cylinder flow inward (Horiuchi, Mestel & Okamoto 1995). Thus, within the inner light surface the plasma must fall into the black hole; outside the outer light surface the plasma must stream outward.

The location of the light surfaces depend on the parameters a, θ, and Ω_F. In Chapter 6 we will study the effects of polar angle on these locations. The existence of a middle, co-rotating region requires that Ω_F lie between some range $\Omega_F^{\min} < \Omega_F < \Omega_F^{\max}$ where the

maximum or minimum value is obtained when $r_L^{in} = r_L^{out}$. Special situations occur: for $\Omega_F = 0$ it is clear from the definition that the inner light surface coincides with the static limit surface, i.e., $\alpha = g_{tt} = 0$. Also, when the angular velocity of the magnetosphere is the same as that of the horizon, $\Omega_F = \omega_H$, the light surface coincides with the event horizon. If the black hole rotates faster than the magnetosphere, effectively "dragging" the field, $(0 < \Omega_F < \omega_H)$, the inner light surface must be located in the ergosphere. Finally, if $0 < \omega_H < \Omega_F$, the inner light surface can lie in the ergosphere or outside it.

Inner and Outer Alfvén Radius

An important property of plasma flows in a magnetosphere is the existence of three "critical points" where the velocity of the flow equals the wave velocities of the three MHD wave modes. When $\alpha = M^2$ it appears that the function f in the poloidal wind equation, (2.41), diverges. To obtain a physical accretion flow, that streams with a finite velocity, we must require the condition

$$\tilde{L} = -\left(\frac{G_\phi}{G_t}\right)_A \tag{2.49}$$

to hold, where the subscript "A" denotes quantities at the Alfvén radius. Note the distinction between the Alfvén radius defined here and the Alfvén point defined in equation (2.38). Generally these two positions will be coincident but it is not required. To be precise, the Alfvén point must occur at an Alfvén radius to keep the poloidal wind equation from becoming singular, but the converse is not required. The distinction will be relevant in the next chapter when shock categories are developed and also in Chapter 6 where it will be studied in depth. We will tend to use the terms interchangeably when they occur at the same position.

Because the spacetime geometry is incorporated in equation (2.49), this radius is really the general-relativistic version of the Alfvén radius. Equations (2.34), (2.35) and (2.39) have the same singular point but do not produce any additional constraints. Due to the relation $\alpha_A = M_A^2 > 0$, the Alfvén points must be located between the inner and outer light surfaces; the value of $\tilde{L}$ is also restricted. If the magnetosphere drags the black hole in the same direction of its rotation ($\Omega_F/\omega_H > 1$) or rotates counter to the black hole rotation ($\Omega_F\omega_H < 0$), then the condition $0 < \tilde{L}\Omega_F < 1$ means that two Alfvén points exist between the light surfaces, while for $\tilde{L}\Omega_F > 1$ no Alfvén points appear. For the situation in which the black hole drags the magnetosphere ($0 < \Omega_F < \omega_H$), there is only one Alfvén point for any $\tilde{L}\Omega_F$. Thus, the number of Alfvén points for a given $\tilde{L}$ depends on the angular velocity Ω_F of the field line; this is a purely general-relativistic effect. This effect will be important in the following chapter when shock solutions are categorized.

When $\tilde{L}\Omega_F > 1$ it is possible for both the total energy and angular momentum of the MHD accreting plasma to be negative; this means that energy extraction from the black hole is possible (see Figure 3.8). Although this feature is of no interest to us here, considerable research has been undertaken to analyze this behavior, (Christodoulou & Ruffini 1971; Blandford & Znajek 1977; Znajek 1977; Beskin & Kuznetsova 2000; Punsly 2001, TNTT90). However, information about the position of the Alfvén point can be obtained by expressing the energy E and angular momentum L as functions of the Alfvén point:

$$E = \left(\frac{G_t}{\alpha}\right)_A e \,, \tag{2.50}$$

$$L = \left(\frac{-g_{\phi\phi}}{\alpha}\right)_A (\Omega_F - \omega_A)\, e\ . \tag{2.51}$$

Because α_A and e are always positive, a negative energy implies $(G_t)_A < 0$. Then, a negative angular momentum L, with positive $(-g_{\phi\phi})_A$, puts the Alfvén point within the ergosphere, under the condition $0 < \Omega_F < \omega_H$.

Fast and Slow Magnetosonic Points

The fast magnetosonic point is defined as a singularity in the gradient of M^2 (Beskin, Kuznetsova & Rafikov, 1998). TNTT90 generalized the fast magnetosonic point derivation given by Camenzind (1986b) to the Kerr geometry and proved that any ingoing flowline from the Alfvén point to the event horizon must pass through the fast magnetosonic point. By making use of the differentiation of η and M^2, the differential form of the poloidal equation (2.41) becomes:

$$(\ln u_p)' = \left(\frac{u_p^2}{M^2}\right)^3 \frac{\mathcal{N}}{(u_p^2 - u_{AW}^2)^2 (u_p^2 - u_{FM}^2)(u_p^2 - u_{SM}^2)}\ , \tag{2.52}$$

where the prime $(\ldots)'$ denotes $[(\partial_\theta \Psi)\partial_r - (\partial_r \Psi)\partial_\theta]/(\sqrt{-g} B_p)$, the derivative along a stream line. The numerator of equation (2.52) is given by

$$\mathcal{N} = \left(\frac{E}{\mu}\right)^2 \left\{ [\mathcal{R}(M^2 - \alpha) C_{sw}^2 + M^4 \mathcal{A}^2](\ln B_p)' + \frac{1}{2}(1 + C_{sw}^2)[M^4 (M^2 - \alpha) k' - \mathcal{Q}\alpha'] \right\} \tag{2.53}$$

where

$$\mathcal{A} \equiv \tilde{e}^2 + \alpha k = f^2 (M^2 - \alpha)^2\ , \tag{2.54}$$

$$\mathcal{R} \equiv \alpha\tilde{e}^2 - 2\tilde{e}^2M^2 - kM^4 \ , \tag{2.55}$$

$$\mathcal{Q} \equiv \alpha\tilde{e}^2 - 3\tilde{e}^2M^2 - 2kM^4 \ , \tag{2.56}$$

$$\tilde{e} \equiv 1 - \Omega_F\tilde{L} \ . \tag{2.57}$$

The general-relativistic Alfvén wave speed u_{AW}, the slow magnetosonic wave speed u_{SM} (slow mode), and the fast magnetosonic wave speed u_{FM} (fast mode) are defined by

$$u_{AW}^2 \equiv \frac{B_P^2}{4\pi\mu n}\alpha \ , \tag{2.58}$$

$$u_{SM}^2 \equiv \frac{1}{2}\left(Z - \sqrt{Z^2 - 4C_{sw}^2u_{AW}^2}\right) \ , \tag{2.59}$$

$$u_{FM}^2 \equiv \frac{1}{2}\left(Z + \sqrt{Z^2 - 4C_{sw}^2u_{AW}^2}\right) \ , \tag{2.60}$$

where

$$Z \equiv u_{AW}^2 + \frac{B_\phi^2}{4\pi\mu n\rho_w^2} + C_{sw}^2 \ . \tag{2.61}$$

The relativistic sound velocity a_{sw} is defined by

$$a_{sw}^2 \equiv \left(\frac{\partial \ln \mu}{\partial \ln n}\right)_{ad} = (\Gamma - 1)\frac{\mu - m_p}{\mu} \ , \tag{2.62}$$

and the sound four-velocity is given by $C_{sw}^2 = a_{sw}^2/(1 - a_{sw}^2)$. Equations (2.52) through (2.62) were taken from Takahashi (2000a). The magnetosonic critical points occur where the denominator of equation (2.52) vanishes.

The requirement that the flow pass through the fast magnetosonic point establishes a conserved quantity. For example, specifying E, L and Ω_F then restricts $\eta = \eta(E, L, \Omega_F)$. Figure 2.2 shows several solutions to the wind equation, but only one curve (heavy solid),

obeying the relation for η, goes through r_F.

Injection and Separation Points

So far, physically relevant positions along the accreting flow have been discussed. But there are two additional positions of interest, the separation point and the injection point. They pertain to the origin of the accreting plasma. We begin with the separation point. Outgoing jets have been observed in AGN and are believed to be generated from magnetospheres surrounding SMBHs. But the entire region of the magnetosphere cannot consist of outflow due to the existence of the horizon. There must exist some boundary region where accreting plasma is separated from outgoing winds and the poloidal velocity of the particles becomes very small.

Thus, there is a source of mass flux in the magnetic flux tube itself, with some of the mass being driven to infinity and some accreting toward the horizon. This region is called the separation region. The origin of these mass fluxes may be due to the matter surrounding the black hole (i.e., accretion disk) or the process of particle creation. Figure 2.3 illustrates the separation region and both ingoing and outgoing flows. These flows are specified by E, L and Ω_F and stream away from the separation point along a given flux surface, Ψ. The constant Ψ line crosses the $\alpha = 0$ curves at the light surface and the $\alpha = M^2$ curves at the Alfvén points.

Specializing to cold flows, with zero initial poloidal velocity, the separation surface

must satisfy the conditions $u_p = 0$ and $|u_p'| < \infty$. Equations (2.52) and (2.53)[4] imply that

$$\alpha' = 0 \Big|_{r=r_{\rm S}} , \tag{2.63}$$

which can be taken as the definition of the separation point. For a monopole geometry the position of the separation point in the equatorial plane is given by

$$r_{\rm S} = [m(1 - a\Omega_F)^2]^{1/3}\Omega_F^{-2/3} . \tag{2.64}$$

For this situation, the separation point corresponds to the corotation point where Ω_F is equal to the angular velocity Ω_K of circular orbits in Kerr geometry [$\Omega_K = (\sqrt{mr^3} - ma)/(r^3 - ma^2)$] (Hirotani et al. 1992). This relation shows how the black hole spin affects the location of the separation point: if the magnetosphere and black hole are corotating ($a\Omega_F > 1$), r_S moves inward as compared to the Schwarzschild case. Conversely, if they are counter-rotating, r_S moves outward. Physically, the effect of co-rotation is to weaken gravity while counter-rotation effectively strengthens gravity. The separation point is thus similar to the stagnation point of Johnson & Axford (1971). In their model the stagnation point, the location where inflow and outflow of a spherically symmetric gas originated, was the point at which the gas pressure balanced gravity.

The separation point partitions the magnetospheric plasma into two unique regions. But where does the plasma come from? There must be a source of mass flux in the magnetic flux tube. The details of the plasma injection process have been discussed by

[4]To be completely accurate, the cold flow limit of these equations give the separation surface. These equations are given in Chapter 6, equations (6.3) and (6.4).

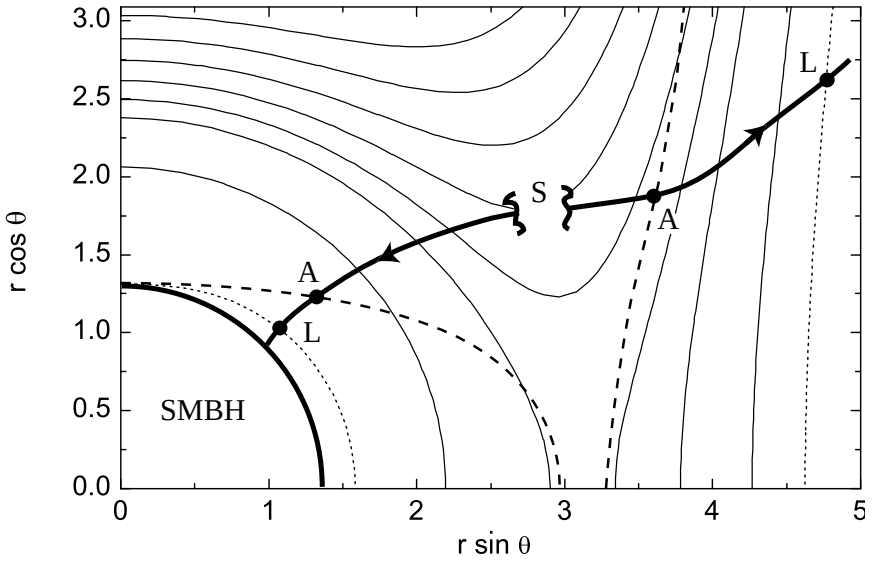


Figure 2.3: Schematic of typical inflow and outflow in a black hole magnetosphere. Thin solid lines are contours of constant α, the thick solid line denotes the plasma flow. The thin dotted lines indicate $\alpha = 0$ and the thick dashed line gives $\alpha = M^2$. Both flows begin at an injection point located in the separation region (S) and pass through the Alfvén point (A), and light surface (L). The point where the flowline is tangent to a constant α contour is the separation point. The fast and slow points are not shown.

various authors (Blandford & Znajek 1977; Beskin 1992; Punsly 2001). Pair creation in the γ-ray field of an AGN is one possible source of the plasma (see Hirotani & Okamoto 1998 for details). Particle creation can be considered to exist in a small section of a magnetic flux tube, where a conserved energy and angular momentum flux are injected into the tube.

The injection point for cold flows is defined by setting the poloidal velocity to be zero in the wind equation, (2.41), which then reduces to

$$E - \Omega_F L = \alpha^{1/2} \ . \tag{2.65}$$

In our model we are not directly concerned with the injection process. Instead, conserved quantities are assigned, equation (2.65) produces an injection point and the resulting flow

Table 2.1: Types of MHD Shocks. The "state" of the plasma is based on its relative speed with respect to the characteristic wave mode speeds and is given by $[1] \geq u_{\rm F} \geq [2] \geq u_{\rm A} \geq [3] \geq u_{\rm S} \geq [4]$. The arrow '$\rightarrow$' indicates the shock transition from preshock to postshock quantities.

Type	State	Velocity	$B_{\rm tang}$
fast	$[1] \rightarrow [2]$	Super-fast $\rightarrow$ Sub-fast	increase
slow	$[3] \rightarrow [4]$	Super-slow $\rightarrow$ Sub-slow	decrease
intermediate	$[1] \rightarrow [3]$	Super-Alfvén $\rightarrow$ Sub-Alfvén	sign change
"	$[1] \rightarrow [4]$	"	"
"	$[2] \rightarrow [3]$	"	"
"	$[2] \rightarrow [4]$	"	"

is accepted if all the critical point conditions are satisfied.

Types of MHD Shocks

While the equations of neutral gas dynamics permit only one type of wave (the sound wave), and one type of shock, MHD allows for three different types of wave modes. This gives rise to three different types of MHD shocks connecting plasma states which are traditionally labelled from 1 to 4, with state 1 a super-fast state, state 2 sub-fast but super-Alfvénic, state 3 sub-Alfvénic but super-slow, and state 4 sub-slow (Landau & Lifshitz 1984; De Sterck, Low & Poedts 1998). A fast shock refracts the magnetic field away from the shock normal while a slow shock refracts the magnetic field toward the shock normal. Intermediate shocks are unstable in ideal MHD and there is even debate about their existence in general (see, for example, Wu & Kennel 1992; De Sterck & Poedts 2000). Thus, only fast and slow shocks are considered in this research. Table 2.1 summarizes the important characteristics of MHD shocks. See Draine (1993) for good review of astrophysical shocks, including MHD shocks.

MHD Shocks in Kerr Geometry

In order to explore the properties of MHD shocks associated with accretion flows near a black hole, we derive in this section the general relativistic version of MHD shock conditions—an extension of the flat spacetime model of AC88. Figure 2.4 shows a schematic picture of general accretion inflow from a plasma source, through a shock front, onto a black hole. In this picture, the accretion originates from the plasma source (which can be the surface of a torus) rotating around a black hole. Strong shocks may be produced somewhere between the plasma source and the event horizon.

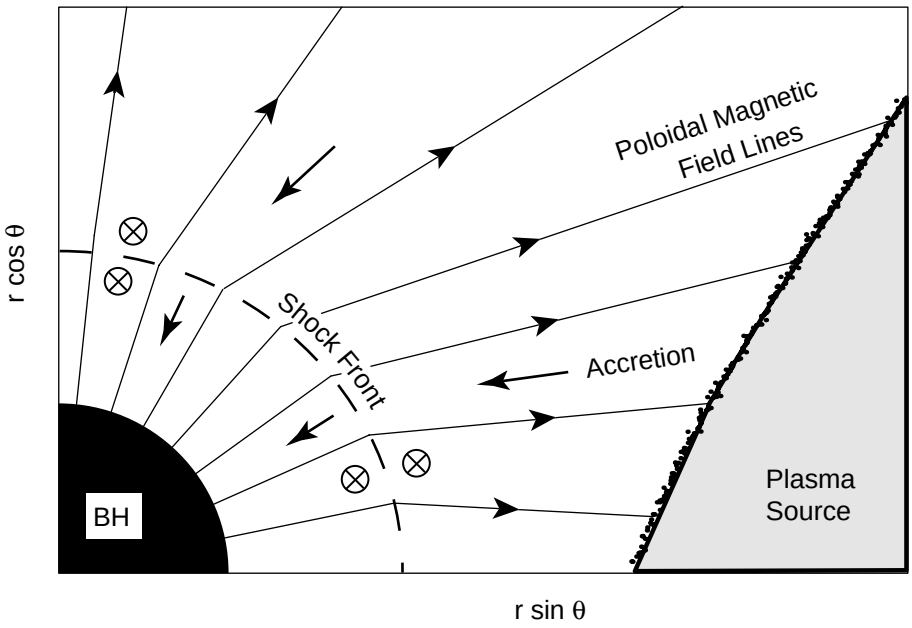


Figure 2.4: Accretion flows with shock front. It is assumed that in the poloidal plane the downstream flow is radial and the shock front is perpendicular to the downstream flow direction. In the general case, the magnetic field has a nonzero toroidal component (marked by $\otimes$) due to the plasma rotation.

The Jump Conditions

In this section we develop the Rankine-Hugoniot shock conditions (hereafter RH) for

general relativistic flows (Takahashi, 2000b). In a complete solution of plasma accretion that includes a shock, the flow must satisfy a set of conditions on either side of the discontinuity. The RH shock conditions for a relativistic flow, derived in Landau & Lifshitz (1959), are discussed in (*e.g.,* Chakrabarti, 1989, 1990a,b; Lu et al., 1997). The goal is to express as many postshock quantities as possible in terms of the preshock quantities and the compression ratio.

A brief historical digression about the RH conditions is in order. William John Macquorn Rankine, a Scottish engineer, first presented the normal shock equations for continuity, momentum and energy, in an 1870 paper titled "On the Thermodynamic Theory of Waves of Finite Longitudinal Disturbance," (Rankine 1870). Incidentally, it was in this same paper that the symbol γ was first used to represent the ratio of specific heats, c_p/c_v. In 1887 Pierre Henry Hugoniot independently produced the equations obtained by Rankine. Although their results applied to non-relativistic flows and adiabatic, normal shocks, the term *Rankine-Hugoniot conditions* is, in modern usage, usually used to describe all equations dealing with changes across any shock in which energy is conserved. We will follow the modern usage and refer to the relationship of physical quantities on either side of a shock as the RH (or jump) conditions. Research on the RH conditions continues; a complete bifurcation analysis of the RH equations for compressible magnetohydrodynamics in the case of a perfect gas was recently performed by Heinrich & Rohde (2003).

The jump conditions for arbitrary shocks in a relativistic MHD flow are (e.g., AC88):

$$[nu^{\alpha}]n_{\alpha} = 0 \ , \quad \text{— the particle number conservation} \tag{2.66}$$

$$[T^{\alpha\beta}]n_\alpha = 0 \ , \quad \text{— the energy momentum conservation} \tag{2.67}$$

$$[\vec{E}] \times \vec{n} = 0 \ , \quad \text{— the continuity relations for the electric field} \tag{2.68}$$

$$[\vec{B}] \cdot \vec{n} = 0 \ , \quad \text{— the continuity relations for the magnetic field} \tag{2.69}$$

where $n^\alpha = (n_0, \vec{n})$ is the shock normal and the square brackets denote the difference between the values of a quantity on the two sides of the shock.

We assume that the downstream flow velocity is radial (normal to the event horizon) and the shock front is perpendicular to the downstream flow **n**=(1,0,0) as illustrated in Figure 2.4. Then, we set

$$u_1^\alpha = (u_1^t, u_1^r, u_1^\theta, u_1^\phi) \ , \tag{2.70}$$

$$u_2^\alpha = (u_2^t, u_2^r, 0, u_2^\phi) \ , \tag{2.71}$$

$$B_1^\alpha = (B^r, B_1^\theta, B_1^\phi) \ , \tag{2.72}$$

$$B_2^\alpha = (B^r, 0, B_2^\phi) \ , \tag{2.73}$$

$$E_1^\alpha = (E_1^r, E^\theta, 0) \ , \tag{2.74}$$

$$E_2^\alpha = (0, E^\theta, 0) \ , \tag{2.75}$$

where equations (2.68) and (2.69) have been used. The subscripts "1" and "2" denote the preshock and the postshock quantities, respectively. Equations (2.66) and (2.67) evaluated in the shock rest frame yield the following relations

$$n_1 u_1^r = n_2 u_2^r \ , \tag{2.76}$$

$$n_1\mu_1(u^r u_r)_1 - P_1 + \frac{1}{8\pi g_{tt}}(-E_1^r E_{r1} + B_1^\theta B_{\theta 1} + B_1^\phi B_{\phi 1})$$
$$= \quad n_2\mu_2(u^r u_r)_2 - P_2 + \frac{1}{8\pi g_{tt}}(B_2^\phi B_{\phi 2}) \ , \tag{2.77}$$

$$n_1\mu_1 u_1^r u_1^\theta - \frac{1}{4\pi g_{tt}}\left(B^r B_1^\theta + E_1^r E^\theta\right) = 0 \ , \tag{2.78}$$

$$n_1\mu_1 u_1^r u_1^\phi - \frac{1}{4\pi g_{tt}}\left(B_1^\phi B^r\right) = n_2\mu_2 u_2^r u_2^\phi - \frac{1}{4\pi g_{tt}}\left(B_2^\phi B^r\right) \ , \tag{2.79}$$

$$n_1\mu_1 u_1^r u_1^t - \frac{1}{4\pi g_{tt}}\left(\frac{B_{\phi 1}E_\theta}{\sqrt{-g}} + B_1^t B^r\right) = n_2\mu_2 u_2^r u_2^t$$
$$- \frac{1}{4\pi g_{tt}}\left(\frac{B_{\phi 2}E_\theta}{\sqrt{-g}} + B_2^t B^r\right) \ . \tag{2.80}$$

From the MHD conditions, we also obtain

$$E_{r1}u_{t1} + \sqrt{-g}(B_1^\phi u_1^\theta - B_1^\theta u_1^\phi) = 0 \ , \tag{2.81}$$

$$(B^r u_1^\phi - B_1^\phi u_1^r)\frac{1}{u_{t1}} = \frac{-E_\theta}{\sqrt{-g}} = (B^r u_2^\phi - B_2^\phi u_2^r)\frac{1}{u_{t2}} \ , \tag{2.82}$$

$$(g_{t\phi}E_\theta + \sqrt{-g}B^r)u_1^\theta + (g_{t\phi}E_{r1} - \sqrt{-g}B_1^\theta)u_1^r = 0 \ , \tag{2.83}$$

$$E_{r1}u_1^r + E_{\theta 1}u_1^\theta = 0 \ . \tag{2.84}$$

From the shock condition of $(T^{rt})_1 = (T^{rt})_2$, we obtain

$$(E - \omega L)_1 = (E - \omega L)_2 \tag{2.85}$$

where $\omega \equiv -g_{t\phi}/g_{\phi\phi}$ is the angular velocity of the zero angular momentum observer

(ZAMO) with respect to a distant observer. The shock condition $(T^{r\phi})_1 = (T^{r\phi})_2$, yields

$$(g_{t\phi}E + g_{tt}L)_1 = (g_{t\phi}E + g_{tt}L)_2 \quad . \tag{2.86}$$

From these relations, we see that $E_1 = E_2$ and $L_1 = L_2$. Although the jump conditions are given in the shock rest frame they indicate that the energy and angular momentum seen by a distant observer continue to be conserved along a stream line even for shocked flow. Further, from the particle number conservation and the continuity for electric and magnetic fields at the shock front, we also obtain the relations $(\Omega_F)_1 = (\Omega_F)_2$ and $\eta_1 = \eta_2$. Thus, the field-aligned flow parameters E, L, Ω_F and η are conserved across the shock front. This means that the location of the light surface and the Alfvén radius are not altered by the generation of a shock (see [2.48] and [2.51]). Because of entropy generation ($S_2 > S_1$ and $K_2 > K_1$), the fast/slow magnetosonic points appear at different locations in the preshock and postshock flow solutions. The increasing entropy makes the Alfvén wave speed at the Alfvén point $u_{\rm A}$ [$\equiv u_{\rm AW}(r_{\rm A})$] in a postshock solution smaller than that in a preshock solution.

Dimensionless Parameters and Their Relations

When the state of the upstream flow is given, there are five unknown quantities downstream (n_2, u_2^t, u_2^r, u_2^ϕ, and B_2^ϕ). It is convenient to introduce five dimensionless parameters to replace these unknown quantities. Then the jump conditions can be systematically applied to eliminate the parameters, until we obtain a single polynomial equation of seventh degree in the compression ratio. After solving this equation we can calculate the remaining

unknown quantities.

From the energy momentum conservation at the shock front, we have $(T^{rt})_1 = (T^{rt})_2$, where T^{rt} can be reduced to

$$\begin{aligned} T^{rt} &= g^{tt}(\mathcal{E}^r_{\rm fluid} + \mathcal{E}^r_{\rm em}) - g^{t\phi}(\mathcal{L}^r_{\rm fluid} + \mathcal{L}^r_{\rm em}) && (2.87) \\ &= g^{tt}\left\{ n\mu u^r u_t(1-\omega\ell) + \frac{B_\phi B^r(\Omega_F - \omega)}{4\pi G_t} \right\} . && (2.88) \end{aligned}$$

We define the "magnetization parameter", introduced by Michel (1969), which denotes the ratio of the Poynting flux to the total mass-energy flux seen by ZAMO,

$$\sigma \equiv \frac{(\mathcal{E}^r - \omega\mathcal{L}^r)_{\rm em}}{(\mathcal{E}^r - \omega\mathcal{L}^r)_{\rm fluid}} . \tag{2.89}$$

Then we can express equation (2.87) as

$$T^{rt} = g^{tt}(\mathcal{E}^r - \omega\mathcal{L}^r)_{\rm fluid}(1+\sigma) = (nu^r)(\mu u^t)(1+\sigma) . \tag{2.90}$$

The magnetization parameter can then be reduced to

$$\sigma = \frac{B_\phi}{4\pi\eta(\mu u^t)}\frac{G_\phi}{\rho_w^2} . \tag{2.91}$$

By using equations (2.34) and (2.35), σ is denoted in terms of M^2, E, L and Ω_F, as

$$\sigma = -\frac{(G_\phi E + G_t L)G_\phi}{\rho_w^2 e + (g_{\phi\phi}E + g_{t\phi}L)M^2} = -\frac{e - h\alpha}{e - hM^2} , \tag{2.92}$$

where $h \equiv g^{tt}(E - \omega L)$. This relation can be inverted to express M^2 in terms of σ, E, L and Ω_F,

$$M^2 = \frac{1}{h\sigma}\left[e(1+\sigma) - h\alpha\right] \ . \tag{2.93}$$

Next, we define the following dimensionless parameters:

$$q \equiv \frac{B_{\phi 2}}{B_{\phi 1}} = \frac{M_1^2 - \alpha}{M_2^2 - \alpha} \ , \tag{2.94}$$

$$\zeta \equiv \frac{\mu_2 u_2^t}{\mu_1 u_1^t} = \frac{e - hM_2^2}{e - hM_1^2} q \ , \tag{2.95}$$

$$\xi \equiv \frac{n_2 u_2^t}{n_1 u_1^t} = \frac{M_1^2}{M_2^2}\zeta \ , \tag{2.96}$$

where q is the amplification factor of the transverse magnetic field, ζ is the ratio of the shock frame specific enthalpies and ξ is the shock frame compression ratio. Physically, the compression ratio is the ratio of the shock normal fluid velocities, in the shock frame. This can be easily shown by rewriting equation (2.96) as $\xi = v_1^{\hat{r}}/v_2^{\hat{r}}$, where $v_i^{\hat{r}}$ are the radial velocities of the fluid in the ZAMO frame. From equations (2.76), (2.80), (2.82) we obtain the following relation

$$1 - \zeta = \sigma_1 \left(q - 1\right) \ . \tag{2.97}$$

The normalization of the 4-velocity ($u^\alpha u_\alpha = c^2 = 1$) gives an equation for u_2^t

$$u_2^t = \left\{ g_{tt} + 2g_{t\phi}\Omega_2 + g_{\phi\phi}\Omega_2^2 + \frac{(u^r u_r)_1}{\xi^2 (u_1^t)^2} \right\}^{-1/2} \ , \tag{2.98}$$

where $\Omega \equiv u^\phi/u^t$ is the angular velocity of the fluid, and

$$\Omega_2 = \frac{e\Omega_F - \rho_w^{-2}(g_{t\phi}E + g_{tt}L)M_2^2}{e - hM_2^2} \ . \tag{2.99}$$

Once ξ or M_2 are determined, Ω_2 and u_2^t are determined.

From equation (2.77), we obtain

$$1 - \frac{\zeta}{\xi} - \frac{P_1 - P_2}{n_1\mu_1(u^r u_r)_1} + \frac{(-E^r E_r + B^\theta B_\theta + B^\phi B_\phi)_1 - (B^\phi B_\phi)_2}{8\pi g_{tt} n_1 \mu_1 (u^r u_r)_1} = 0 \ . \tag{2.100}$$

Using the relations

$$-E^r E_r + B^\theta B_\theta = \frac{g_{tt}\alpha}{G_t^2} B^\theta B_\theta \ , \tag{2.101}$$

$$(B^\phi B_\phi)_1 - (B^\phi B_\phi)_2 = (B^\phi B_\phi)_1 (1 - q^2) \ , \tag{2.102}$$

we get

$$1 - \frac{\zeta}{\xi} = \Pi - \mathcal{X}_1 + (q^2 - 1)\mathcal{T}_1 \ , \tag{2.103}$$

with

$$\Pi \equiv \frac{P_1 - P_2}{n_1\mu_1(u^r u_r)_1} = 1 - \frac{1}{\xi} + \frac{\sigma_1}{\xi}(q-1) + \mathcal{X}_1 - (q^2-1)\mathcal{T}_1 \ , \tag{2.104}$$

$$\mathcal{X}_1 \equiv \frac{\alpha (B^\theta B_\theta)_1}{2B^r B_r M_1^2} \ , \tag{2.105}$$

$$\mathcal{T}_1 \equiv \frac{\sigma_1}{2}\left(\frac{u^t}{u^r}\right)_1^2 \frac{\rho_w^2(\Omega_F - \Omega_1)}{g_{rr}G_\phi} \ , \tag{2.106}$$

which depend on ξ, q and upstream parameters M_1^2 (or σ_1), E, L and Ω_F. The relation

between M_2^2 and M_1^2 are given by the poloidal equation (2.41). At the shock location $r = r_{sh}$, both $M^2 = M_1^2$ and $M^2 = M_2^2$ are solutions of the poloidal equation.

In the following, for preshock accretion flows we restrict ourselves to the cold limit ($P_1 = 0$). Using the definition of ζ and the equation of state for a Boltzmann gas (2.12), we find with equation (2.104)

$$1 - \frac{u_2^t}{u_1^t} = \sigma_1(q-1) - \frac{\Gamma}{\Gamma - 1}\frac{g_{rr}(u^r/u^t)_1^2(u_2^t)^2}{\xi}\Pi \ . \tag{2.107}$$

Combining equations (2.94) and (2.97) gives a quadratic equation for ζ

$$\zeta^2 - \left\{1 + \sigma_1 + \left(\frac{G_t}{M_1^2} - \frac{\sigma_1\Omega_F}{\Omega_F - \Omega_1}\right)\xi\right\}\zeta + \left(\frac{G_t}{M_1^2} - \frac{\sigma_1\Omega_1}{\Omega_F - \Omega_1}\right)\xi = 0 \ , \tag{2.108}$$

where we have used the relation $\Omega - \Omega_F = \sigma M^2/G_\phi$. This equation for ζ will be used extensively for establishing shock categories in the following chapter. We are now able to eliminate u_2^t and q from equation (2.107). After considerable manipulation[5] we obtain a polynomial of seventh degree in ξ

$$\sum_{i=0}^{7} c_i(M_1^2, \Gamma; m, a, E, L, \Omega_F, \eta)\xi^i = 0 \ . \tag{2.109}$$

The coefficients c_i are dependent only on upstream parameters, except for Γ which is a

[5]By 'considerable manipulation' we mean several months of effort to obtain a useful analytic form of equation (2.109). The result was a polynomial having a number of terms in the neighborhood of 10^5, even with the metric coefficients left as $g_{\alpha\beta}$.

function of the downstream temperature. Θ is related to ξ through

$$\Theta = -g_{rr} u_1^t u_2^t (u_1^r/u_1^t)^2 \Pi/\xi \ . \tag{2.110}$$

Thus, the compression ratio ξ is the solution of a polynomial (2.109), which has to be solved simultaneously with equation (2.13) for the polytropic index Γ of the shocked plasma. The explicit forms of the coefficients c_i are quite lengthy. This polynomial has in general several real solutions corresponding to the different shock transitions. Restrictions on the postshock physical quantities must be applied to eliminate the extraneous solutions. After the compression ratio has been computed, the downstream quantities ζ, q, u_2^t, u_2^r, Ω_2 and Π are obtained from equations, (2.108), (2.94), (2.98), (2.76), (2.99) and (2.104), respectively. The derivation leading to (2.109) was first done by Takahashi (TNTT90). The analytic form of this equation, verifying that it is 7^{th} degree in ξ, and numerical solutions were first obtained by me.

Finally, it should be noted that the jump conditions derived here place no restriction on what type of RH shock can occur—the results are valid for either slow or fast magnetosonic shocks. Thus, we seek solutions of (2.109) that will give shocks as illustrated in Figure 2.5. The curves in these figures are contours of the wind equation for different "entropy related mass accretion rate", $\dot{\mathcal{M}}$ defined by

$$\dot{\mathcal{M}} \equiv m_p \eta K^N = m_p \eta K^{1/(\Gamma-1)} \ . \tag{2.111}$$

This quantity is constant in a shock-free flow but it can change across the shock due to

the generation of entropy, (Chakrabarti 1990a).

A slow shock occurs after the outer slow point. The flow must then pass through another slow point, an Alfvén point and a fast point successively in order to reach the horizon. For a fast shock, it is the preshock flow that must pass through all the critical points; the postshock flow must then pass through a final fast point before reaching the horizon.

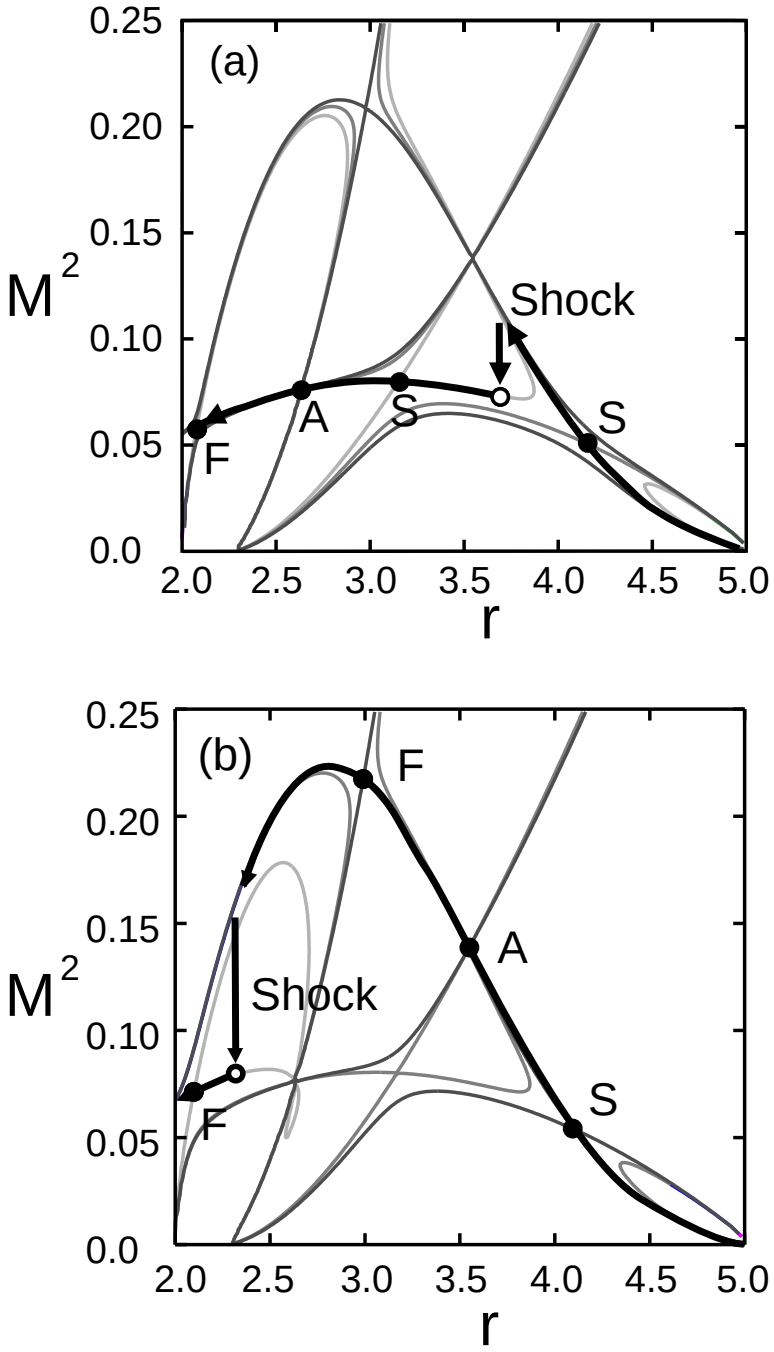


Figure 2.5: Examples of a slow (a) and fast (b) magnetosonic shock in the M^2 vs. r plane for a hot flow. Curves are contours of constant $\dot{\mathcal{M}}$. In either case, the accreting flow follows a particular contour until a shock occurs. Then the flow drops to a different contour and proceeds through the required critical points. Figures adapted from "http://phe.phyas.aichi-edu.ac.jp/jgoto/mhd.html".

CHAPTER 3

CATEGORIZATION OF MHD SHOCKS

'Have a place for everything and keep the thing somewhere else. This is not advice, it is merely custom.' – Mark Twain

Introduction

Due to the large number of input parameters it is useful to arrange the possible shock solutions in a coherent fashion. Not only does this provide some insight into the behavior of the shocks, it aids in the numerical calculation of shock solutions. We would like to categorize both fast and slow shocks. It is convenient to use the relationship between the angular velocities of the accreting plasma and the black hole. In addition, the magnitude and sign of the preshock magnetization parameter (σ_1) is also useful in forming the various categories.[1] The sign of σ_1 also determines whether $\zeta > 1$ or $\zeta < 1$; this is important to know when solving the jump conditions numerically. The categories can be subdivided based on the signs of E and L which is useful when considering shocks in the ergoregion.

We begin by investigating the solution space of two shock parameters, ξ and ζ, first for slow shocks and then for fast shocks. By merely graphing their relationship, large regions of the parameter space can be excluded. Next, restrictions on shock parameters with respect to the types of accretion flows are studied. Because σ_1 (and G_ϕ) play a role the flow types can be associated with the cases arising from the ζ vs. ξ relationship. The

[1] The sign of the magnetization parameter indicates the direction of Poynting flux: $\sigma_1 < 0$ for outward flux.

flow types of TNTT90 are generalized to the negative spin situation and identified with positive spin cases. Finally, the relationships and behaviors of various physical quantities are provided in several tables.

The ξ vs. ζ Parameter Space

One of the variables describing the shock transition is $\zeta \equiv (\mu_2 u_2^t)/(\mu_1 u_1^t)$. Its qualitative relationship to the compression ratio can be investigated to better understand the shock properties. We begin with the equation for ζ, equation (2.95), written in terms of a quadratic in ζ:

$$\zeta^2 - \left[1 + \sigma_1 + \left(\frac{G_t}{M_1^2} - \frac{\sigma_1 \Omega_F}{\Omega_F - \Omega_1}\right)\xi\right]\zeta + \left(\frac{G_t}{M_1^2} - \frac{\sigma_1 \Omega_1}{\Omega_F - \Omega_1}\right)\xi = 0 \ . \tag{3.1}$$

The shock quantities ξ and ζ are now explicitly related through the preshock magnetization in the sense that the sign and magnitude of σ_1 in equation (3.1) limits the acceptable (ζ, ξ) parameter space.

From the relation $\Omega - \Omega_F = \sigma M^2/G_\phi$, we obtain for the preshock flow

$$\frac{G_t}{M_1^2} - \frac{\sigma_1 \Omega_F}{\Omega_F - \Omega_1} = \frac{G_t}{M_1^2} + \frac{G_\phi}{\sigma_1 M_1^2}\sigma_1 \Omega_F = \frac{\alpha}{M_1^2} \ . \tag{3.2}$$

Substitution into equation (3.1) gives

$$\zeta^2 - (1 + \sigma_1)\zeta + \frac{\alpha}{M_1^2}(-\zeta + \delta/\alpha)\xi = 0 \ , \tag{3.3}$$

where $\alpha \equiv G_t + \Omega_F G_\phi$ and $\delta \equiv G_t + \Omega_1 G_\phi$. Rearranging gives a useful form for the

compression ratio in terms of ζ:

$$\xi(\zeta) = \frac{M_1^2}{\alpha}\frac{\zeta[\zeta - (1+\sigma_1)]}{(\zeta - \delta/\alpha)} \ . \tag{3.4}$$

From the definition of ζ and $\xi \equiv (n_2 u_2^t)/(n_1 u_1^t) = (M_1^2/M_2^2)\zeta$, we require $\zeta > 0$ and $\xi > 1$. From the shock condition, $M_1^2/M_2^2 > 1$ is also required, implying $\xi > \zeta$. By inspection of equation (3.4) we see that $\xi = 0$ at $\zeta = 0$ or $\zeta = 1 + \sigma_1$, and $\xi \to \pm\infty$ as $\zeta \to \delta/\alpha$. Also, for $\zeta \gg 1$, equation (3.4) reduces to

$$\xi = \zeta\frac{M_1^2}{\alpha}\left(\frac{1 - (1+\sigma_1)/\zeta}{1 - \delta/(\alpha\zeta)}\right) \approx \zeta\frac{M_1^2}{\alpha}(1 - \frac{\sigma_1}{\zeta}) \ . \tag{3.5}$$

The slope is then M_1^2/α for large ζ and diverges upward (downward) for negative (positive) σ_1 as ζ decreases. Remember from Chapter 2 that in the sub-Alfvénic region (slow shock domain), $M_1^2/\alpha < 1$ while in the super-Alfvénic region (fast shock domain), $M_1^2/\alpha > 1$. The detailed behavior of equation (3.4) depends on the value of σ_1. There are four cases for slow shocks and three for fast shocks. Figures 3.1 through 3.5 illustrate the various cases and include the restrictions and asymptotes discussed above. Now we work out the details, first for slow shocks, then for fast shocks.

Slow Magnetosonic Shocks

Case 1. [$(1+\sigma_1) < 0$]. Then $\sigma_1 < -1$ and $\zeta > \delta/\alpha$ ($\zeta > 1$ or $\zeta < 1$). The possibility exists for two different ζ values given the same ξ. The thick curve (solid and dashed) in Figure 3.1 is the general solution of equation (3.4). However, from equation (2.97) we see that for slow shocks ($q < 1$), a negative magnetization requires $\zeta < 1$. Thus

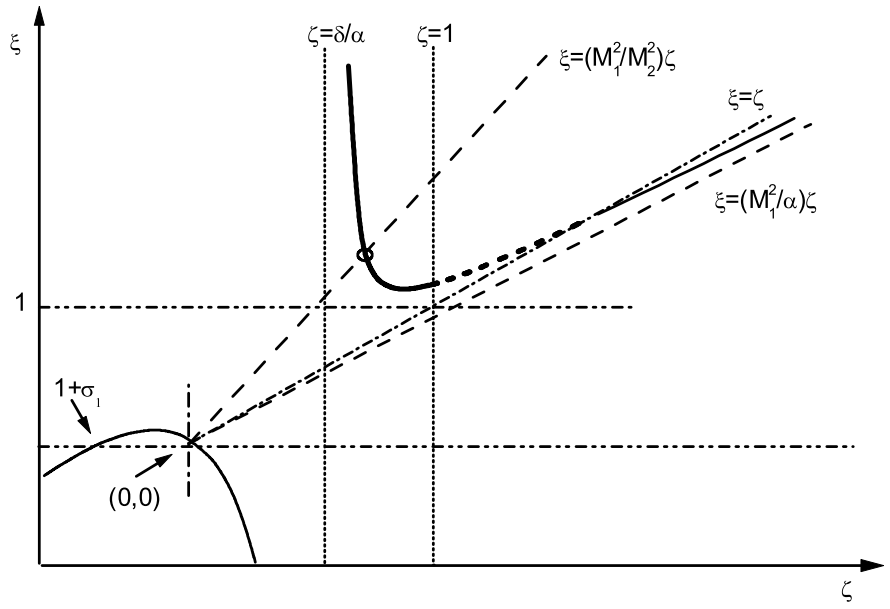


Figure 3.1: The solution curve of equation (3.4) for Case 1 (slow shock, Type II) is indicated by the thick curve (solid and dashed). The thick dashed curve is eliminated by the requirement $\zeta < 1$. Only the solid thick curve is acceptable, here constrained on the left, bottom and right by $\zeta > \delta/\alpha$, $\xi > 1$ and $\zeta < 1$, respectively. The particular solution is the shown by the circle.

the thick dashed line is excluded. The actual solution is, of course, the intersection of the general solution with the $\xi = (M_1^2/M_2^2)\zeta$ line, indicated by a circle in the figure. No shock solutions have been found for this case, in that we have always had $\sigma_1 > -1$.

Case 2. [$0 < (1 + \sigma_1) < 1$]. Then $-1 < \sigma_1 < 0$ and there are two possible regions for shocks: $\zeta > \delta/\alpha$ or $0 < \zeta < (1 + \sigma_1)$. Figure 3.2 shows the solution curves for this case. The cutoff for valid solutions in either region is the $\xi = \zeta$ line. As in Case 1, the $\zeta > 1$ region is excluded for negative magnetization. Also, the region $0 < \zeta < (1+\sigma_1)$ is forbidden because this would require $\xi < 1$. The minimum value of ξ occurs at

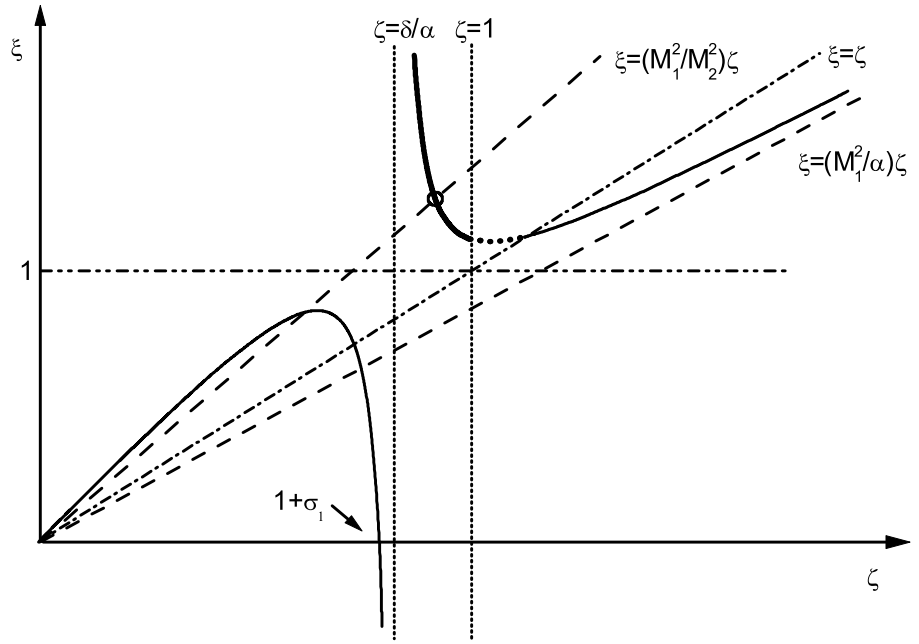


Figure 3.2: The solution curve of equation (3.4) for Case 2 (slow shock, Type II). The solid thick section of the curve indicates the acceptable region. The particular solution is indicated by the circle.

either $\zeta = 1$ or $\zeta = (\delta/\alpha)[1 - \sqrt{1 - (\alpha/\delta)(1 + \sigma_1)}]$ (from $\mathrm{d}\xi/\mathrm{d}\zeta = 0$), depending on the shape of the curve. For the latter situation the minimum compression ratio is given by $\xi_{\min} = (M_1^2/\alpha)\left\{2(\delta/\alpha)[\sqrt{1 - (\alpha/\delta)(1 + \sigma_1)} - 1] - (1 + \sigma_1)\right\}$. For typical values of α, δ, σ_1 and M_1, $\xi_{\min} \approx 4$. From Figure 3.2 we see that it is unlikely that a large compression ratio will be obtained for Case 2 shocks.

Case 3. [$(1 + \sigma_1) > 1$]. Then $\sigma_1 > 0$ and $1 < \zeta < \delta/\alpha$. A minimum value for ξ occurs for $\zeta \approx 1$ and is $\xi_{\min} \approx (M_1^2\sigma_1)/(G_\phi(\Omega_1 - \Omega_F))$. For $\zeta = 1$ we must have either $\sigma_1 = 0$ or $q = 1$. The former is Case 4 (below) and the latter implies no shock. The ξ vs. ζ relationship for Case 3 is shown in Figure 3.3. If the preshock magnetization is

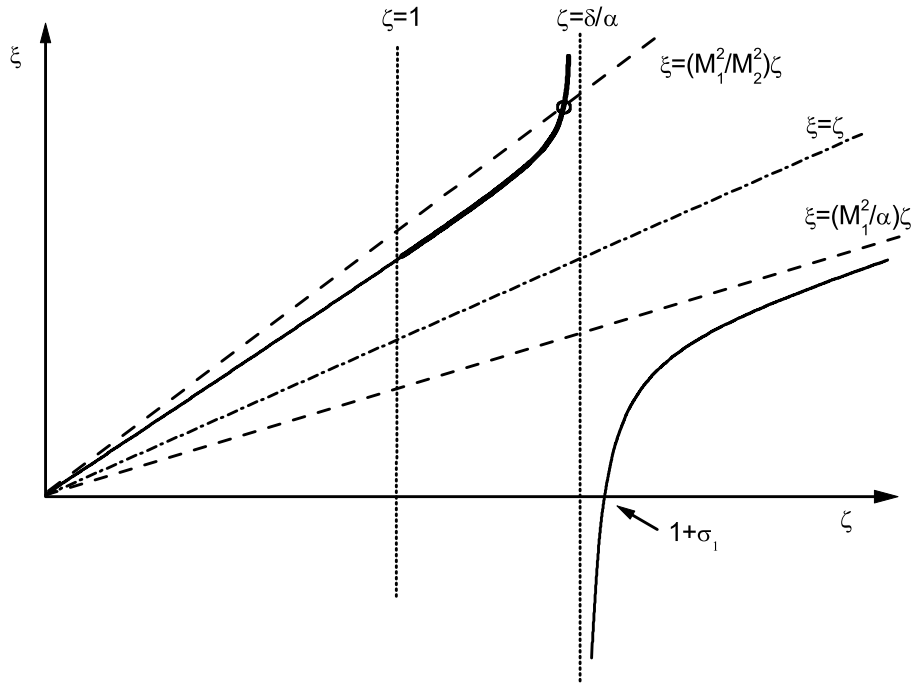


Figure 3.3: The solution curve of (3.4) for Case 3 (slow shock, Types I, II and III). The thick section indicates the acceptable region, bounded by $1 < \zeta < \delta/\alpha$. The particular solution is shown by the circle. For this case a large compression ratio may be possible. This requires either $\zeta \approx \delta/alpha$ or $\delta/alpha \gg 1$. The latter case requires a large preshock magnetization.

sufficiently large, along with δ/α, then there is a possibility of a large compression ratio.

Case 4. [$\sigma_1 = 0$]. Then $\xi = (M_1^2/\alpha)(\zeta - 1)/(\zeta - (\delta/\alpha))$. This case turns out to be a more complicated situation than might first appear. From equation (2.91)

$$\sigma = \frac{B_\phi}{4\pi\eta(\mu u^t)} \frac{G_\phi}{\rho_w^2} \ , \tag{3.6}$$

there are two ways to obtain zero magnetization. Either $B_{\phi 1} = 0$ or $G_\phi = 0$. We

consider each situation separately:

(a) [$G_\phi = 0$]. From the definition of G_ϕ, this occurs when $\Omega_F = \omega$. The ZAMO is rotating with the poloidal magnetic field and sees no Poynting flux. Also, when $G_\phi = 0$, $\delta/\alpha = (G_t + \Omega_1 G_\phi)/(G_t + \Omega_F G_\phi) = 1$. In order to have a finite compression ratio, the condition $\zeta(G_\phi = 0) = 1$ must be met. Shocks do occur for this situation and physical quantities are well behaved. Examples of shocks in this category will be presented in Chapter 4.

(b) [$B_{\phi 1} = 0$]. Then the field line is perpendicular to the shock front and there is no influence of the magnetic field on the shocked flow. The MHD shock is equivalent to a hydrodynamic shock. This occurs at $r_{sh} = r_A^{out}$ for the Multiple Inner Alfvén points configuration. This possibility will be discussed in detail in Chapter 5.

Fast Magnetosonic Shocks

Although fast shocks will be discussed in more detail in Chapter 7, it is appropriate to analyze the different categories here. As with slow shocks, the ξ vs. ζ behavior in equation (3.4) can be used to generate various cases for fast shocks. We still require $\zeta > 0$ and $\xi > 1$, but now $M_{1,2}^2 > \alpha$. This puts a greater restriction on the solution space. For fast shocks there are three possible cases.

Case 5. [$(1 + \sigma_1 < 1)$]. Then $\sigma_1 < 0$ and $\zeta > 1$. For this case, a large ζ could give a large compression ratio, see Figure 3.4. But after an exhaustive search, valid flows for this case have had only a small negative magnetization, $\zeta \approx 1$ and ξ has always

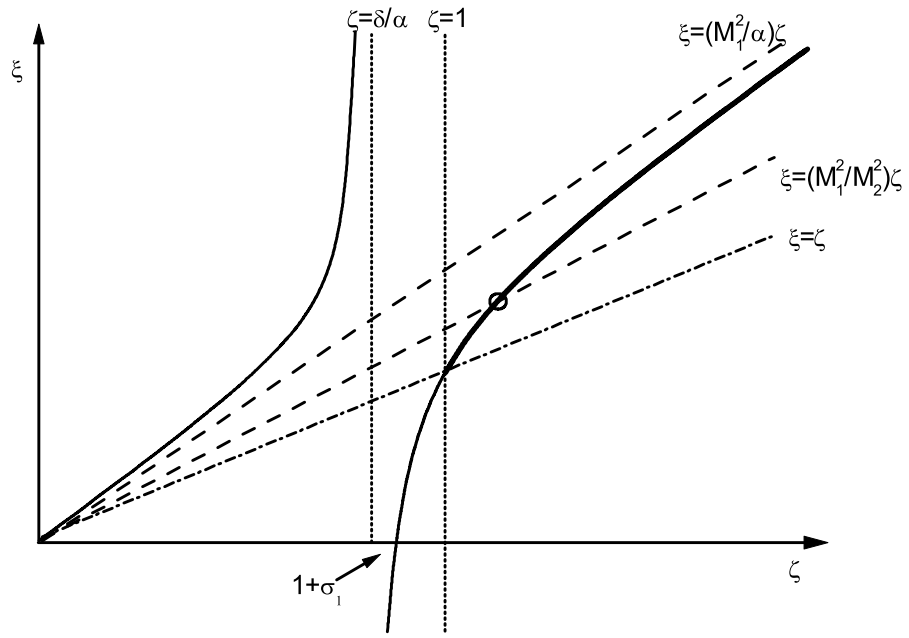


Figure 3.4: The solution curve of (3.4) for Case 5 (fast shock, Type II). The thick section indicates the acceptable region, bounded by $\zeta > 1$. The particular solution is shown by the circle. For this case a large compression ratio is possible, but none have been found.

been less than four.

Case 6. [$(1 + \sigma_1 > 1)$]. Then $\sigma_1 > 0$ and $\zeta < 1$. The shock conditions and the requirements of equation (3.4) severely limit the range of solutions. From Figure 3.5 it is clear that a large ξ is unlikely, regardless of the value for σ_1.

Case 7. [$\sigma_1 = 0$]. This is similar to Case 4 for slow shocks. Can only occur if $G_\phi = 0$.

Types of Accretion Flows

In addition to studying shocks by relating shock parameters to the preshock magne-

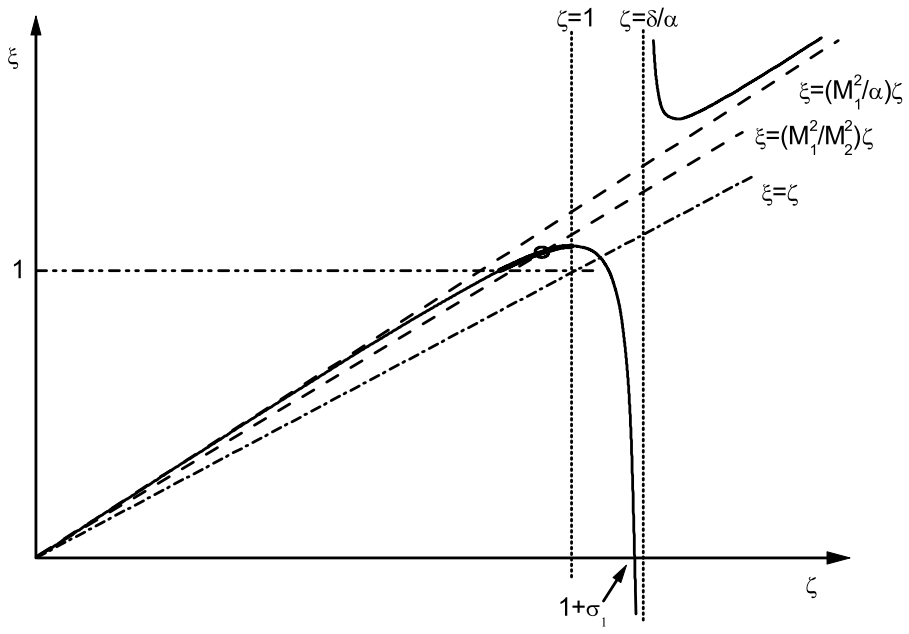


Figure 3.5: The solution curve of (3.4) for Case 6 (fast shock, Types I and III). The thick section indicates the acceptable region, bounded by $\zeta < 1$ and $\xi > 1$. The particular solution is shown by the circle. For this case a large compression ratio is extremely unlikely.

tization, it is also possible to classify shocks based on the types of MHD accretion flows that are allowed in the Kerr black hole geometry. For the model used in this research, TNTT90 discovered three types of flows, similar to the classification of transonic hydrodynamic flows by Fukue (1987), based on the relationship of the horizon angular velocity to the magnetosphere angular velocity. They are given by:

$$\text{Type I} \qquad \omega_H < \Omega_F < \Omega_{\max} \ , \tag{3.7}$$

$$\text{Type II} \qquad 0 < \Omega_F < \omega_H \ , \tag{3.8}$$

$$\text{Type III} \qquad \Omega_{\min} < \Omega_F < 0 \ . \tag{3.9}$$

Here, $\Omega_{\rm min}$ and $\Omega_{\rm max}$ are given by

$$\Omega_{\rm max/min} = \left[6m\cos\left(\frac{\psi}{3}+\frac{2\pi}{3}k\right)-a\right]^{-1} \quad (k=0,1)\ , \tag{3.10}$$

where $\cos\psi = -(a/m)$, and $k=0$ and $k=1$ correspond to the maximum and minimum values, respectively. These types assume $\omega_H > 0$, (positive black hole spin), a split-monopole field line geometry and apply only to accretion flows in the equatorial plane. The maximum and minimum values are determined by forcing the light cylinders to coincide ($r_L^{\rm in} = r_L^{\rm out}$). Details can be found in TNTT90. Figure 3.6 shows the ranges of the magnetosphere angular velocity and the horizon angular velocity as a function of spin. Also indicated are the flow type regions. The types for negative spin are discussed later in the chapter.

Further consequences of typing the flow according to equations (3.7)–(3.9) can be seen by plotting $\Omega_F\tilde{L}$ vs. r_A, as shown in Figures 3.7 and 3.8. For Type I or III flows there can be two Alfvén points for a given $\tilde{L}$ while for Type II flows there can only be one. That the number of Alfvén points for a given $\tilde{L}$ depends on the angular velocity Ω_F of the field line is a purely general-relativistic effect. The flow types can be further subdivided by energy and angular momentum. This is especially evident for Type II flows.

The details of the derivation for shock categories are rather tedious. One such derivation for Type II shocks has been provided in Appendix A. To summarize, slow shocks in Type II accretion ($q<1$, $\Omega_F<\omega_H$, $B_\phi>0$) with $a\geq 0$ can fall into three categories, determined by the sign of G_ϕ (a function of geometry and magnetosphere angular velocity):

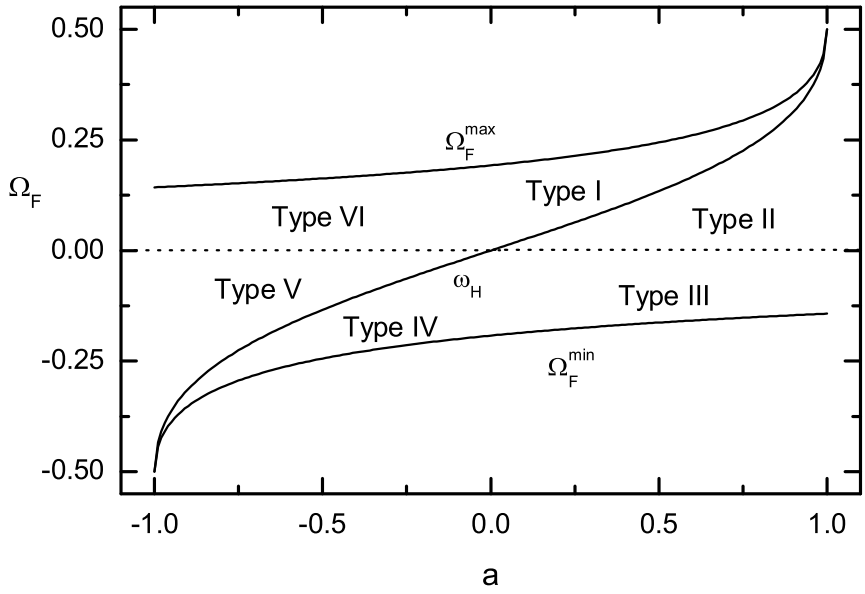


Figure 3.6: The maximum and minimum Ω_F as a function of spin, in the equatorial plane assuming a split-monopole poloidal magnetic field configuration. The three flow type regions for positive spin, defined by equations (3.7)–(3.9) are indicated as are the negative spin types.

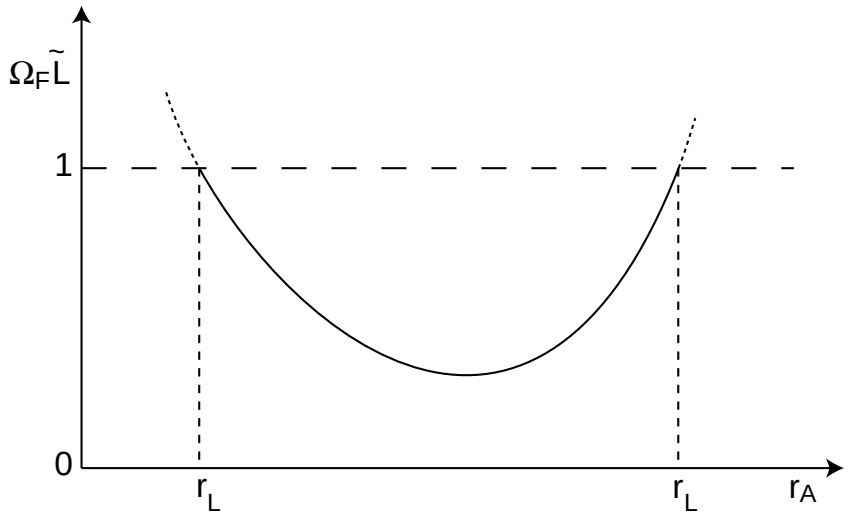


Figure 3.7: Relation of $\Omega_F\tilde{L}$ to r_A for Type I and III flows ($0 < \Omega_F\tilde{L} < 1$).

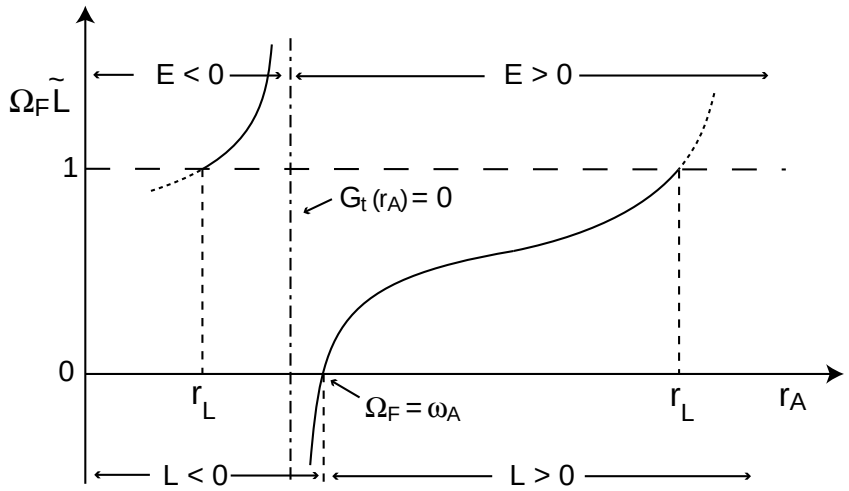


Figure 3.8: Relation of $\Omega_F \tilde{L}$ to r_A for Type II flows. The parameter space can be further subdivided based on the signs of E and L. The three subcategories are: Type IIb region ($E < 0$, $L < 0$), Type IIa ($E > 0$, $L < 0$) and Type IIc ($E > 0$, $L > 0$).

1. $G_\phi > 0$: Then $\zeta > 1$, $\sigma_{1,2} > 0$ and $0 < \Omega_F < \Omega_2 < \Omega_1 \gtrless \omega < \omega_H$.

2. $G_\phi = 0$: Then $\zeta = 1$, $\sigma_{1,2} = 0$ and $\omega = \Omega_F$.

3. $G_\phi < 0$: Then $\zeta < 1$, $\sigma_{1,2} < 0$ and $0 < \omega < \Omega_F < \Omega_2 < \Omega_1 < \omega_H$.

In the first category the relationship of the angular velocities of the accreting plasma and a ZAMO are indeterminate and will depend on the precise initial conditions. The results for all flow types are presented in Tables 3.1–3.6.

Of most significance is that these categories can now be related to the classifications obtained from considering σ_1 in the ξ vs. ζ relationship. The three regions of Type II flows, $\{(E < 0,\, L < 0),\, (E > 0,\, L < 0),\, (E > 0,\, L > 0)\}$, shown in Figure 3.8, allow for natural subdivisions. Without performing any numerical calculations, much information about shocks can be obtained. Extracting information about the strength of shocks and possible locations, such as the ergosphere, is possible without performing any calculations.

Slow shocks for Type I accretion ($q < 1$, $\omega_H < \Omega_F < \Omega_{\max}$) are both simpler and more

complicated. In the case of a single inner Alfvén radius, $B_\phi < 0$ and an analysis similar to that above is straightforward. However, in the rare case of multiple inner Alfvén radii we must be more careful due to the sign change of B_ϕ. This will be covered in more detail in Chapter 6. But keeping in mind this sign change, the analysis mirrors the one above. The analysis for Type III flows is also straightforward.

In the tables, Type "I" refers to the case with only one inner Alfvén point. The other Type I's refer to the case of multiple inner Alfvén points (MIAPs).[2] Specifically, Imi1 refers to valid preshock flow through the inner Alfvén point and the shock occurring between the two Alfvén points, Imi3 is the same except the shock occurs between the outer Alfvén point and the injection point, and Imi2 refers to the transition point where the magnetization parameter is zero. Imo refers to valid preshock flow through the outer Alfvén point and the shock also occurring between this Alfvén point and the injection point. The other flow categories are self-explanatory.

It is interesting that a single flow can produce shocks in more than one subcategory. In the case of MIAP's this is obvious: subcategories Imi1, Im2 and Imi3 all have the same parameter set, (E, L, Ω_F, η). But Type II flows can also have this behavior: as the shock location moves inward, Type IIa1 switches to IIa2 and then to IIa3 in succession.

The previous results were all based on a positive black hole spin. Because there was no restriction on the angular momentum of the flow or magnetosphere angular velocity, these types can be mapped 1-1 to the negative spin situation. Flow types IV-VI, similar

[2]By "multiple" we mean two.

to those defined in equations (3.7)–(3.9) are then defined for negative spins:

$$\text{Type IV} \qquad \Omega_{\min} < \Omega_F < \omega_H \ , \tag{3.11}$$

$$\text{Type V} \qquad \omega_H < \Omega_F < 0 \ , \tag{3.12}$$

$$\text{Type VI} \qquad 0 < \Omega_F < \Omega_{\max} \ . \tag{3.13}$$

In the ξ vs. ζ analysis, there is no difference for negative spin.

In the next chapter, slow shocks around a counter-rotating black hole are compared with shocks around a co-rotating black hole. So categories for shocks occurring near a negative spin black hole are presented in Tables 3.3 and 3.4, although not in as much detail. Fast shocks are studied in Chapter 7, so for completeness, Tables 3.5 and 3.6 list the restrictions and ranges of fast shocks and flow parameters for positive spin black holes and Cases 5-7.

The first set of shock solutions presented in the next chapter are Type I or VI and all are Case 3. Using the results developed in this chapter we could have predicted a large compression ratio for negative spin shocks (sadly, this was not the case). From Figure 3.3, ξ can only be large when ζ becomes large, because M_1^2/M_2^2 never gets larger than four. Note that ζ approaching the δ/α asymptote is not sufficient to produce a large ξ because the actual solution is the intersection of the solution curve of equation (3.4) and the line $\xi = (M_1^2/M_2^2)\zeta$. The figure also indicates that a large magnetization is needed. But how does the negative black hole spin produce a strong shock? To obtain a large ξ we can try

to make δ/α as large as possible. From the definitions of α and δ we have

$$\frac{\delta}{\alpha} = \frac{G_t + \Omega_1 G_\phi}{G_t + \Omega_F G_\phi}. \tag{3.14}$$

To ensure that $\delta/\alpha \gg 1$ we can make α very small; this means arranging the Alfvén point to be close to the inner light cylinder. This is not sufficient however: from equation (3.14), if $\Omega_1 \approx \Omega_F$ it does not matter how small α becomes. So we want a relatively large δ; with $G_t > 0$ and $G_\phi < 0$ we attain this by arranging for a large negative Ω_1. We can do this by choosing a large negative spin; frame dragging will do the rest.

Developing categories for various shock solutions organizes the parameter space, aids in the numerical calculation of the shocks and facilitates understanding of those shocks. The black hole geometry and global magnetosphere have been connected to local shocks. We have gained insight in shock formation without having to compute the solutions. For example, we have found that large compression ratios for fast shocks are excluded.

A systematic categorization of MHD shock solutions around black holes has not been done before. We have seen that it is a useful approach for qualitative understanding of shocks. These categories will likely provide a valuable reference for future research, perhaps as a guide or comparison to isothermal shocks for example.

Table 3.1: Slow shock categories for positive black hole spin. Here, "+" indicates a positive quantity while "-" means a negative quantity. See pages 48–52 for a description of the various cases.

Type	Case	E	L	G_ϕ	σ_1	ζ	B_ϕ	δ/α
I	3	+	+	−	+	>1	−	$1<\zeta<\delta/\alpha<1+\sigma_1$
Imi1	3	+	+	−	+	>1	−	$1<\zeta<\delta/\alpha<1+\sigma_1$
Imi2	4	+	+	−	0	$=1$	0	$1=\zeta=\delta/\alpha$
Imi3	2	+	+	−	−	<1	+	$0<1+\sigma_1<\delta/\alpha<\zeta<1$
Imo	2	+	+	−	−	<1	+	$0<1+\sigma_1<\delta/\alpha<\zeta<1$
IIa1	3	+	−	+	+	>1	+	$1<\zeta<\delta/\alpha<1+\sigma_1$
IIa2	4	+	−	0	0	$=1$	+	$1=\zeta=\delta/\alpha$
IIa3	2	+	−	−	−	<1	+	$0<1+\sigma_1<\delta/\alpha<\zeta<1$
IIb	3	−	−	+	+	>1	+	$1<\zeta<\delta/\alpha<1+\sigma_1$
IIc	2	+	+	−	−	<1	+	$0<1+\sigma_1<\delta/\alpha<\zeta<1$
III	3	+	−	+	+	>1	+	$1<\zeta<\delta/\alpha<1+\sigma_1$

Table 3.2: Additional relationships for slow shock categories, positive spin. The sign of the preshock magnetic energy component must be the same sign as the preshock magnetization. The sign of the difference in toroidal velocities across the shock is always opposite the sign of the preshock toroidal magnetic field component.

Type	E^z_{k1}	E^z_{m1}	$v_2^{\hat\phi}-v_1^{\hat\phi}$	Angular Velocities
I	+	+	+	$0<\omega<\omega_H<\Omega_1<\Omega_2<\Omega_F$
Imi1	<1	+	+	$0<\omega<\omega_H<\Omega_1<\Omega_2<\Omega_F$
Imi2	$=1$	0	0	$0<\omega<\omega_H<\Omega_F<\Omega_1<\Omega_2$
Imi3	>1	−	−	$0<\omega<\omega_H<\Omega_F<\Omega_2<\Omega_1$
Imo	+	−	−	$0<\omega<\omega_H<\Omega_F<\Omega_2<\Omega_1$
IIa1	+	+	−	$0<\Omega_F<\Omega_2<\Omega_1 \gtrless \omega<\omega_H$
IIa2	1	0	−	$0<\Omega_F=\omega<\Omega_2<\Omega_1<\omega_H$
IIa3	+	−	−	$0<\omega<\Omega_F<\Omega_2<\Omega_1<\omega_H$
IIb	+	+	−	$0<\Omega_F<\Omega_2<\Omega_1 \gtrless \omega<\omega_H$
IIc	+	−	−	$0<\omega<\Omega_F<\Omega_2<\Omega_1<\omega_H$
III	+	+	−	$0<\omega<\omega_H,\quad \Omega_F<\Omega_2<\Omega_1$

Table 3.3: Slow shock categories for negative spins. Here, "+" ("-") means greater than (less than) zero. The "Map" column indicates the corresponding positive spin case. Note: there should be a $1-1$ relationship for positive spins.

Type	Map	Case	E	L	G_ϕ	σ_1	ζ	B_ϕ	δ/α
IV	I	3	$+$	$-$	$+$	$+$	>1	$+$	$1<\zeta<\delta/\alpha<1+\sigma_1$
Va1	IIa1	3	$+$	$-$	$-$	$+$	<1	$-$	$1<\zeta<\delta/\alpha<1+\sigma_1$
Va2	IIa2	4	$+$	$-$	0	0	$=1$	$-$	$1<\zeta<\delta/\alpha<1+\sigma_1$
Va3	IIa3	2	$+$	$-$	$+$	$-$	>1	$-$	$0<1+\sigma_1<\delta/\alpha<\zeta<1$
Vb	IIb	3	$-$	$+$	$-$	$+$	>1	$-$	$1<\zeta<\delta/\alpha<1+\sigma_1$
Vc	IIc	2	$+$	$-$	$+$	$-$	<1	$-$	$0<1+\sigma_1<\delta/\alpha<\zeta<1$
VI	III	3	$+$	$+$	$-$	$+$	>1	$-$	$1<\zeta<\delta/\alpha<1+\sigma_1$

Table 3.4: Additional relationships for slow shock categories, negative spin.

Type	E^z_{k1}	E^z_{m1}	$v_2^{\hat\phi}-v_1^{\hat\phi}$	Angular Velocities
IV	$+$	$+$	$-$	$\Omega_F<\omega_H<\omega<0,\ \Omega_F<\Omega_2<\Omega_1$
Va1	<1	$+$	$+$	$\omega_H<\Omega_F<\omega<0,\ \Omega_1<\Omega_2<\Omega_F$
Va2	$=1$	0	$+$	$\omega_H<\Omega_F=\omega<0,\ \Omega_1<\Omega_2<\Omega_F$
Va3	>1	$-$	$+$	$\omega_H<\Omega_F<\omega<0,\ \Omega_1<\Omega_2<\Omega_F$
Vb	$+$	$+$	$+$	$\omega_H<\omega<\Omega_F<0,\ \Omega_1<\Omega_2<\Omega_F$
Vc	$+$	$-$	$+$	$\omega_H<\Omega_F<\omega<0,\ \Omega_1<\Omega_2<\Omega_F$
VI	$+$	$+$	$+$	$\omega_H<\omega<0<\Omega_F,\ \Omega_2<\Omega_1<\Omega_F$

Table 3.5: Fast shock categories for positive spins. Here, "+" ("-") means greater than (less than) zero. See page 53–53 for a description of these cases.

Type	Case	E	L	G_ϕ	σ_1	ζ	B_ϕ	δ/α
I	6	$+$	$+$	$-$	$+$	<1	$-$	$0<\zeta<1<1+\sigma_1<\delta/\alpha$
IIa1	5	$+$	$+$	$-$	$-$	>1	$+$	$0<\delta/\alpha<1+\sigma_1<1<\zeta$
IIa2	7	$+$	$+$	0	0	$=1$	$+$	$\delta/\alpha=1=\zeta$
IIa3	6	$+$	$+$	$+$	$+$	<1	$+$	$0<\zeta<1<1+\sigma_1<\delta/\alpha$
IIb	6	$-$	$-$	$+$	$+$	<1	$+$	$0<\zeta<1<1+\sigma_1<\delta/\alpha$
IIc	6	$+$	$+$	$+$	$+$	<1	$+$	$0<\zeta<1<1+\sigma_1<\delta/\alpha$
III	6	$+$	$-$	$+$	$+$	<1	$+$	$0<\zeta<1<1+\sigma_1<\delta/\alpha$

Table 3.6: Additional relationships for fast shock categories, positive spin.

Type	E^z_{k1}	E^z_{m1}	$v_2^{\hat{\phi}} - v_1^{\hat{\phi}}$	Angular Velocities
I	+	+	−	$0 < \omega < \omega_H < \Omega_2 < \Omega_1 < \Omega_F$
IIa1	+	+	+	$0 < \Omega_F < \omega < \omega_H < \Omega_1 < \Omega_2$
IIa2	1	0	+	$0 < \Omega_F = \omega < \omega_H < \Omega_1 < \Omega_2$
IIa3	+	−	+	$0 < \omega < \Omega_F < \omega_H < \Omega_1 < \Omega_2$
IIb	+	+	+	$0 < \Omega_F < \Omega_1 < \omega \gtrless \Omega_2 \gtrless \omega_H$
IIc	+	+	+	$0 < \Omega_F < \omega < \omega < \Omega_1 < \Omega_2 \gtrless \omega_H$
III	+	+	+	$\omega_H < \omega < 0 < \Omega_F,\ \Omega_1 < \Omega_2 < \Omega_F$

CHAPTER 4

SLOW MAGNETOSONIC SHOCKS IN THE EQUATORIAL PLANE

'Results! Why, man, I have gotten a lot of results. I know several thousand things that won't work.' – Thomas A. Edison

Introduction

In this chapter we present, finally, examples of MHD shocks produced by our model. Typical shocks for all flow types are shown, as well as the asymptotic case, where the effects of general relativity are minimal. Although an effort has been made to explain the behavior of the shocks, attempting to isolate specific cause and effect results, such as "a large black hole spin produces strong shocks" is very difficult to do given the large number of parameters. The other obvious difficulty in identifying general relativistic effects is that the metric coefficients are endemic to the equations. The most profitable approach is to compare shocks occurring in different flow types, as these already take into account the curvature and spin effects.

Throughout this chapter we restrict ourselves to slow magnetosonic shocks, which must be located between the plasma source (r_I) and the Alfvén point (r_A). Thus we will consider only the sub-Alfvénic accretion ($M < M_{\rm A}$) of a transfast MHD accretion solution. The cold preshock accretion is superslow magnetosonic, the postshock accretion is hot, having been heated at the shock. The slow magnetosonic wave speed in the hot plasma is nonzero, $(u_{\rm SM})_2 > 0$ so that the postshock accretion must satisfy the condition

$0 < u_{p2} < (u_{\rm SM})_2$ at the shock location; that is, the postshock flow must be subslow magnetosonic. All of the preshock accretion flows presented are physically acceptable flows in the sense that the critical condition (as shown in Figure 2.2) is satisfied.

Effects of Black Hole Spin

To see the general shock behavior as a dependence on the hole's spin a, we present solutions to the coupled equations (2.109) and (2.13) for a range of black hole spins, both positive and negative. For computational reasons (namely speed and accuracy in calculation of Bessel functions), instead of equation (2.13) we use a polynomial approximation given by Service (1986):

$$\Gamma = \frac{1}{3}(5.0 - 1.21937z + 0.18203z^2 - 0.96583z^3 + 2.32513z^4 - 2.39332z^5 + 1.07136z^6) \ , \quad (4.1)$$

where

$$z \equiv \frac{\Theta}{0.24 + \Theta} \ . \quad (4.2)$$

Figure 4.1 displays the polytropic index as a function of temperature while Figure 4.2 shows the estimated fractional error in Γ using equation (4.1). This indicates that the polynomial approximation is clearly adequate for our purposes.

There are several free parameters, including the four conserved quantities E, L, Ω_F, and η. To limit the confusion, as we vary the spin we keep two of the conserved quantities constant. Fixing L and Ω_F would prevent the formation of shocks (because valid flows could not be obtained) across the entire spin range, so E and η were held constant. For

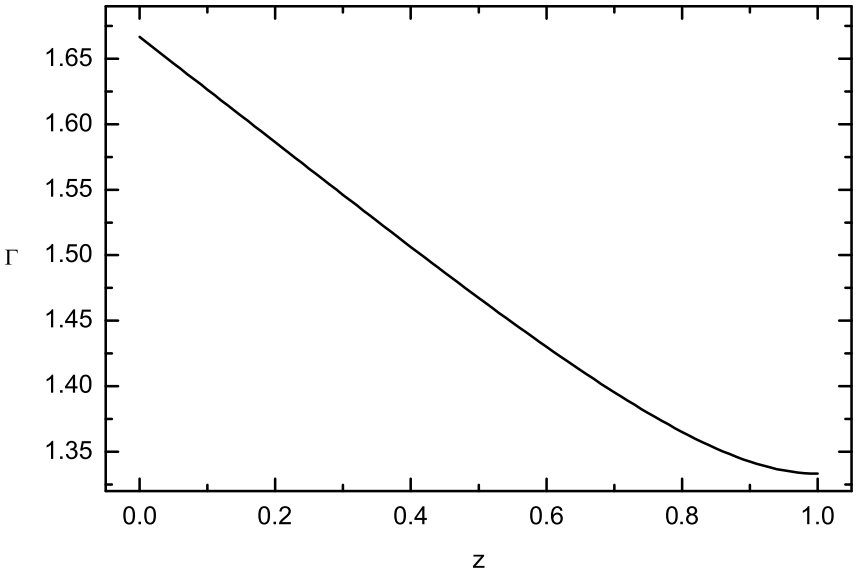


Figure 4.1: The polytropic index as a function of temperature according to Services's polynomial approximation where $z = \Theta/(0.24 + \Theta)$. The abscissa varies from nonrelativistic at $z = 0$ to ultrarelativistic at $z = 1$.

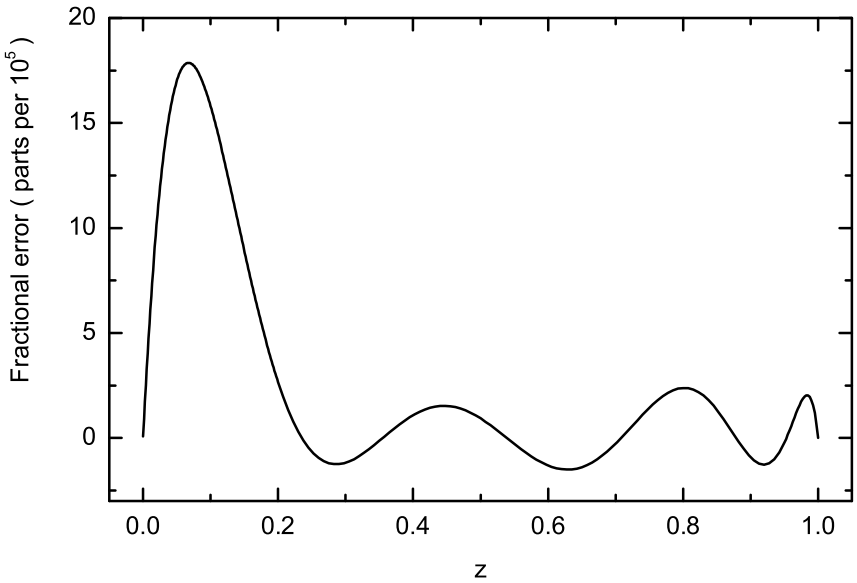


Figure 4.2: Estimated fractional error for the fitting formula, equation (4.1), of the polytropic index Γ. The error is zero at both the extreme nonrelativistic ($\Gamma = 5/3$) and extreme relativistic ($\Gamma = 4/3$) limits.

Table 4.1: Conserved quantities for the accreting plasma

Symbol	Physical Description	Definition
Ω_F	Angular velocity of the magnetic field lines	Eq. (2.17)
E	Total energy measured by a distant observer	Eq. (2.30)
L	Total angular momentum measured by a distant observer	Eq. (2.31)
η	Particle number flux per magnetic flux tube	Eq. (2.18)

Table 4.2: Important Radial Locations

Symbol	Description	Definition
r_H	Black Hole Horizon	Eq. (2.2)
$r_{\rm st}$	Static Limit	Eq. (2.3)
r_L	Light Cylinder	Eq. (2.48)
r_F	Fast Point	Eq. (2.53)
r_A	Alfv́en Point	Eq. (2.49)
r_S	Slow Point	Eq. (2.53)
r_I	Injection Point	Eq. (2.65)
$r_{\rm sp}$	Separation Point	Eq. (2.63)

convenience, the description of the conserved quantities are given in Table (4.1). The trans-fast MHD accretion solutions were then obtained by letting L (and thus e) decrease rapidly with increasing spin a (Table 4.3). Here, we should note that the radii of $r = r_{\rm H}$, $r = r_{\rm F}$, $r = r_{\rm L}$, $r = r_{\rm A}$ and $r = r_{\rm I}$ are different for each flow solution; for larger spin a, the region of $r_{\rm A} < r < r_{\rm inj}$, where the slow magnetosonic shock is expected, becomes narrow and shifts inward (toward the horizon).

For numerical quantities the radial coordinate, black hole spin and magnetosphere angular velocity will be scaled by the black hole mass, m, ($r \to r/m$, $a \to a/m$, $\Omega_F \to m\Omega_F$). The energy, angular momentum and particle flux through a flux tube will be scaled by the particle mass, m_p, ($E \to E/m_p$, $L \to L/(mm_p)$ and $\eta \to m_p\eta$. Note that $[L] = cm^2$ so it has been scaled by black hole mass and particle mass. This scaling will be indicated explicitly in tables but not figures.

Table 4.3: Parameter set for cold trans-fast MHD accretion solutions, where $E/\mu_1 = 1.0062$ and $\mu_1\eta = 0.04133$ and $\mu_1 = m_{part}$ (for a cold flow).

a/m	$L/\mu_{\rm c}$	$m\Omega_F$	r_H/m	$r_{\rm L}/m$	$r_{\rm F}/m$	$r_{\rm A}/m$	$r_{\rm inj}/m$	$r_{\rm sp}/m$
0.95	2.470	0.3691	1.312	1.314	1.320	1.335	1.439	1.457
0.30	3.950	0.1096	1.954	1.964	1.970	2.022	3.694	4.270
0.00	5.147	0.0519	2.000	2.022	2.067	2.093	5.283	7.188
−0.20	7.332	0.0278	1.980	2.029	2.030	2.102	6.197	10.943
−0.40	11.275	0.0148	1.916	2.026	1.870	2.096	7.093	16.618
−0.70	22.283	0.0055	1.714	2.016	1.739	2.074	9.307	32.176
−0.90	40.823	0.0026	1.436	2.009	1.444	2.050	10.834	53.658

Figure 4.3 shows the effect of black hole rotation on the nature of the accretion flow and shock strength. The spin parameters selected are $a = 0.95$, 0.3, 0.0, −0.2, −0.4, −0.7, and −0.9. For this parameter set we always have $\Omega_F > \omega_H$ so the flows are of Type I ($a > 0$) or Type VI ($a < 0$). Furthermore, all flows are Case 3 as defined in Chapter 3 (see Tables 3.1–3.4). In the figures the solid curves are for minimum spin, $a = -0.9$, and the spin increases to a maximum of $a = 0.95$ as indicated on the graph. Positive a refers to black hole and magnetosphere corotation (i.e., $\Omega_F > 0$), while negative a implies counter-rotation. One effect on the flow is that for negative spins a larger angular momentum is required. This tends to reduce the maximum radial velocity of the flow, even though the injection point moves steadily outward for decreasing spins.

Figure 4.3 indicates that for flows with nonrelativistic velocities, near the injection point, $\xi \approx 4$ for all spins—a typical result for such flows. In the nonrelativistic limit, the compression ratio is given by $\xi(\Gamma) = (\Gamma + 1)/(\Gamma - 1)$; then $\xi(5/3) = 4$. For a radiation dominated fluid, $\Gamma = 4/3$, and $\xi_{\rm max} = 7$, but this does not necessarily mean relativistic flows. Shocks occurring in the formalism of the relativistic Rankine-Hugoniot relations, (Taub, 1948; Thorne, 1973), can have a diverging compression ratio (Liang, 1977; Anile,

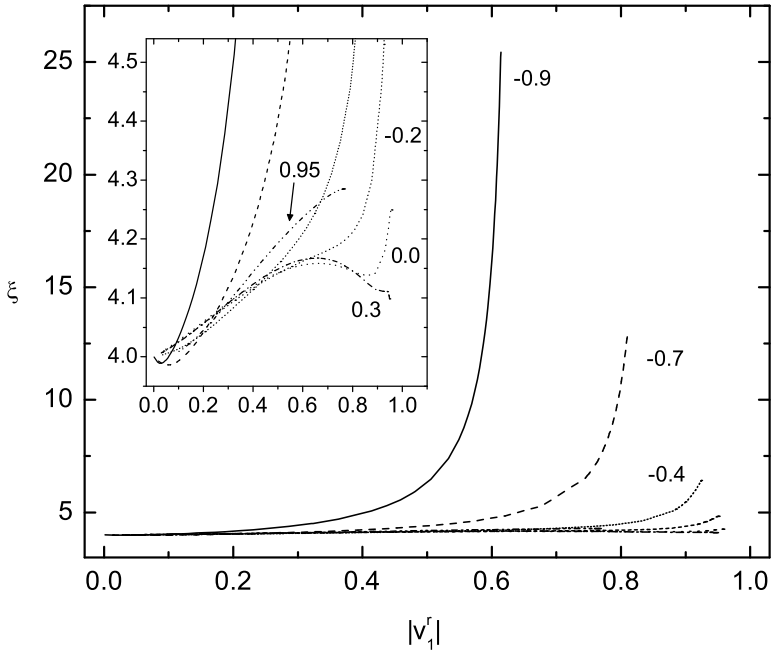


Figure 4.3: The compression ratio as a function of the preshock radial velocity where the velocity is given in units of c. There is a dramatic difference in shock strength between corotating and counter-rotating black holes.

Miller & Motta, 1983).

As Figure 4.3 clearly shows, the compression ratio can greatly exceed the "Newtonian" limit. When ξ is large, Figure 4.4 clearly indicates that the polytropic index is approximately 4/3. In this case the flow is extremely relativistic. We have not yet explained the compression ratio's strong dependence on black hole spin. Near the injection point, far from the horizon, we would not expect spin to be important and that is the case. But even for the $a = 0.95$ situation, where the injection point is within the ergosphere, the compression ratio seems to be unaffected by spin. However, the figure clearly indicates a strong correlation of ξ with black hole spin when the shock occurs near the Alfvén point. So its going to take more work to explain this dependence.

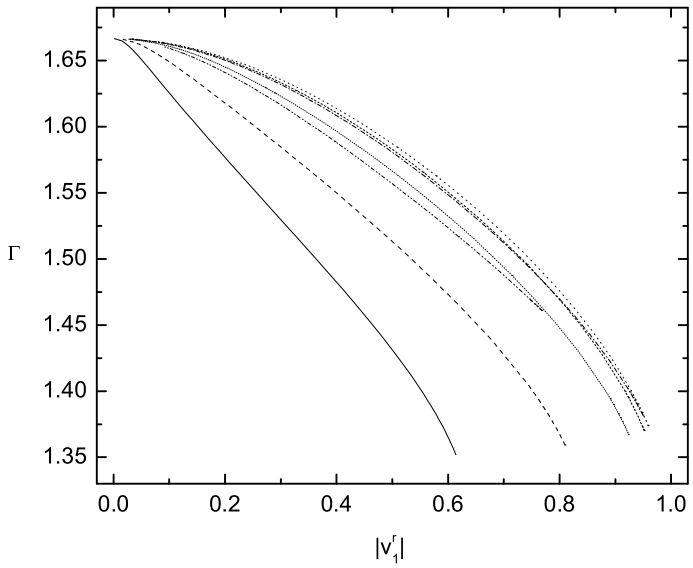


Figure 4.4: The polytropic index as a function of preshock radial velocity. It varies from 5/3 at the injection point to approximately 4/3 near the Alfvén point. The curve labelling is the same as in Figure 4.3.

The reason for the extremely large compression ratio is revealed in the defining equation (2.96), $\xi \equiv (n_2 u_2^t)/(n_1 u_1^t)$. Figure 4.5 shows that the number density ratio increases uniformly with velocity but the rate of increase is greater for negative spins. Also, Figure 4.6 indicates that although the ratio u_2^t/u_1^t does not have a large absolute change, the general decreasing trend with velocity is reversed abruptly for the most negative spins. This is not a very satisfying explanation for the behavior of ξ; postshock quantities are still involved and effects of the black spin are not evident.

A better approach is found by writing the compression ratio as $\xi = (M_1/M_2)^2\zeta$. The squared Alfvén Mach number ratio never exceeds four, as shown in Figure 4.7 and decreases rapidly near the Alfvén point, where the compression ratio is largest. The large values for ξ are then due to large values for ζ, as indicated in Figure 4.8. Although this explanation still involves postshock quantities, we have seen in Chapter 3 that Case 3

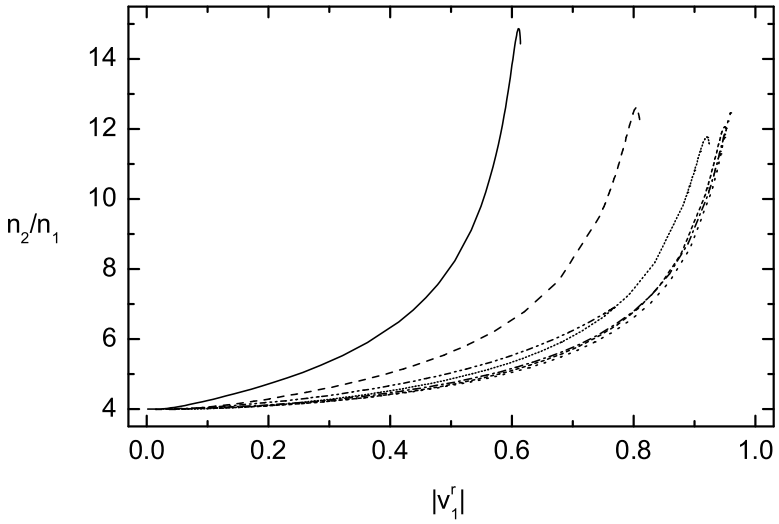


Figure 4.5: The number density ratio vs. radial velocity for the flows listed in Table 4.3. The curve labelling is the same as in Figure 4.3.

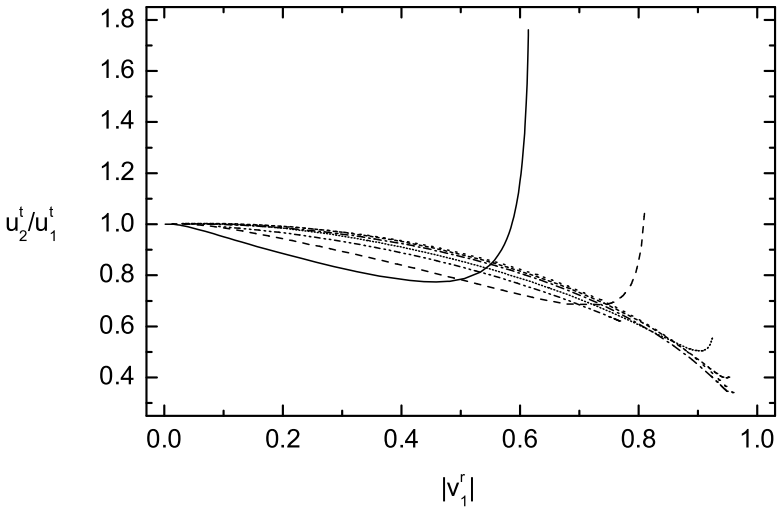


Figure 4.6: The ratio of the time-component four-velocities vs. radial velocity. Only for large negative spins is there a significant difference. The curve labelling is the same as in Figure 4.3.

flows can have large compression ratios only for large ζ. So at least a prediction of large ξ could have been made. In addition, we also know that the preshock magnetization must be large; this is verified in Figure 4.9. The compression ratio can be directly related to the preshock magnetization by writing

$$\xi = \frac{M_1^2}{M_2^2}[1 + (1-q)\sigma_1] \ , \tag{4.3}$$

where we have used equations (2.96) and (2.97). When $r_{sh} \approx r_I$, the shock is weak, $q \to 1$, so that $\xi \approx M_1^2/M_2^2$. This ratio always has a maximum of about four. For stronger shocks, when $r_{sh} \approx r_A$, we have $q \to 0$ and $\xi \approx (M_1/M_2)^2(1+\sigma_1)$. Thus, for large magnetization, the compression ratio is proportional to σ_1. Using equation (2.92) the magnetization can be written as

$$\sigma = \frac{(\tilde{L} - l)(\Omega_F - \omega)}{(1 - \Omega_F \tilde{L})(1 - \omega\ell)} \ . \tag{4.4}$$

Although the magnetization is a plasma/magnetosphere parameter, the effect of the black hole geometry is incorporated directly via ω. Indirectly, the geometry is contained in ℓ and puts limitations on the values of $\tilde{L}$ that give valid flow. The magnetization can become arbitrarily large when $\Omega_F \tilde{L} \to 1$; this occurs as the flow approaches the light cylinder (see Figure 3.7). But there are other ways to obtain a large magnetization. The term $1 - \omega\ell$ is never very small, but for large negative black hole spins, ℓ and ω both become negative as the flow moves inward from the injection point (see Figure 4.10). Then, in the numerator, ℓ and ω enhance $\tilde{L}$ and Ω_F, respectively. This will enhance the preshock magnetization. Finally, we have already seen that for valid flow, $\tilde{L}$ increases

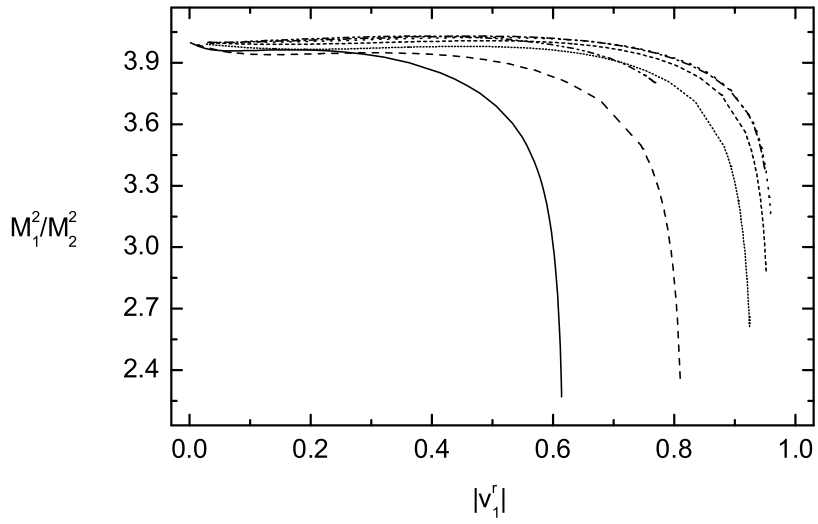


Figure 4.7: The ratio of the Alfvèn Mach numbers vs. radial velocity for Table 4.3 shocks. The curve labelling is the same as in Figure 4.3.

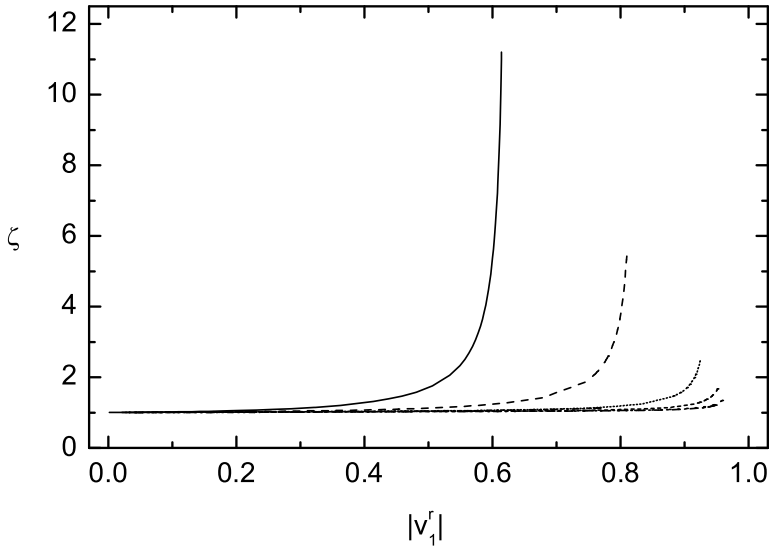


Figure 4.8: ζ vs radial velocity for Table 4.3 shocks. The curve labelling is the same as in Figure 4.3.

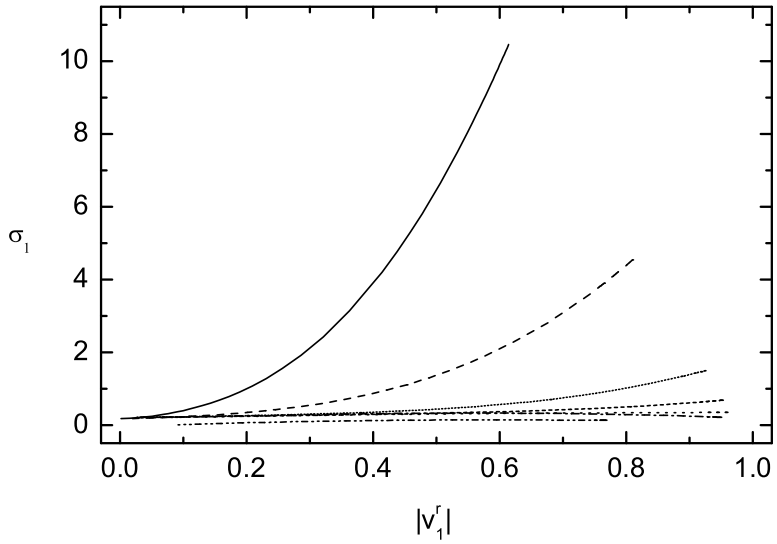


Figure 4.9: Preshock magnetization vs. radial velocity for Table 4.3 shocks. The curve labelling is the same as in Figure 4.3.

dramatically as the spin became more negative. Thus, the black hole spin can be seen to affect the magnetization in several ways and this in turn is directly related to the shock strength.

Another important quantity is the postshock temperature, shown in Figure 4.11. For this parameter set the temperature trend is similar to the compression ratio trend. A weak shock does not produce much heating, as expected, regardless of spin. Strong shocks give significant heating and there is a correlation with spin. To see why this happens, it is useful to look at the magnetic fields and energies of the plasma on both sides of the shock. Figures 4.12 and 4.13 show the ZAMO toroidal magnetic fields on either side of the shock. These fields are given by

$$B^{\hat{\phi}} = \frac{u^t_z}{g_{\phi\phi}} B_\phi \ , \tag{4.5}$$

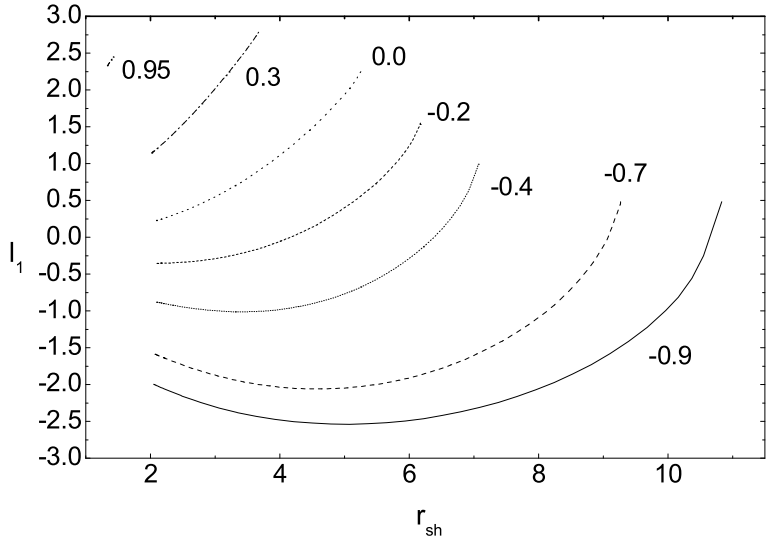


Figure 4.10: Preshock specific angular momentum vs. shock location.

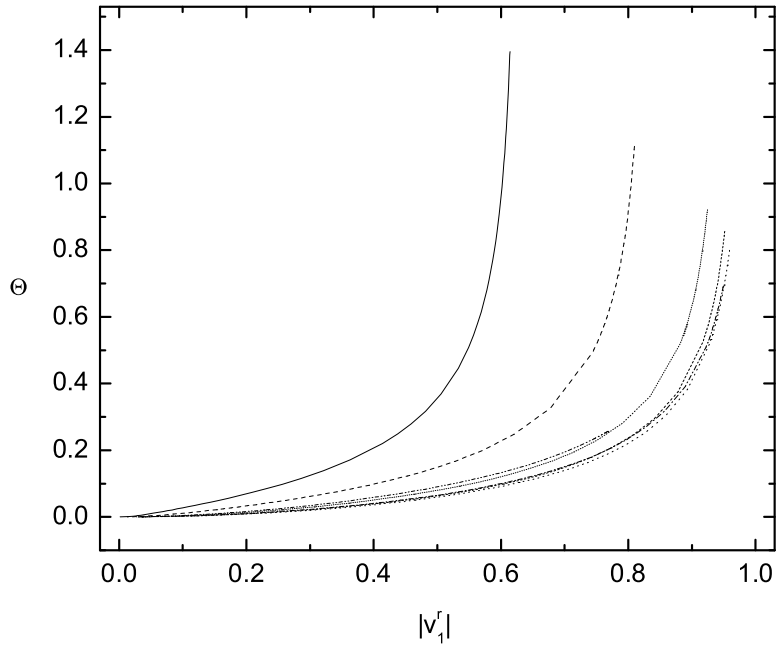


Figure 4.11: The temperature parameter of the postshock flow, $\Theta = kT/m_{\rm p}c^2$ vs. radial velocity. For all flows, the temperature rises rapidly as the shock location approaches the Alfvén point. This occurs regardless of the behavior of the compression ratio.

where $u^\alpha = (u^t, 0, 0, u^\phi)$ is the four-velocity of a ZAMO and

$$u^t_{\rm z} = (g^{tt})^{1/2} = \left(\frac{-g_{\phi\phi}}{\rho_w^2} \right)^{1/2} \quad . \tag{4.6}$$

At the injection point this field component, for all flows, is approximately the same; the negative spin flows have values a bit larger due to the large L required for valid flows. The field is positive throughout the flow for all spins. Also, for every flow, the field increases as the flow moves inward, especially near the Alfvén point. In Figure 4.13 we see that the postshock field follows roughly the same behavior, only with smaller values, as it be must for slow shocks. The exception occurs near the Alfvén point where the field drops to zero indicating a switch-off shock (see Chapter 6). Strong shocks occur when the preshock toroidal field is large and the postshock field is very small.

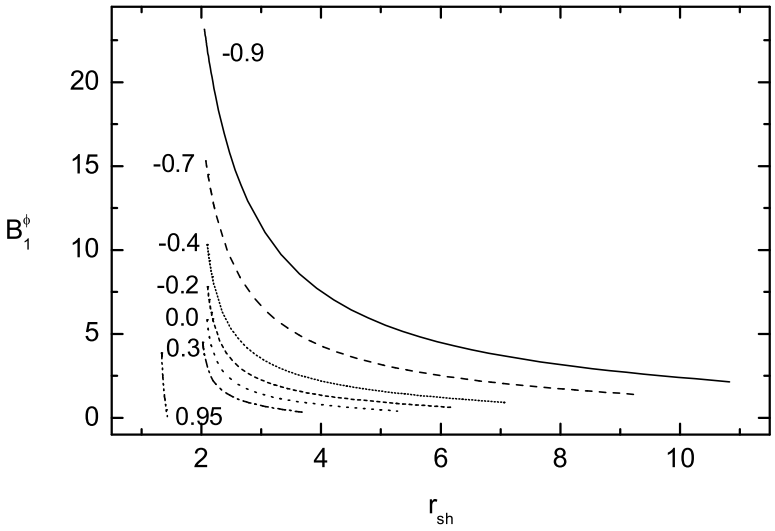


Figure 4.12: Preshock azimuthal magnetic field in the ZAMO frame vs. shock location. The curve labelling is the same as in Figure 4.3.

Next, we can look at the energetics of the shock. The ZAMO energy of the flow is

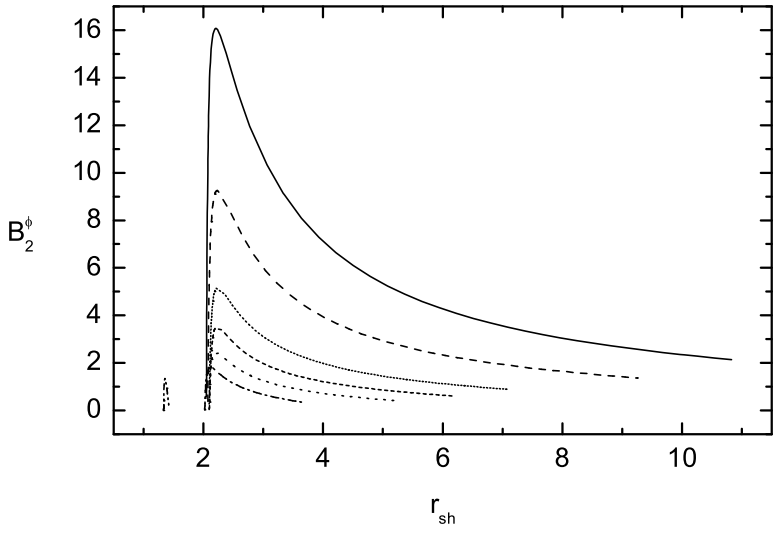


Figure 4.13: Postshock azimuthal magnetic field in the ZAMO frame vs. shock location. The curve labelling is the same as in Figure 4.3. Notice that for the innermost radial location of each shock, the field component becomes very small. This is indicative of a switch-off shock, where the postshock tangential magnetic field component vanishes. This will be discussed in chapter 6.

given by (see, for example, Schutz, 1985),

$$E_{\rm z} = u_{\rm z}^t (E - \omega L) \ . \tag{4.7}$$

This energy is positive-definite, implying $E > \omega L$, and does not change across the shock as shown in equation (2.85). Figure 4.14 shows the ZAMO energy of the flow for each spin case. Near the injection point all the flows have $E_{\rm z} \approx E$ because curvature and spin effects are small there. But near the Alfvén point the ZAMO energy increases and is much greater for the negative spin cases. This is due mainly to spin ($\omega < 0$) so that the two terms in equation (4.7) are additive. With such a large energy it is no surprise that the negative spin cases can produce so much heating in the postshock flow.

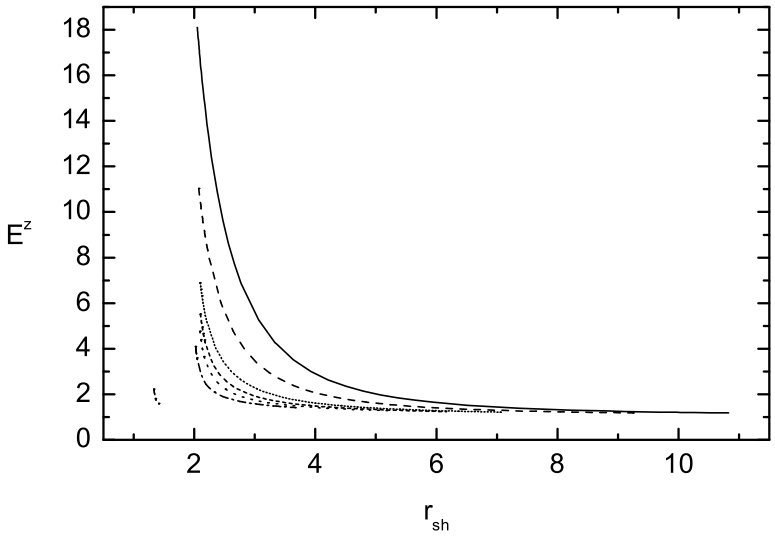


Figure 4.14: The energy of the accreting flow in the ZAMO frame. For a given flow, it remains constant across a shock. There is much more energy available for heating the plasma as the black hole spin decreases. The curve labelling is the same as in Figure 4.3.

Looking at the magnetic contribution to the total ZAMO energy for both preshock and postshock flows in Figures 4.15 and 4.16 further clarifies the situation for this parameter set.[1] They are given by

$$E^z_{Mi} = u^t_z \left(\frac{\Omega_F B_{\phi i}}{4\pi\eta} \right) (\omega - \Omega_F) \qquad i = (1, 2) \ . \tag{4.8}$$

These relations are derived in Appendix B. Near the injection point, all flows (except the $a = 0.95$ case) have both a preshock and postshock magnetic component of approximately 20%. So there is not a large reservoir of magnetic energy available to be converted at the shock. But this component steadily increases as a smaller (more negative) black hole spin is selected and, generally, as the flow moves inward.

[1]The preshock flow is cold so that the total energy can be divided into two terms: kinetic and magnetic. The postshock flow is hot; this means that while the magnetic contribution can still be easily separated, the kinetic and thermal cannot be so easily distinguished.

Very near the Alfvén point the magnetic energy component of the preshock flow for the $a = -0.95$ case is greater than 90%. But this energy is almost entirely converted to kinetic+thermal energy. The fluid is severely accelerated in the toroidal direction by the shock, as shown by Figures 4.17 and 4.18; this acceleration also produces significant heating of the plasma. The details of this process are hidden for an infinitely thin shock. Tokar et al. (1986) considered electron heating in studies of high Mach number perpendicular collisionless shocks. Papadopolous (1986) proposed electron heating in an electron-ion plasma from a consideration of plasma instabilities. A similar investigation but treating the ions and electrons as particles was done by Shimada & Hoshino (2000). For a review of the physics of electron heating at collisionless shocks, see Scudder (1995).

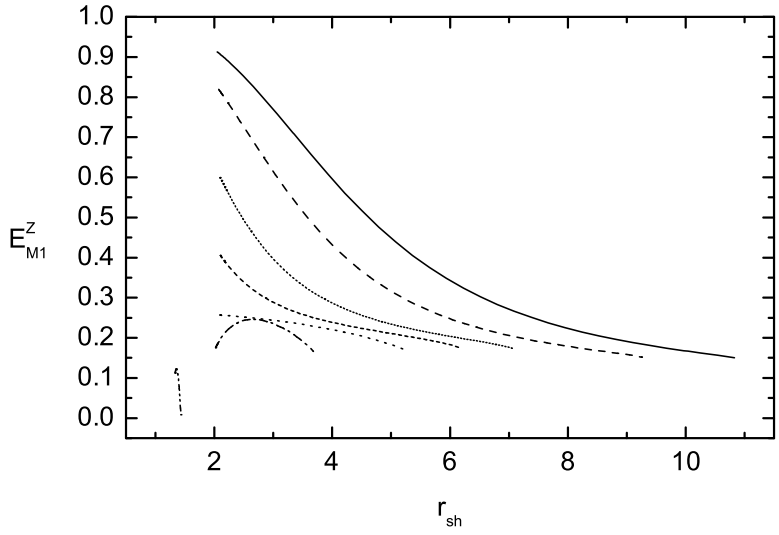


Figure 4.15: Preshock magnetic energy fraction in the ZAMO frame vs. shock location. The curve labelling is the same as in Figure 4.3. The most negative spin case has the largest magnetic energy component.

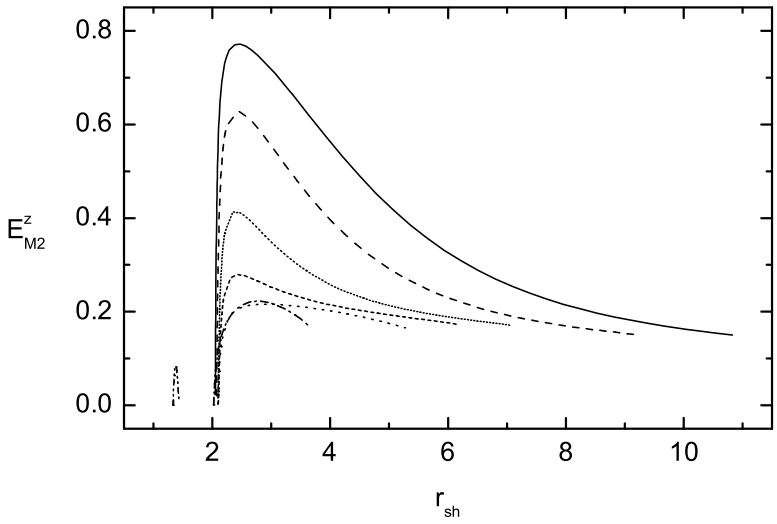


Figure 4.16: Postshock magnetic energy fraction in the ZAMO frame vs. shock location. In all cases this term approaches zero as the shock location nears the Alfvén point.

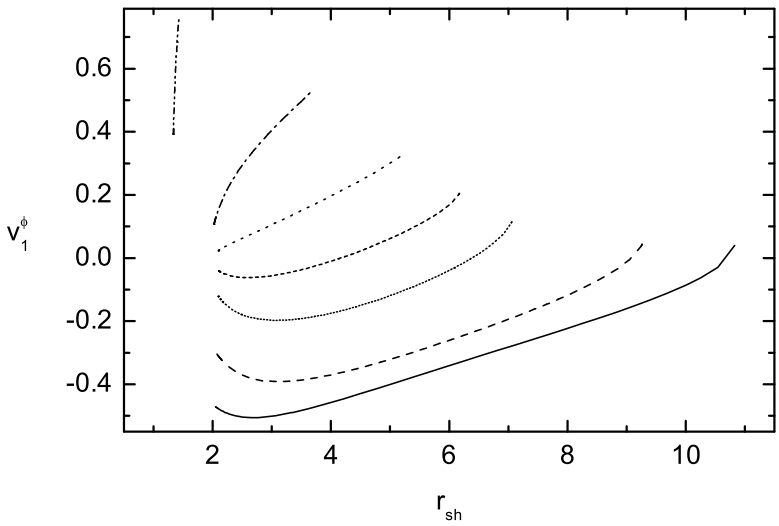


Figure 4.17: Preshock plasma toroidal velocity in the ZAMO frame vs. shock location. The curve labelling is the same as in Figure 4.3.

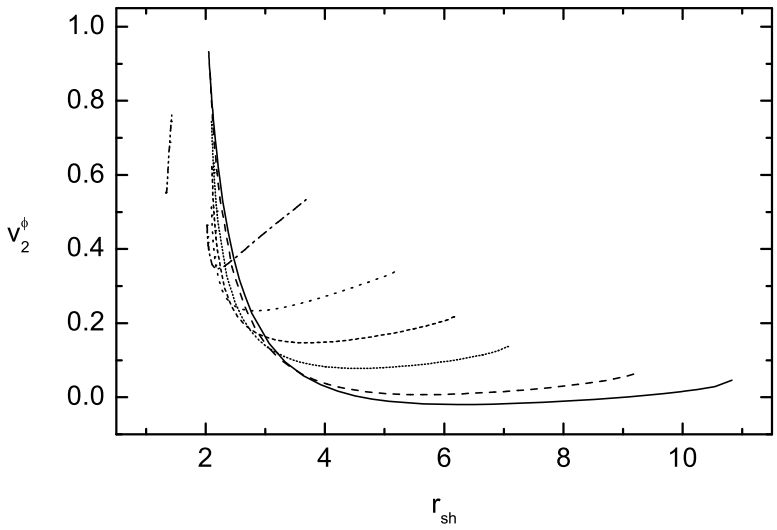


Figure 4.18: Postshock plasma toroidal velocity in the ZAMO frame vs. shock location.

Magnetization Effects

We now move on to another example of strong shocks. We have already discussed that a strong shock can occur if the preshock flow has a large magnetization. A negative spin is not required; as equation (4.4) indicates, we can simply force a large magnetization by choosing $\Omega_F \tilde{L} \approx 1$. Figure 4.19 shows such a solution where the conserved quantities are given in Table 4.4. In this case there is a large positive spin ($a = 0.8$) and the only way to obtain a large magnetization is by choosing a rapidly rotating magnetosphere, ($\Omega_F = 92\%\ \Omega_F^{\max}$), along with a large angular momentum. Then not only is most of the energy in the magnetic term, as the figure indicates, the total energy is extremely large, $E_z \approx 1400$. The results are similar to the first parameter set given, but now the entire shock region lies within the ergosphere.

The magnetic energy content in the accreting flow has a significant effect on slow shock

Table 4.4: Parameter set for Type I cold trans-fast MHD accretion solutions in the magnetically dominated limit ($\Omega_F \tilde{L} \approx 1$). The black hole spin is $a = 0.8$, $\mu_1 \eta = 0.00075$ and $\Omega_F \tilde{L} = 0.9995$.

E/μ_c	L/μ_c	$m\Omega_F$	r_H/m	r_L/m	r_F/m	r_A/m	r_{inj}/m	r_{sp}/m
65.03	228.68	0.2842	1.6	1.62358	1.60025	1.6237	1.6276	1.948

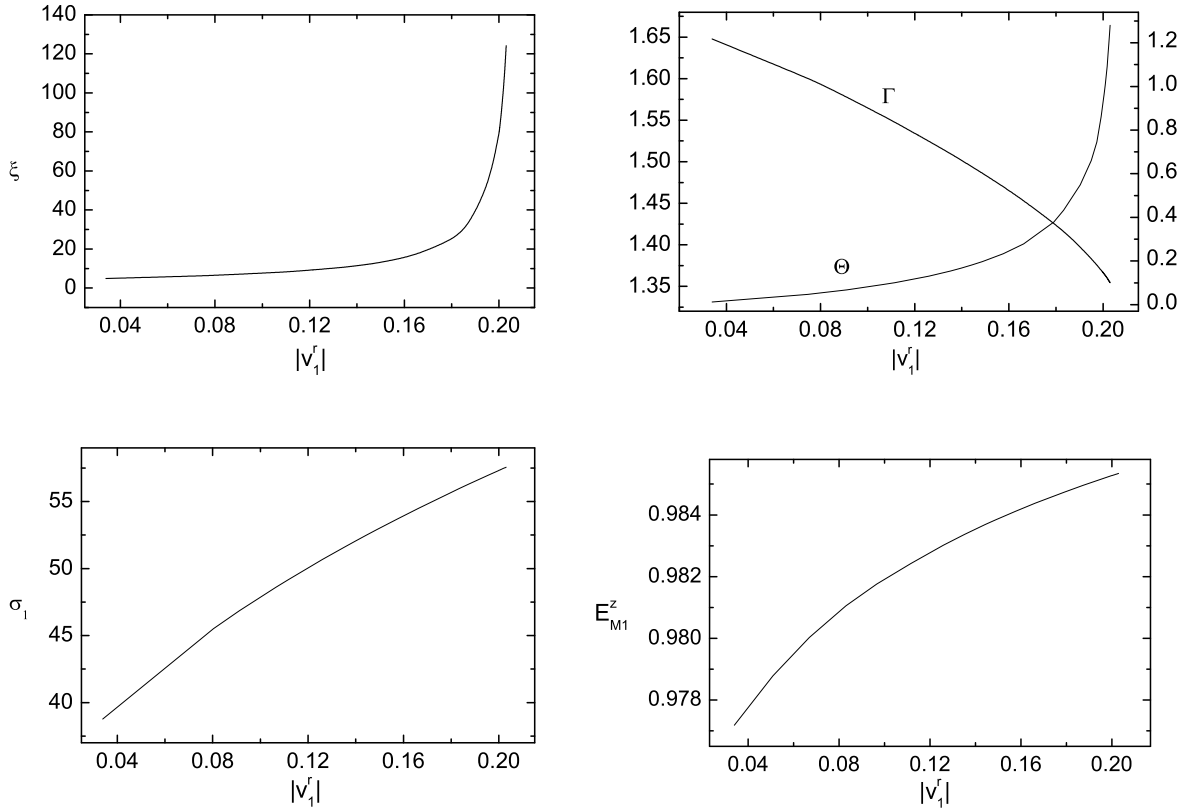


Figure 4.19: A slow magnetosonic shock for extreme magnetization ($\Omega_F \tilde{L} \approx 1$). For this situation the compression ratio is large even for small radial velocities.

behavior. A simple way to isolate this effect is to choose zero black hole spin and modify the conserved quantities Ω_F and $\tilde{L}$. Figure 4.20 presents four slow shocks for flows with varying magnetic energy. One flow is the $a = 0$ case given in Table 4.3; it has a maximum preshock magnetic energy component of $E_{M1}^{max} \approx 25\%$. The next two flows were obtained by searching for the maximum magnetic energy component possible by varying only either $\tilde{L}$ or Ω_F. In both cases the varied quantity increased as indicated in Table 4.5. Both of

Table 4.5: Parameter set for cold trans-fast MHD accretion solutions with varying magnetic energy component, E_M, where $a = 0$. Shock #1 is the same shock solution as the zero spin case in Table 4.3 with $E_{\rm M1}^{\rm max} \approx 25\%$. Shocks #2 and #3 have $E_{\rm M1}^{\rm max} \approx 55\%$ while shock #4 has $E_{\rm M1}^{\rm max} \approx 6\%$.

Shock	$E/\mu_{\rm c}$	$L/\mu_{\rm c}$	$\tilde{L}$	$m\Omega_F$	$\Omega_F\tilde{L}$	$r_{\rm L}/m$	$r_{\rm F}/m$	$r_{\rm A}/m$	$r_{\rm inj}/m$
1	1.0062	5.147	5.115	0.0519	0.265	2.022	2.067	2.093	7.19
2	1.2854	6.575	5.115	0.1161	0.594	2.130	2.098	2.263	4.20
3	1.4784	15.863	10.730	0.0519	0.557	2.022	2.018	2.041	7.19
4	0.4664	2.118	4.541	0.1021	0.464	2.096	2.259	2.259	4.58

these flow have $E_{\rm M1}^{\rm max} \approx 55\%$.

Finally, we let both Ω_F and $\tilde{L}$ vary in such a way as to produce the smallest magnetic energy component. This flow has only $E_{\rm M1}^{\rm max} \approx 6\%$. There is a distinct correlation of compression ratio with magnetic energy, as expected. The larger angular momentum of shock #3 allows the shock location to occur closer to the light cylinder by moving the Alfvén point inward, producing the greater temperature. Although plotting the temperature parameter Θ versus the radial velocity makes it difficult to identify the individual shocks solutions, it was done so specifically to show that the postshock temperature is strongly dependent on the preshock radial velocity.

Type II Shocks

We now discuss slow shock formation in Type II flows. As discussed in the previous chapter, this type applies to a slowly corotating magnetosphere, $0 < \Omega_F < \omega_H$. The relationships and signs of many quantities are given in Tables 3.1 and 3.2. Seven typical shocks are presented, two for each subtype, along with one solution that spans the three divisions of subtype IIa. A moderately large black hole spin, $a = 0.8$, was chosen to gener-

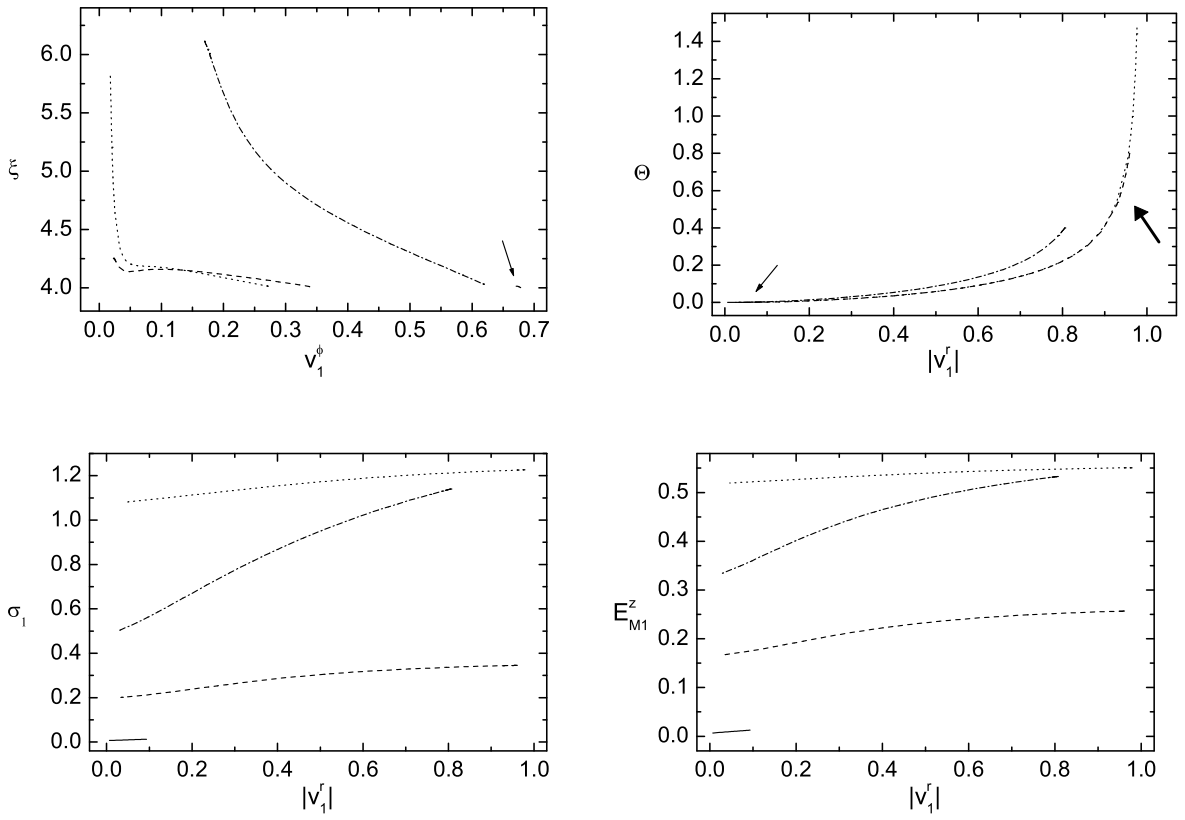


Figure 4.20: Slow magnetosonic shocks with varying magnetic energy. The shocks are identified with Table 4.5: 1 (Dash), 2 (Dot-Dash), 3 (Dot), 4 (Solid). The small arrow locates Shock #4 and the large arrow locates Shock #1.

ate an ergosphere wide enough for easy numerical exploration. The conserved quantities and location of critical points are given in Table 4.6. Note that Type IIb shocks must form entirely within the ergosphere, Type IIc shocks form entirely outside the static limit and Type IIa shocks are not restricted to be inside or outside the ergosphere.

Figure 4.21 shows the compression ratio as a function of radial velocity and ζ for the Type II shocks listed in Table 4.6. The Type IIb and IIa1 shocks are relatively strong compared to the others. This is because they have positive magnetization so that there is positive ZAMO magnetic energy available. They also have a larger ζ and are all Case 3. So once again, by using the shock categories we could have predicted this result. Figure 4.22

Table 4.6: Parameter set for Type II cold trans-fast MHD accretion solutions.

Shock	Type	E/μ_c	L/μ_c	$m\Omega_F$	$\Omega_F\tilde{L}$	r_L/m	r_F/m	r_A/m	r_{inj}/m
1	IIb	-0.173	-2.539	0.135	1.9805	1.701	1.692	1.746	1.762
2	IIb	-0.085	-2.724	0.098	3.1518	1.761	1.763	1.819	1.829
3	IIa1	0.039	-1.839	0.120	-5.7087	1.724	1.731	1.820	1.872
4	IIa3	0.742	-0.019	0.050	-0.0013	1.862	1.903	3.044	4.723
5	IIa123	0.120	-1.821	0.168	-2.5262	1.657	1.678	1.752	2.300
6	IIc	0.487	0.052	0.146	0.0154	1.685	1.855	2.048	2.505
7	IIc	0.746	0.443	0.055	0.0329	1.850	2.001	3.479	4.366

shows that these are the only flows with a negative toroidal velocity; because $v_2^{\hat{\phi}} - v_1^{\hat{\phi}} < 0$, this means that the flow is accelerated across the shock (as opposed to decelerated) and this tends to give stronger shocks. Type IIa1 and IIa3 flows, while being quite similar in parameter space, give shocks with qualitatively different behavior. As expected, the shock for Type IIa123 flow behaves like #5 at low velocities (near the injection point) and like #3 at higher velocities (near the Alfvén point). The temperature profiles are all very similar, as usual, implying that for Type II shocks the heating is mostly a function of radial velocity. Shocks #4 and #7 depart somewhat from the trend, producing more heating for a given velocity. This appears to be due to the small magnetic energy component: at the same preshock plasma radial velocity the magnetization is almost zero (Figure 4.23). Shock #5 has by far the largest temperature and also, the largest radial velocity. The behavior of the Type IIa123 flow is best seen in Figure 4.23 where the point at which Type IIa2 flows exists ($\sigma_1 = \sigma_2 = 0$).

Type III Shocks

The remaining shock category is Type III shocks, for which we include a few sample shock solutions. The conserved quantities for each flow are given in Table 4.7. The energy

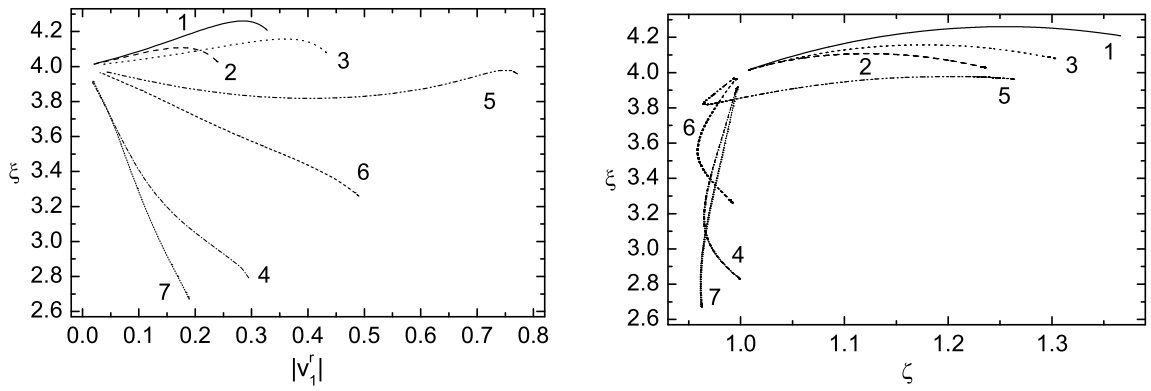


Figure 4.21: Compression ratio for Type II slow magnetosonic shocks as a function of radial velocity and ζ. The shocks are labelled in accordance with Table 4.6.

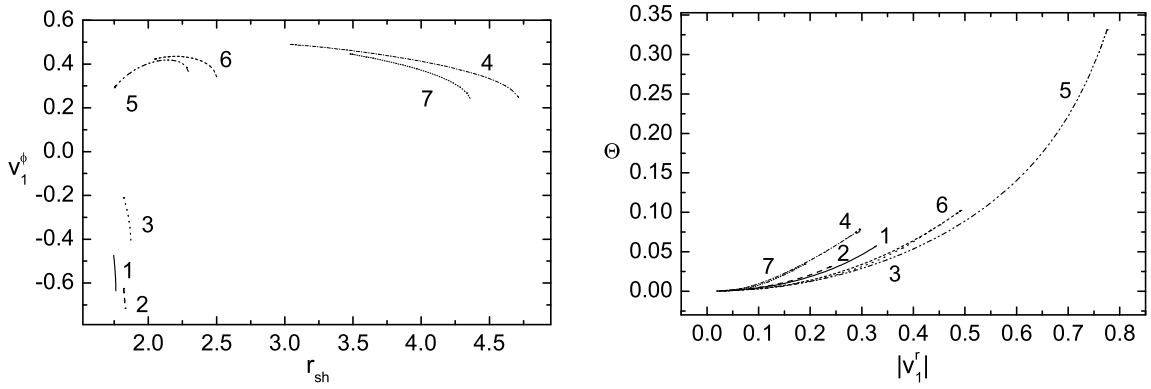


Figure 4.22: Toroidal velocity vs. shock location and temperature parameter vs. radial velocity for Type II slow magnetosonic shocks. The shocks are labelled in accordance with Table 4.6.

for each flow was chosen to be very close to the energy of the first parameter set (see Table 4.3). Two black hole spins were selected, $a = 0.0,\ 0.8$. Recall that for Type III flows the magnetosphere is rotating opposite to the SMBH. Then the toroidal velocity of the preshock flow decreases in magnitude as it accretes, as indicated in Figure 4.24. Type III shocks must be Case 3 and, in agreement with previous results, the compression ratio is $\xi \gtrapprox 4$. Similarly, the radial velocity never gets large, producing little heating.

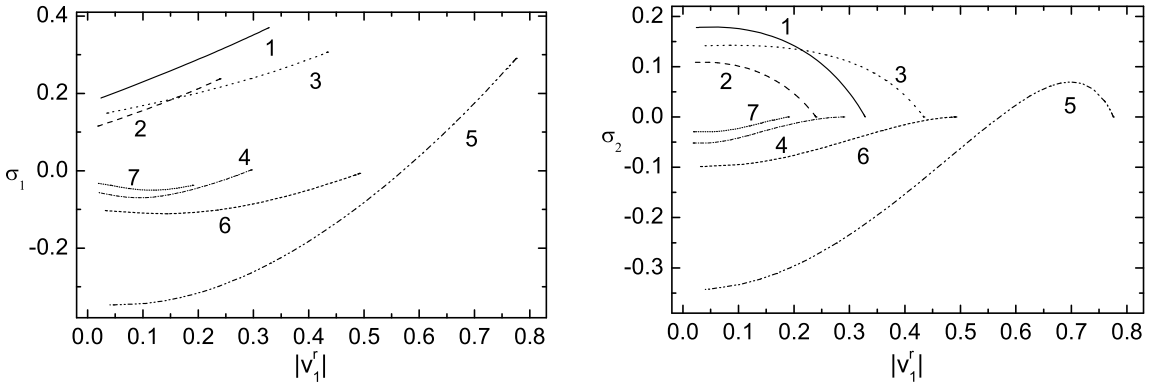


Figure 4.23: Preshock and postshock magnetization vs. radial velocity for Type II slow magnetosonic shocks. The shocks are labelled in accordance with Table 4.6.

Table 4.7: Parameter set for Type III cold trans-fast MHD accretion solutions.

Shock	a	$E/\mu_{\rm c}$	$L/\mu_{\rm c}$	$m\Omega_F$	$\Omega_F\tilde{L}$	$r_{\rm L}/m$	$r_{\rm F}/m$	$r_{\rm A}/m$	$r_{\rm inj}/m$
1	0.0	1.0056	-4.76	-0.1559	0.738	2.293	2.401	2.539	3.452
2	0.0	1.0062	-5.45	-0.1516	0.821	2.268	2.338	2.375	3.517
3	0.8	1.0062	-6.05	-0.1152	0.697	2.657	3.030	3.051	4.480
4	0.8	1.0063	-5.48	-0.1151	0.631	2.656	3.271	3.307	4.482

Shock #1, with the smallest magnitude angular momentum, has the largest radial velocity and the largest temperature. The figure also shows that the compression ratio is greatest for the largest $\Delta\Omega = \Omega_2 - \Omega_1$. This is consistent with the acceleration at the shock front converting radial kinetic energy to toroidal kinetic energy. Due to counter-rotation, the black hole spin causes the shock location to be pushed farther from the horizon. For the given choice of conserved quantities, the magnetic energy content is so small that very strong shocks do not occur. However, it is likely that such a shock could be formed for Type III shocks as we already have seen examples of very strong Type VI shocks, which map 1-1 with Type III shocks.

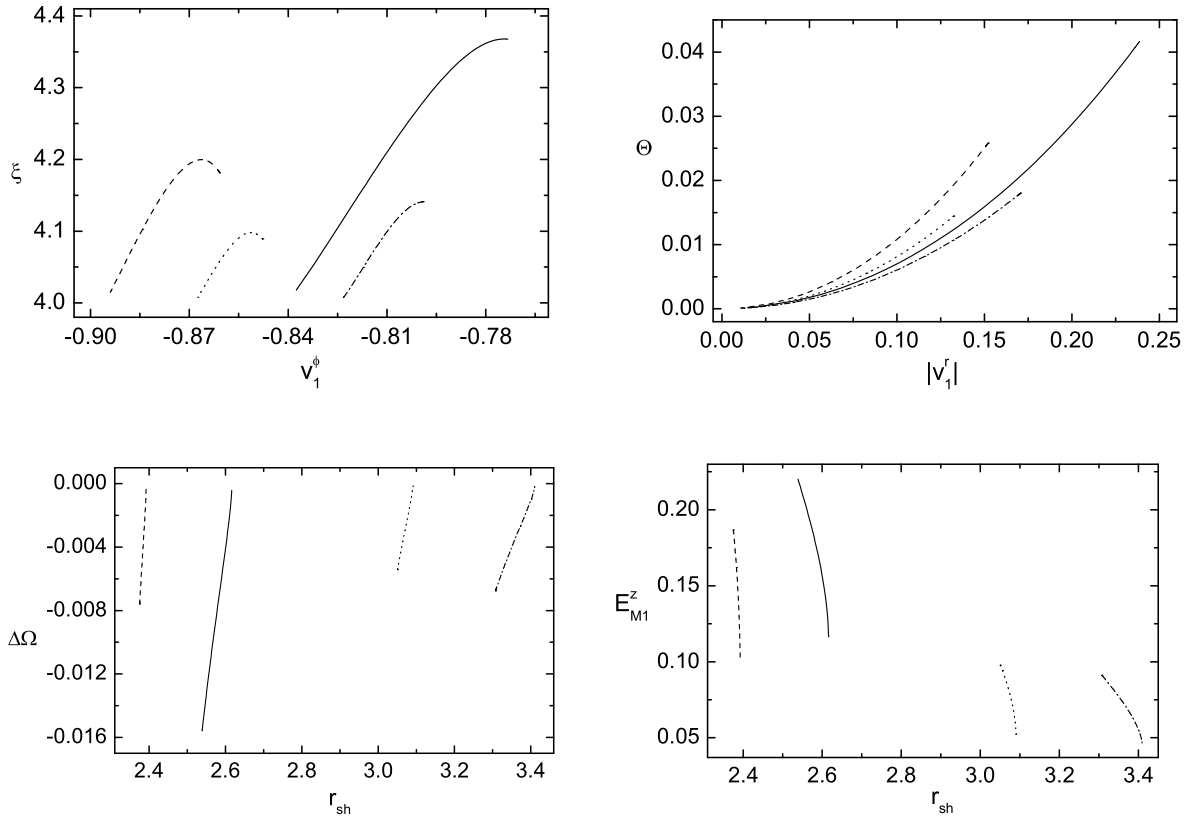


Figure 4.24: Type III slow magnetosonic shocks. The shocks are identified with Table 4.7: 1 (Solid), 2 (Dash), 3 (Dot), 4 (Dash-Dot).

Asymptotic Limit

The equations derived in Chapter 2 reduce to the corresponding equations in AC88 in the limit of no plasma rotation and weak gravity ($\Omega_1 = 0$,$m = 0$, $a = 0$). As a check on the derivation and solution method, we present in Figure 4.25 the results for the asymptotic case of $a = 0$, $\Omega_1 \approx 0$ and slowly rotating magnetosphere, $\Omega_F \approx 0$. A set of parameters for this situation, given in Table 4.8, places the injection point far from the black hole so that the shock range is quite large.

Because the Alfvén point is close to the horizon, the weak gravity limit fails there.

Table 4.8: Parameter set for cold trans-fast MHD accretion solutions in the asymptotic limit ($\Omega_1 = 0$, $m = 0$, and $a = 0$).

E/μ_c	L/μ_c	$m\Omega_F$	r_H/m	r_L/m	r_F/m	r_A/m	r_{inj}/m	r_{sp}/m
1.002	14.995	0.0019	2.0	2.00003	2.001	2.00103	43.64	64.6

We cannot try to take the comparison too far because AC88 presented fast magnetosonic shocks while here we are looking only at slow shocks (see Chapter 7 for fast shock results). For this shock solution, the maximum values for several preshock quantities and ζ are: $(\Omega_1)_{max} < 0.002$, $(\sigma_1)_{max} < 0.03$, $\zeta_{max} < 1.0004$, $(E_M^z)_{max} < 3\%$. The results are consistent with those obtained by AC88. The only serious apparent difference between our results and those by AC88 is that their r (our ξ) and $\Pi \to 0$ sharply as their $\beta \to 0$, while our ξ and Π do not drop off sharply as $v_1^r \to 0$. However, the reason is well understood if we are aware of the complication caused by our non-zero v_1^ϕ. In our case when v_1^r approaches 0 our β does not get small due to the contribution by large v_1^ϕ.

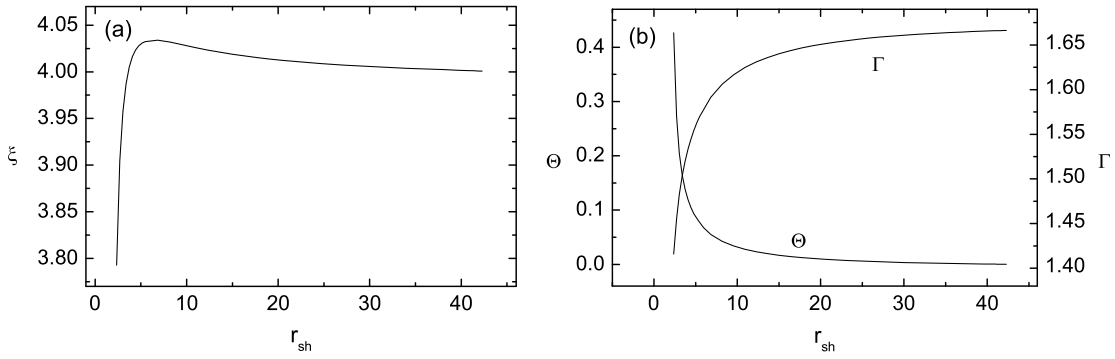


Figure 4.25: (a) Shock frame compression ratio ξ and (b) polytropic index Γ and temperature parameter Θ as functions of shock location in the limit of no plasma rotation and weak gravity ($\Omega_1 = 0$, $m = 0$, $a = 0$).

Summary

The purpose of this chapter was to present and discuss the first shock solutions of the general relativistic version of MHD shock conditions for plasma accreting onto a rotating black hole. The examples were restricted to the equatorial plane for uniformity and to limit complicating effects. In addition, only cold preshock flows were allowed and a split-monopole magnetic field was assumed. Typical slow magnetosonic shocks for each category were discussed.

It was shown that the existence of a black hole vastly increases the complexity of the shock landscape. The rotation of the black hole generates the various flow types, with restrictions on the initial parameters. This subsequently affects the possible shock location due to the location of critical points. Furthermore, the interaction of the black hole spin and magnetosphere rotation is exposed at the shock front. The efficiency of fluid acceleration, both transverse and normal, and the efficiency of magnetic energy conversion are strongly correlated with this interaction.

Finally, a comparison with MHD shocks in a flat spacetime yield encouraging results. Shocks occurring where the effects of the black hole are small behave similarly to their special-relativistic counterparts. But when curvature effects are strong, the richness of the model becomes evident. The following chapters continue the exploration of the model.

CHAPTER 5

SLOW MAGNETOSONIC SHOCKS IN THE POLAR REGION

'Polar exploration is at once the cleanest and most isolated way of having a bad time which has yet been devised.' – A. Cherry-Garrard

Introduction

The previous chapter dealt with shocks occurring for flows restricted to the equatorial plane. Although this was sufficient for a detailed investigation of shock formation in our theory, it is not particularly relevant for typical astrophysical conditions. Generally, in the vicinity of an AGN, the equatorial plane is expected to contain an accretion disk where the assumptions for our model fail. For example, the split monopole magnetic field is strictly valid only for the open interval $\theta = (0, \pi/2)$, thereby excluding the axis and equatorial plane.[1] However, as mentioned in Chapter 1, a primary reason for conducting this research was the possibility of MHD in the polar[2] region of an AGN as a source of X-rays for irradiation of iron atoms in the accretion disk. Therefore, now that we have discussed the particulars of equatorial slow shocks, it is time to explore magnetosonic shock formation in the polar region.

To begin, we ask two questions: (1) can our model produce shocks near the axis and, (2) if so, are these shocks qualitatively different than equatorial shocks? The concise answers

[1]Technically the split monopole field is defined on the open intervals $(0,\pi/2)$ and $(\pi/2, \pi)$, i.e., the field is also defined in the 'southern' hemisphere.

[2]By 'polar' we mean non-equatorial. So we do not restrict flows to be arbitrarily close to the spin axis; rather, we are consider the entire non-equatorial region and investigate the effects of the polar angle on the MHD accretion conditions.

are yes and no, respectively. This chapter will expand on these answers in detail. We first need to investigate the restrictions that apply to plasma flows located off the equatorial plane. Because if the locations of the critical points do not allow for transmagnetosonic flow there can be no shock. Another aspect of polar flows that we need to consider is the angular momentum distribution in relation to the boundary condition on the spin axis.

Behavior of Critical Points

As was mentioned previously, a shock is a local phenomenon: its properties are only indirectly related to its global position. But shock behavior is a function of the preshock flow and this relationship was investigated in the previous chapter. So we start by asking "Why should an accreting plasma in the polar region be any different than flows at the equator?" To answer this question we need to realize that for our model, any differences between equatorial and non-equatorial flows can be due only to geometry. By this we mean not only the spacetime geometry but the configuration of the flow (namely, angular momentum) and the boundary conditions of the magnetic field.

The general relativistic frame-dragging, expressed by the metric term $g_{t\phi}$, depends strongly on polar angle ($g_{t\phi} \propto \sin^2\theta/(r^2 + a^2\cos^2\theta)$), so any effects on the system due to it will diminish rapidly for decreasing polar angles. As the axis is approached, the static limit approaches the horizon, possibly having a significant effect on Type II shocks. Also, a flow near the axis must necessarily have a relatively small mechanical angular momentum in order to accrete onto the black hole. So the first step in studying polar MHD shocks is to investigate the effects of the geometry on the critical points[3]. If the

[3]In this chapter we will use the term 'critical points' loosely. Strictly speaking, only r_F, r_S and r_A are

critical points do not exist, in the correct order, there will be no shock.

The simplest way to begin is to consider the "easy" critical points first. The separation point, the light cylinder and the Alfvén point, equations (2.63), (2.48), and (2.49), respectively, are all functions of $\tilde{L}$ and Ω_F. By specifying only these quantities we can plot the critical point locations as a function of $(r,\, \theta)$. This will help identify the allowed parameter space for valid preshock flow as a function of polar angle. Note that this method will not guarantee a shock solution: first $(E,\, L)$ have to be specified independently to obtain an injection point and then a fast point must be determined by choosing η. There is no guarantee that a pair of conserved quantities $(\tilde{L},\, \Omega_F)$ producing an acceptable set $(r_L,\, r_A,\, r_{\rm sp})$ will also yield an acceptable $(r_F,\, r_I)$. Nevertheless, we can obtain criteria on flow parameters that can aid in the search for polar shocks.

The Kerr metric is quite complicated due to the black hole spin and accompanying frame-dragging effects. It is useful to get some insight on the critical point behavior in an easier situation. Therefore, as a first step, we consider the Schwarzschild case for which the forms of the critical point equations are simple enough to be studied analytically. For zero spin the light cylinder, Alfvén point, and separation point must satisfy the following relations:

$$r_L(a=0): \qquad \frac{(r_L-2)}{r_L} = \Omega_F^2 \rho_L^2 \ , \tag{5.1}$$

$$r_A(a=0): \qquad \tilde{L}\frac{(r_A-2)}{r_A} = \Omega_F \rho_A^2 \ , \tag{5.2}$$

$$r_S(a=0): \qquad r_S^3 \Omega_F^2 \sin^2\theta = 1 \ , \tag{5.3}$$

critical points of the flow. The light cylinders, injection point and separation point are *not* critical points.

where $\rho \equiv r \sin\theta$ is the cylindrical radius. Equation (5.1) shows, as we saw in the previous chapter for equatorial flows, that one way to obtain a large outer light cylinder and hence the possibility of a distant injection point is to make Ω_F exceedingly small. It also shows that near the axis ($\theta \to 0$) the inner light cylinder nears the horizon, $r_H = 2$, and the outer light cylinder becomes arbitrarily large. With polar flows allowing for the possibility of a large r_I independently of Ω_F, we begin to see a hint that slow shocks may occur over a large range in the polar regions far more readily than in the equatorial plane.

Continuing, equation (5.2) indicates that for intermediate angles and $r \gg r_H$, the cylindrical radius increases with $\tilde{L}$, as one might expect. If the flow has too much angular momentum, it cannot accrete onto the black hole. Near the axis we find two possibilities for the inner Alfvén radius: (i) either $\tilde{L} \to 0$ or (ii) $r_A \to r_H$. The first case would imply that magnetically dominated flows would be absent near the axis while the second implies that slow shocks could occur arbitrarily close to the horizon. Finally, equation (5.3) shows that the separation point can become arbitrarily large near the pole. Taken together, these results give a clear indication that, for zero spin at least, there is the potential for slow shocks over a much greater range near the axis than the equatorial plane. For extreme spins the situation is more complicated near the horizon. But the effects of spin will diminish as the radial distance from the black hole increases because $g_{t\phi} \propto a/r$. So the analysis in the zero spin case should carry over to arbitrary spins, for $r \gg r_H$.

Now consider the effect of the polar angle on the location of the critical points when the spin is not zero. It is easiest to see this with pictures. Figures 5.1 through 5.5 show polar plots of the inner light cylinder, Alfvén radius and separation point for different spins and flow types. The light cylinder and separation point are independent of $\tilde{L}$ so it

is convenient to hold Ω_F fixed and change $\tilde{L}$ to see patterns.

Figure 5.1 displays a number of interesting features for Type I flows. The light cylinder remains close to the horizon for all angles but the separation point becomes roughly parallel to the spin axis at small angles. Thus the possible slow shock range is greatly enhanced in the polar regions. For small angles, an Alfvén point exists for any value of $\tilde{L}$. But only for small values of $\tilde{L}$ can the Alfvén point move to a large radial distance. This in turn implies that intense shocks can occur far from the black hole in the polar regions only if the flow has small angular momentum. At larger angles, the number of Alfvén points strongly depends on the angular momentum and/or black hole spin. For example, with only a small change in spin, from $a = 0.0 \rightarrow 0.3$, the $\tilde{L} = 3.1$ solution gives either zero or two Alfvén points near the equator. Of course, if $\tilde{L}$ is held constant, the same argument holds for Ω_F.

The situation for Type II flows is much different and more complicated due to the three subtypes allowed. In Figure 5.2, the behavior for two Type IIa flows indicates that multiple inner Alfvén points do not exist. There is not a great difference in Alfvén point behavior as a function of angle for either flow. Unlike Type I flows, the r_A-curves bend down to the equator so a large r_A in the polar regions will not occur. Notice that due to the counter-rotation, a relatively large angular momentum is allowed near the axis. There is an interesting "dip" very close to the spin axis. This behavior is due to G_t and G_ϕ. From the defining equation for the Alfvén point, equation (2.49),

$$G_\phi = -\tilde{L} G_t \quad \text{for} \quad r = r_A \ ,$$

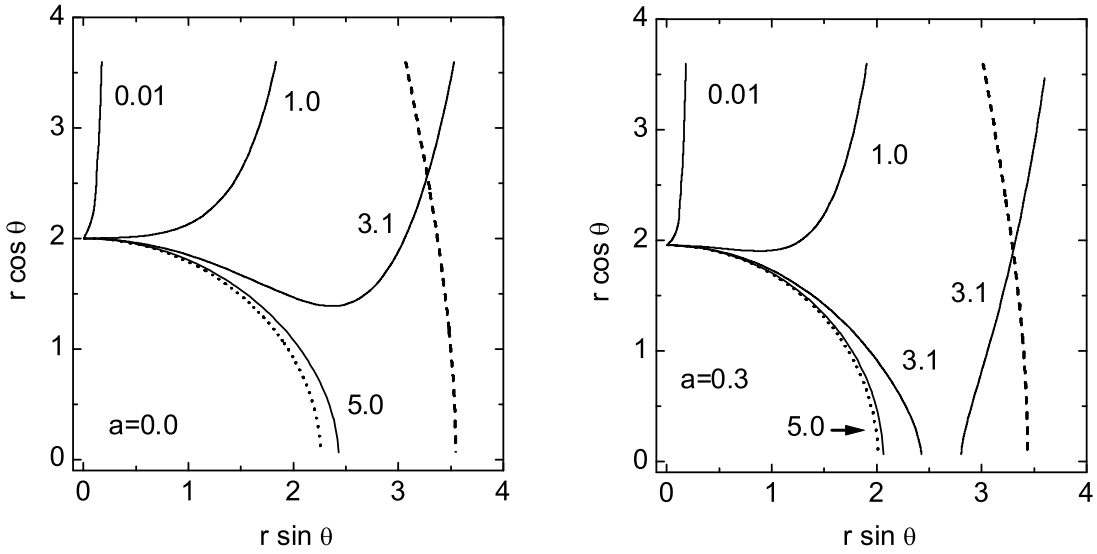


Figure 5.1: Polar plots of r_L (dotted), r_A (solid) and $r_{\rm sp}$ (dashed) for four Type I flows. Each r_A curve is labelled by $\tilde{L}$ and $\Omega_F = 0.15$. A constant Ω_F means that r_L and r_{sp} For clarity the horizon is not drawn; it is located at $r_H(0) = 2.0$ and $r_H(0.3) = 1.954$. The number of Alfvén points for a given set of initial parameters can strongly depend on the polar angle.

the location of the Alfvén point for small angles and nonzero $\tilde{L}$, is determined by

$$\lim_{\theta\to 0} G_\phi = 0 \qquad \lim_{\substack{\theta\to 0 \\ r\to r_H}} G_t = 0 \ . \tag{5.4}$$

So the Alfvén point, if it exists, must approach the horizon for small angles. This is true for all flow types. The exception is if the angular momentum is allowed to vanish as $\theta \to 0$. Then the Alfvén point does not necessarily approach the horizon for small angles. We will see an example of this later in the chapter.

Next, Type IIb flows are shown in Figure 5.3. These flows are similar to Type IIa flows but, as discussed in Chapter 2, the Alfvén point must lie within the ergosphere. So even extreme values of $\tilde{L}$ do not significantly alter the picture. Accretion flows for the

last subcategory, Type IIc are shown in Figure 5.4. The value for Ω_F was specifically chosen to be close to $\omega_H(a = 0.7)$. Then, for small enough $\tilde{L}$, the shock regions depends strongly on polar angle. Near the equator, the region is small; as the angle decreases, the shock region gradually increases. At some critical angle (here, about 30°), the r_A-curve breaks away from the light cylinder and eventually intersects with the separation point. Depending on the location of the injection point, the shock region could be very small but far away from the black hole. At even smaller angles, the Alfvén point vanishes and valid flow is not possible. With $a = 0.99$, the large $\tilde{L}$ flow has ceased to be valid at any angle: one r_A-curve is now inside the light cylinder and the other is now entirely outside the injection point.

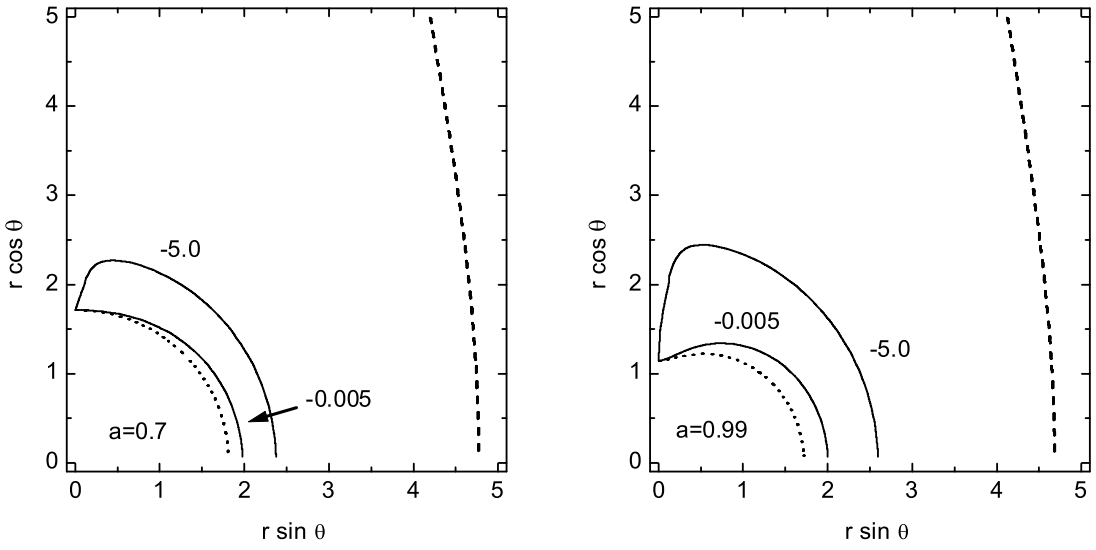


Figure 5.2: Polar plots of r_L (dotted), r_A (solid) and $r_{\rm sp}$ (dashed) for two Type IIa flows. Each r_A curve is labelled by $\tilde{L}$ and $\Omega_F = 0.09$. The horizon is located at $r_H(0.7) = 1.714$ and $r_H(0.99) = 1.141$.

Finally, the behavior of Type III flows is shown in Figure 5.5. This situation is very similar to Type I flows except that the inner light cylinder is pushed farther away from

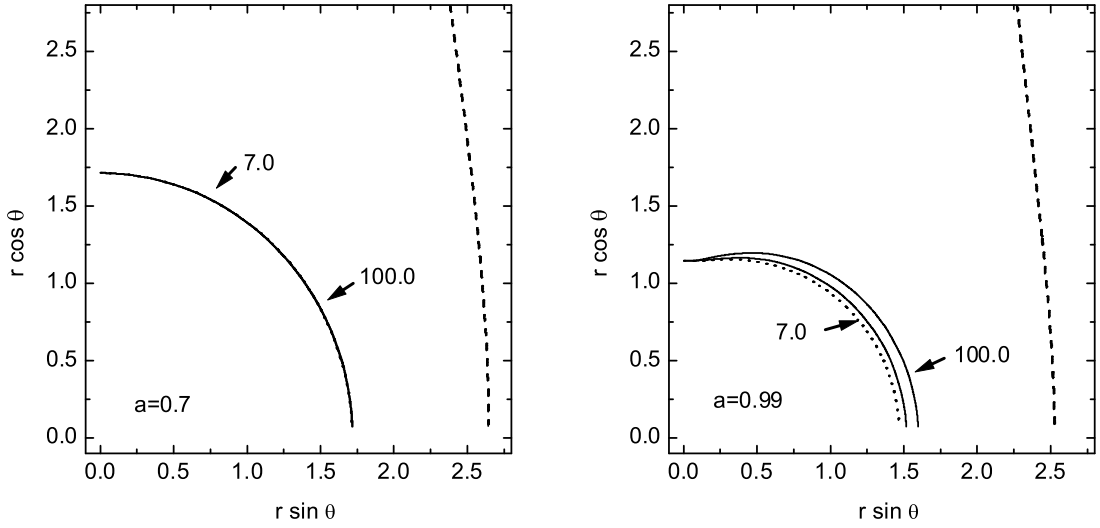


Figure 5.3: Polar plots of r_L (dotted), r_A (solid) and $r_{\rm sp}$ (dashed) for two Type IIb flows. Each r_A curve is labelled by $\tilde{L}$ and $\Omega_F = 0.2$. The horizon is located at $r_H(0.7) = 1.714$ and $r_H(0.99) = 1.141$. For the $a = 0.7$ case, the curves for the inner light cylinder and Alfvén are so close they appear as a single curve.

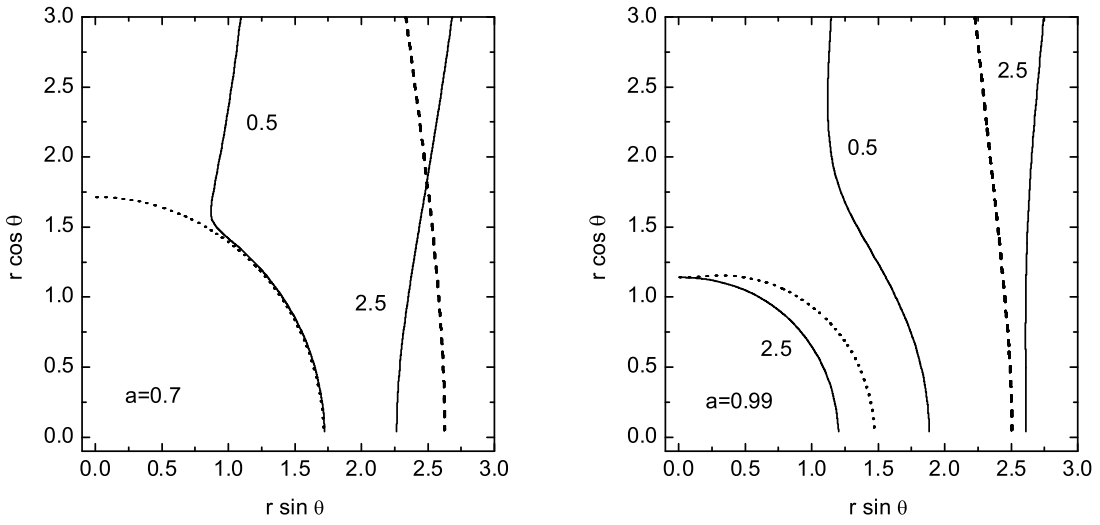


Figure 5.4: Polar plots of r_L (dotted), r_A (solid) and $r_{\rm sp}$ (dashed) for two Type IIc flows. Each r_A curve is labelled by $\tilde{L}$ and $\Omega_F = 0.202$. The horizon is located at $r_H(0.7) = 1.714$ and $r_H(0.99) = 1.141$. For spin $a = 0.99$, the $\tilde{L} = 2.5$ flow has no valid Alfvén point.

the horizon. The effect is a function of polar angle and near the equatorial plane, the light cylinder can cease to exist for a large spin. Then an Alfvén point is not possible, as indicated by the $\tilde{L} = -6.55$ curve, and this region is excluded from shock formation. Although certainly not exhaustive of the range of initial conditions, the figures do show

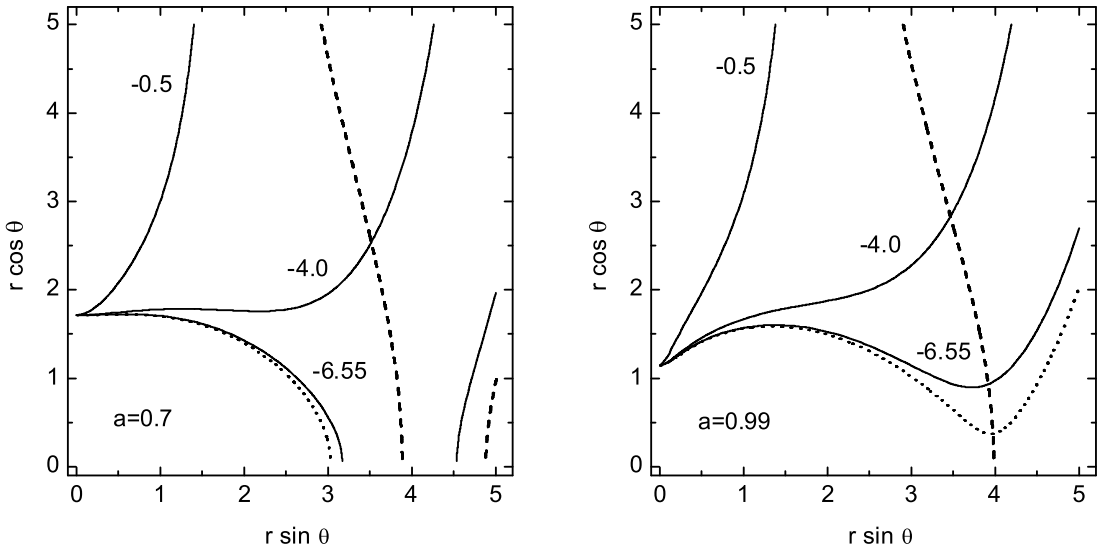


Figure 5.5: Polar plots of r_L (dotted), r_A (solid) and $r_{\rm sp}$ (dashed) for three Type III flows. Each r_A curve is labelled by $\tilde{L}$ and $\Omega_F = -0.144$. The horizon is located at $r_H(0.7) = 1.714$ and $r_H(0.99) = 1.141$. The situation is similar to Type I flows except that the inner light cylinder is pushed farther out and may not exist near the equator.

important trends. They verify that the black hole spin has a negligible effect on the flows far from the hole, regardless of polar angle. Also, with respect to polar angle, there is a much greater sensitivity on spin in the equatorial plane. Generally, a valid flow can be found in the polar regions, with the exception being Type IIc flows for which there may not be an Alfvén point for all initial parameters. However, the location of the Alfvén point and hence the location of strong shocks is strongly dependent on the flow type.

Remarkably, for intermediate angles it is possible to have one initial configuration that

produces either no Alfvén radius or two Alfvén radii, the difference being only a very small angular separation (see, for example, the $\tilde{L} = 3.1$ case for Type I flows in Figure 5.1). For counter-rotating flows another effect occurs: the equatorial solutions vanish because an Alfvén point can not exist. Remember that in Chapter 4 we did find an equatorial shock solution for a Type VI counter-rotating accretion flow—large negative spin and positive Ω_F. We can now see that this was possible only by choosing an extremely small Ω_F. Then the effects of counter-rotation were minimal, the inner light cylinder was close to the horizon and an Alfvén point existed.

Shocks Near The Polar Axis

Now that a preliminary analysis has indicated the possibility of shocks in the polar regions, it is time to present a few shock solutions for polar flows. It was not surprising to find shocks. In the Schwarzschild case the geometry, as well as the magnetic field, is spherically symmetric. So selecting an acceptable angular momentum virtually guaranteed a shock. One detail that needed to be addressed was determining the limits to Ω_F. The maximum/minimum values are still determined by setting $r_L^{\rm in} = r_L^{\rm out}$ but equation (3.10) no longer applies. The result is that much larger Ω_F are possible if the accretion flow originates from small angles. For example, Figure 5.6 shows how the maximum value of Ω_F varies with polar angle for the specific case $a = 0.7$.

As an example of the effect of polar angle, Figure 5.7 displays various parameters for two shock solutions that have the same Ω_F and $\tilde{L}$. For these values, the near equatorial flow was Type IIc while the polar flow was Type I. The results are typical for these types

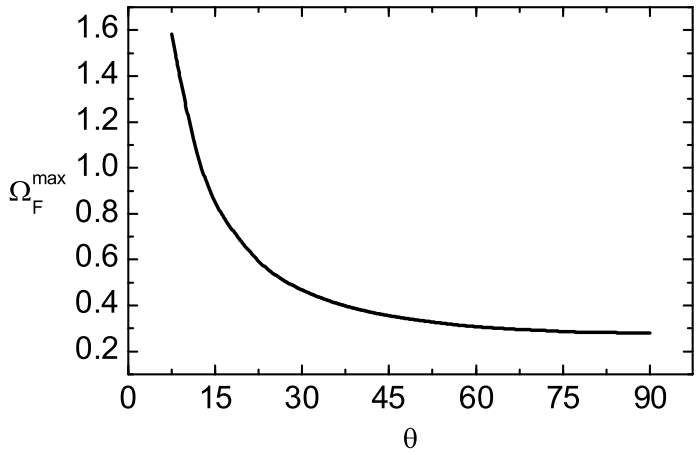


Figure 5.6: The maximum value for Ω_F as a function of polar angle for the case $a = 0.7$. For reference, $\Omega_F^{\max}(\theta = \pi/2) = 0.28116$.

of flows (compare with shocks #6 and #7 of Table 4.6). Once again, shocks are a local phenomenon–the shock behavior does not depend on location, but the type of accretion flows is dependent on location. We have seen that strong slow shocks occur readily for counter-rotating flows. One example of such a shock is given in Figure 5.8. The conserved quantities are similar to those in Figure 5.5 where we saw that Type III flows can have an Alfvén radius close to the horizon and a separation point far away. In this specific example the important radial distances are: $r_L = 1.732$, $r_A = 1.76$, $r_I = 9.15$ and $r_{\rm sp} = 13.9$. So the preshock flow can acquire a large radial velocity and the shock can occur near the light cylinder, two indicators for strong shocks.

Angular Momentum Distribution

So far we have not paid particular attention to the angular momentum chosen for accreting flows. Any angular momentum value giving a valid flow has been accepted.

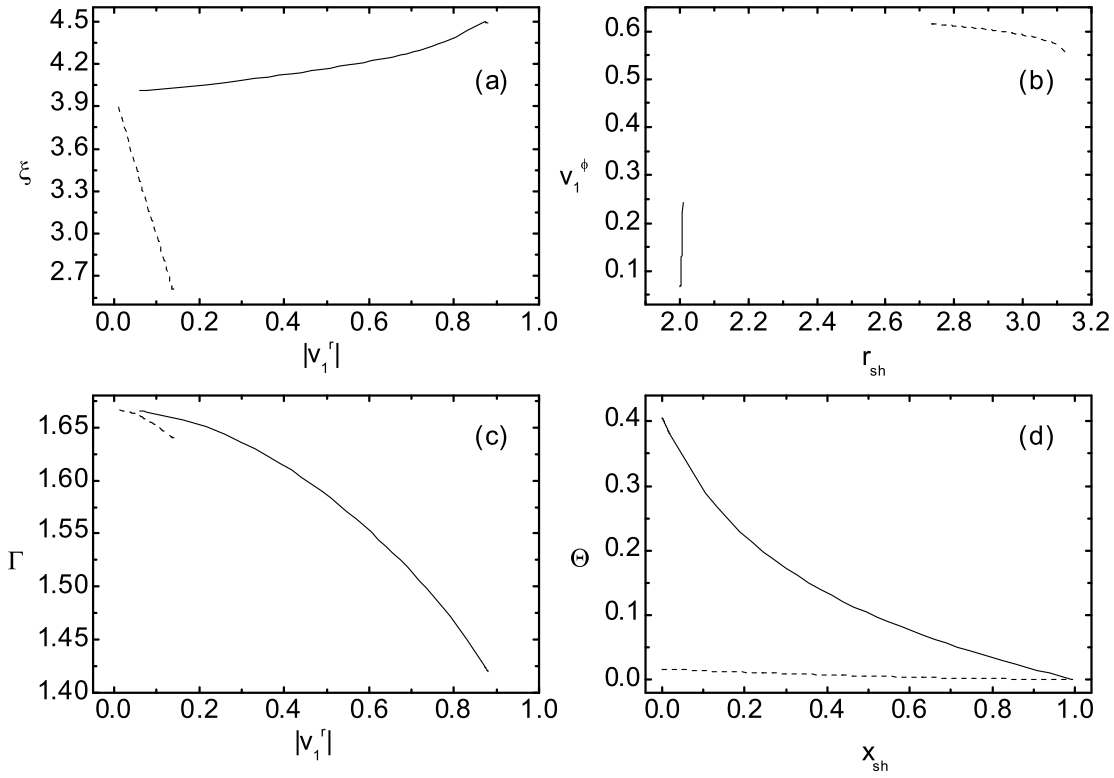


Figure 5.7: Comparison of shock behavior for two accreting flows with the same $\Omega_F = 0.15$ and $\tilde{L} = 0.15$ but different polar angles. Initial parameters are (1) Solid: $\theta = 3.24°$, $E = 0.09$, $L = 0.179$, $a = 0.012$, Type I, (2) Dotted: $\theta = 70.7°$, $E = 0.737$, $L = 1.476$, $a = 0.742$, Type IIc.

For individual shock solutions this is not a problem. But to better understand shocks in the global setting of a black hole we should look at the behavior of quantities over an extended region. One such quantity is the toroidal magnetic field. There are boundary conditions, both at the horizon and at the pole, on the toroidal magnetic field and we can extract information from this. Because the angular momentum is a function of B_ϕ, the θ-dependence on $\tilde{L}$ (or the angular momentum L) becomes important. In this section we will explore the restrictions on the angular momentum, possible angular momentum distributions and the subsequent effect on non-equatorial shocks.

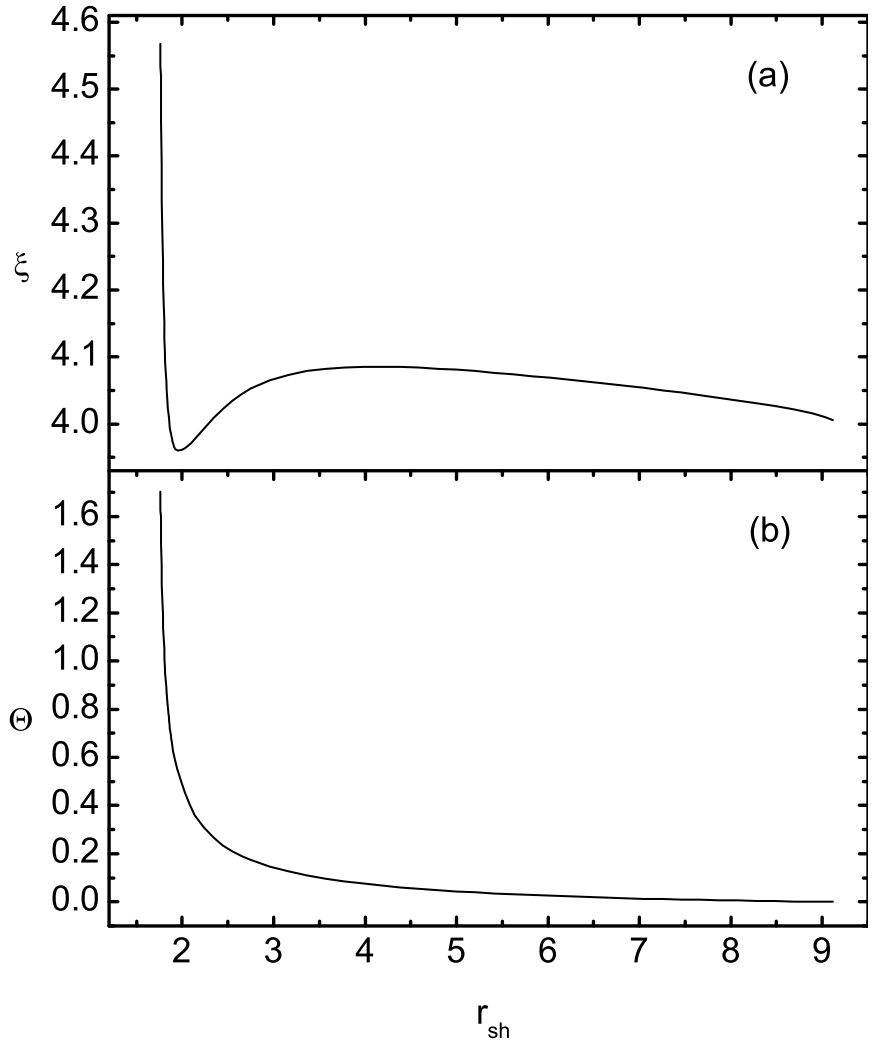


Figure 5.8: Example of strong polar shock, Type III. Parameters are: $\theta = 7.8°$, $a = 0.7$, $E = 1.1$, $L = -1.65$, $\Omega_F = -0.142$.

We begin with the relation for the angular momentum, defined in equation (2.31), $L \equiv -\mu u_\phi - B_\phi/4\pi\eta$. Because L is a function of the toroidal magnetic field, we need to know the boundary conditions on this field. The toroidal component of the magnetic field at the horizon is

$$(B_\phi)_H = \sqrt{\left(\frac{-g_{\phi\phi}}{\Sigma}\right)_H}(\omega_H - \Omega_F)(\partial_\theta A_\phi)_H \ . \tag{5.5}$$

The split-monopole magnetic field has the form $\partial_\theta A_\phi = C \sin\theta$, where $C = constant$. With $g_{\phi\phi} \propto \sin^2\theta$, the toroidal magnetic field component has the θ-dependence $(B_\phi)_H \propto$

$\sin^2\theta$ at the horizon. To be consistent we should require, near the axis at least, that the magnetic field has the form $B_\phi(r,\theta) \sim O(\sin^2\theta)$.

How does this boundary condition relate to the choice of conserved quantities? Because our model uses the split-monopole geometry the assumption of $L(\theta) = constant$ is inconsistent near the axis. This can be remedied. First, we should make sure that the fluid component of L, ($L_f = -\mu u_\phi$) becomes small near the axis. If it does not, a large centrifugal force acts on the plasma and the plasma's inertia could change the magnetic field structure. Second, we can force $L(\theta) \sim \sin^2\theta$. To further restrict the range of parameters, we can also choose $\tilde{L}(\theta) \sim \sin^2\theta$ because we do not expect the energy to have any angular dependence.

There remains the choice of $\tilde{L}_{90} \equiv \tilde{L}(\theta = 90^\circ)$. A large (small) value will give a magnetically (fluid) dominated flow in the equatorial plane. For either choice, because of the $\sin^2\theta$ dependence, the flow must be fluid dominated in the polar regions. Both cases give interesting results, consistent with the conclusions obtained earlier in this chapter. To make the situation a little more interesting, a significant black hole spin, $a = 0.7$, is selected. To make the situation a lot less tedious, a single case, with positive E and positive L, is selected. The accretion flow is then restricted to Type I and Type IIc (see Table 3.1).

A hydro-dominated case is selected by choosing $\tilde{L}_{90} = 2.5$, giving a Type IIc flow for all angles. The angular distribution of critical points and Ω_F for valid flows is shown in Figure 5.9. Near the equatorial plane Ω_F is very narrowly constrained and the radial gap between the injection and Alfvén points, the domain of slow shocks, is quite small. The converse is true in the polar region. There is a distinct demarcation between the two

regions, occurring near 35°. There does not appear to be any unusual physics producing the different regions.

With the given angular momentum distribution the Alfvén radius has only a weak dependence on angle (for zero spin, equation (5.2) shows that the Alfvén radius is independent of angle and roughly of the form $r_A \approx \tilde{L}_{90}/\Omega_F$). For small angles the larger range of Ω_F gives a larger range for r_A. The boundary between the two regions is simply the location where the approximately circular arc of the Alfvén radius and the approximately linear (parallel to the spin axis) line of the separation point, go their separate ways. So even with tight constraints on the free parameters, the shock locations in the polar region are quite variable with the given angular momentum distribution. This will permit some flexibility in positioning a shock when it is used as a source of radiation for hot spots.

Next, we choose $\tilde{L}_{90} = 4.56$ and a sufficiently large Ω_F so that $\Omega_F \tilde{L}_{90} \approx 1$, the magnetically dominated case. Figure 5.10 shows the critical points and poloidal field angular velocity. There is clearly something interesting happening for this situation. For large angles, near the equatorial plane, only small r_A, in the ergosphere, are allowed. These flows are Type I and magnetically dominated. For small angles there is a large range for r_A, all outside the diminished ergosphere. These flows are Type IIc and fluid dominated. The boundary between the two regions is defined by $\Omega_F = \omega_H$ and calculated by setting $r_A = r_{\rm sp}$.

For the values chosen the transition angle can be computed exactly and occurs at $\theta = 43.88°$. The reason for change in flow types is demonstrated in Figure 5.11. At the boundary the acceptable branch of the r_A solution changes discontinuously from the inner branch, with larger Ω_F, (near the equator) to the outer branch, with smaller Ω_F (near

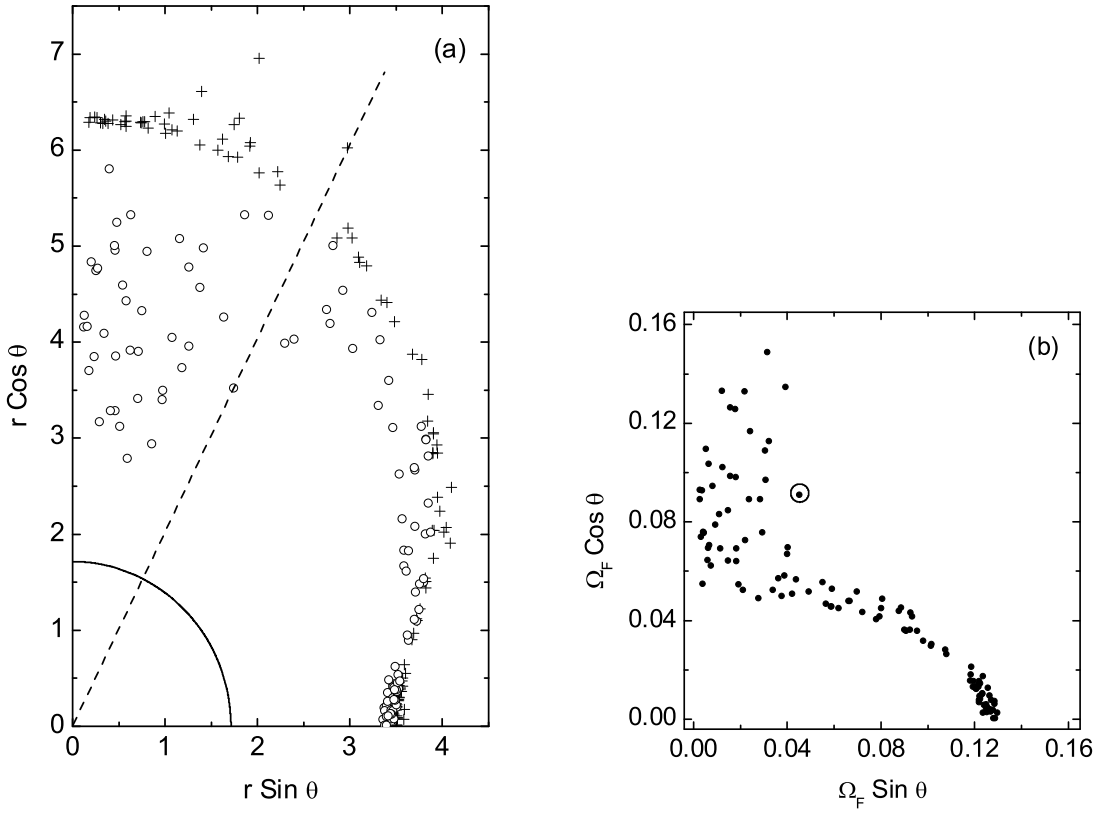


Figure 5.9: (a) A random sample of (r_A, $r_{\rm sp}$) pairs for 116 accretion flows with a preshock angular momentum distribution $\tilde{L} = 2.5\sin^2\theta$ and black hole spin $a = 0.7$. The flow is fluid dominated for all angles. The Alfvén points are labelled by "o" and the separation points by "+". The solid curve is the horizon. The dashed line picks out one (r_A, $r_{\rm sp}$) pair. (b) The corresponding magnetosphere angular velocity. The circled point is the particular Ω_F-value for the pair chosen by the dashed line in (a). The shock location will be tightly constrained in the equatorial region. In the polar region the greater flexibility in choosing Ω_F will allow a greater shock range.

the pole). An interesting aspect of this angular momentum distribution is that the large radial range for slow shock formation occurs next to the transition boundary. Previously we had found that the polar region generally had the greatest range for shocks.

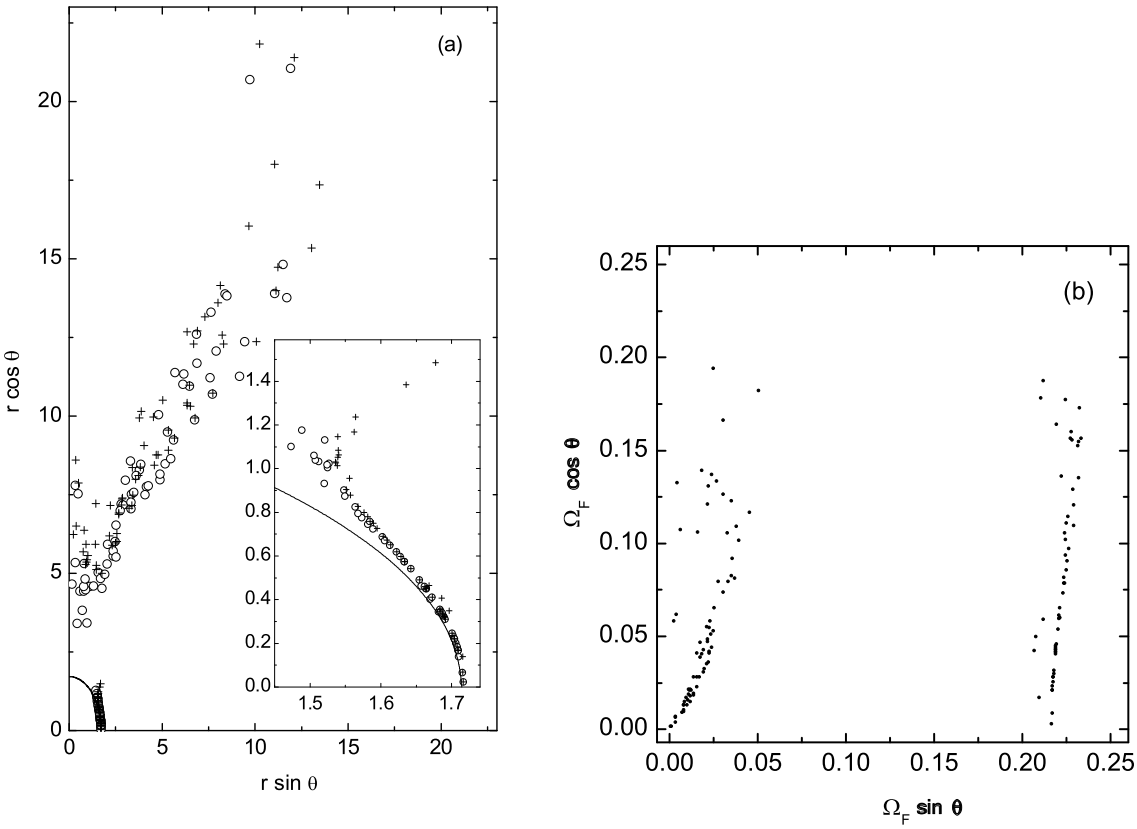


Figure 5.10: (a) A random sample of $(r_A, r_{\rm sp})$ pairs for 128 accretion flows with a preshock angular momentum distribution $\tilde{L} = 4.56 \sin^2\theta$ and black hole spin $a = 0.7$. The flow is magnetically dominated near the equator, fluid dominated near the pole. The Alfvén points are labelled by "o" and the separation points by "+". The solid curve is the horizon. (b) The corresponding magnetosphere angular velocity.

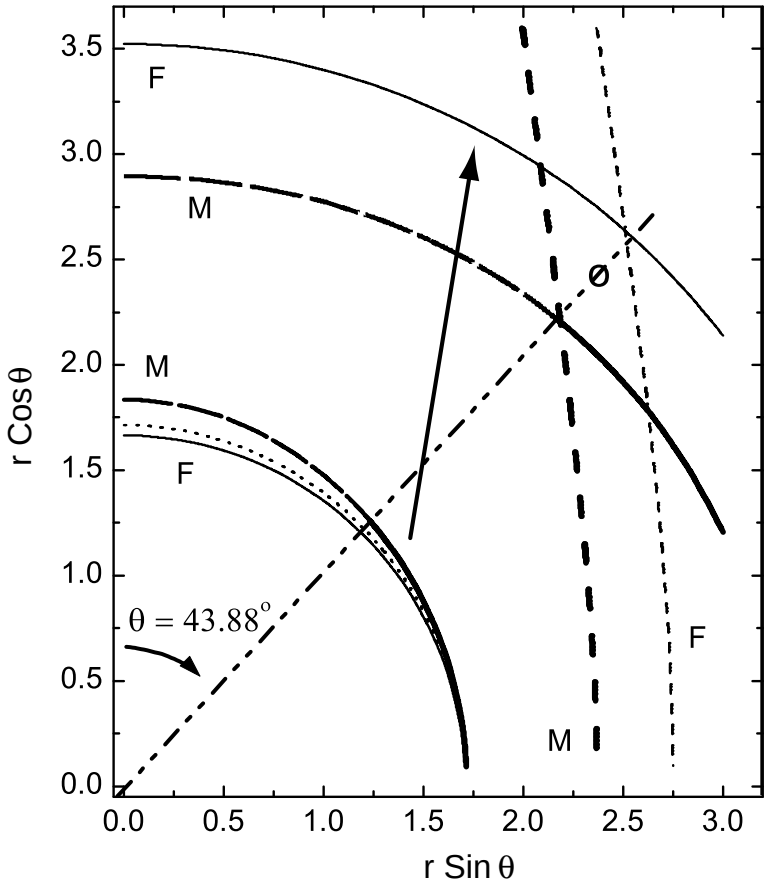


Figure 5.11: Polar plot of r_A (solid), $r_{\rm sp}$ (dash) and r_L (dotted) for both fluid dominated ("F" or thin lines) and magnetically dominated ("M" or thick lines) accretion flows. The preshock angular momentum distribution is $\tilde{L} = 4.56 \sin^2\theta$ and the black hole spin is $a = 0.7$. For large angles (near the equator and $\Omega_F > \omega_H$) the inner Alfvén point is between the light cylinder and the separation point for the "M" flow but not for the "F" flow. Thus, only magnetically dominated flow is allowed there. For small angles (near the axis and $\Omega_F < \omega_H$) the outer branch of the fluid dominated r_A curve becomes the only choice for the inner Alfvén point (the longdash "M" sections do not give valid flow. The transition is denoted by the arrow. The "o" denotes the location (r_A, θ_A) of the transition point.

CHAPTER 6

SWITCH-OFF SHOCKS AND MULTIPLE ALFVÉN POINT FLOWS

'In physics, you don't have to go around making trouble for yourself—nature does it for you.' – Frank Wilczek

Introduction

Two special situations relating to MHD shocks in the vicinity of black holes merit special attention. Under certain circumstances, the spacetime geometry and configuration of the magnetosphere give rise to multiple inner Alfvén points (MIAP's). Significantly different flows can be obtained by adjusting only one of the conserved quantities. Due to the various flow types, the shock behavior can then be significantly altered also. Another special case is the switch-off shock; it occurs when the postshock tangential component of the magnetic field vanishes. It is a limiting case of a slow shock and can be treated with an independent analysis.

Multiple Inner Alfvén Points

Before investigating multiple inner Alfvén point flow solutions and the resultant slow shocks, it is important to understand the difference between an Alfvén point and an Alfvén radius. It was not important to make this distinction previously because the Alfvén point always coincided with the single Alfvén radius. If there are multiple Alfvén radii, this

cannot be the case. The Alfvén radius is a solution of

$$G_\phi + G_t \tilde{L} = 0 \ , \tag{6.1}$$

where $G_t \equiv g_{tt} + g_{t\phi}\Omega_F$ and $G_\phi \equiv g_{t\phi} + g_{\phi\phi}\Omega_F$. It is a function of spacetime geometry, the angular velocity of the magnetosphere, and the fluid's energy and angular momentum. Being independent of the fluid's radial velocity, however, the Alfvén radius is simply a mathematical point with no particular physical significance. Equation (6.1) is complicated enough (fourth degree in radial coordinate r) to allow for two Alfvén radii to occur inside the injection radius for Type I flows.

The Alfvén point, given by $M^2 - \alpha = 0$, does have physical significance. It is the point at which the fluid has attained the Alfvén velocity, i.e., where $M = M_A$. Unless there is some mechanism to slow the fluid (a shock, for example), there can be only one Alfvén point for an accreting fluid. To summarize, once the characteristics of the fluid have been completely specified, the Alfvén point coincides with one, and only one, of the possible Alfvén radii.

This leads to an interesting question. For geometries arranged to have multiple inner Alfvén radii, what changes in the initial conditions of the flow are required for the Alfvén point to "jump" to a different Alfvén radius? From equation (6.1) it is clear that specifying an appropriate pair (Ω_F, $\tilde{L}$) will give multiple Alfvén radii. Then E, L and η are left to specify the Alfvén point, keeping in mind that both E and L can be changed but $\tilde{L}$ must be held constant. In order to simplify the situation as much as possible, we initially keep both E and L fixed. This leaves η as the only remaining free parameter and it alone will

Table 6.1: Initial data and critical points for two MIAP accretion flows. Both flows have $E/\mu_1 = 0.711$, $L/\mu_1 = 0.716$ and $m\Omega_F = 0.207$. The black hole spin is $a/m = 0.503$ and the polar angle is 29.3°.

Flow	$\mu_1\eta$	$r_{\rm H}/m$	$r_{\rm L}/m$	$r_{\rm F}/m$	$r_{\rm A}/m$	$r_{\rm I}/m$	$r_{\rm sp}/m$
Inner	0.195	1.864	1.875	2.196	2.206	3.271	4.489
Outer	0.502	1.864	1.875	2.815	2.852	3.271	4.489

determine the Alfvén point. The two flows will be denoted by ($\eta^{\rm in}$, $r_A^{\rm in}$) and ($\eta^{\rm out}$, $r_A^{\rm out}$) where $r_A^{\rm in} < r_A^{\rm out}$.[1] Slow shock solutions for two such flows were calculated; the data for each flow is given in Table 6.1.

Figure 6.1 shows the solution of the wind equation for the two flows. They are very similar although they each go through their own Alfvén point. The second plot, Figure 6.2 shows the solutions of $N = 0$ and $D = 0$, for each flow, where N and D are the numerator and denominator, respectively, of the poloidal wind equation, (2.41), written in the form

$$(\ln\, u_p)' = \frac{N}{D}\ . \tag{6.2}$$

The prime ($'$) denotes differentiation along the stream line Ψ = constant. For cold flows, N and D are given by (TNTT90)

$$\begin{aligned} N &= \left\{ M^6 + \frac{[2(\alpha k + \epsilon^2)(\ln B_p)' - \alpha k' + 2k\alpha']}{k'} M^4 \right. \\ &\quad \left. + \frac{3\alpha'\epsilon^2}{k'} M^2 - \frac{\alpha\epsilon^2\alpha'}{k'} \right\} \frac{k'}{2} \left(\frac{E}{\mu}\right)^2 \ , \end{aligned} \tag{6.3}$$

$$D = \left[M^6 + 3\frac{\epsilon^2}{k} M^4 - 3\frac{\alpha\epsilon^2}{k} M^2 + \frac{\alpha^2\epsilon^2}{k} + + \left(\frac{4\pi\mu\eta}{B_p}\right)^2 \frac{\alpha\epsilon^2}{k} \right] \frac{u_p^2 k}{1+u_p^2} \left(\frac{E}{\mu}\right)^2 \ , \tag{6.4}$$

and $\epsilon \equiv 1 - \Omega_F \tilde{L}$. These curves meet at the Alfvén point and intersect at the fast

[1] This $r_A^{\rm out}$ is not to be confused with the outer Alfvén point for outgoing flows, which are not discussed here.

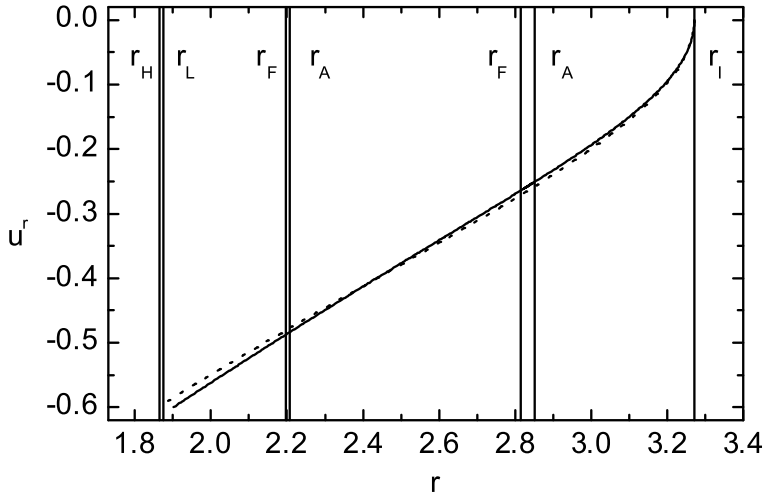


Figure 6.1: Solutions of the wind equation for the two flows listed in Table 6.1. The flows are quite similar, as might be expected from the similarity of the initial conditions. The solid curve goes through the outer Alfvén point and its corresponding fast point; the dotted curve goes through the inner Alfvén point.

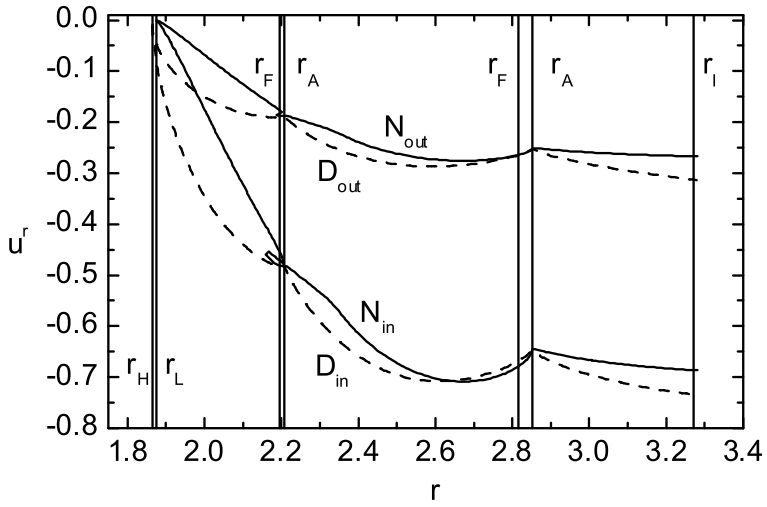


Figure 6.2: Solution of the numerator (N) and denominator (D) of equation (6.2). The intersection of these curves give the Alfvén point and the fast point. The important radial locations are also indicated.

magnetosonic point. Note that these curves show that both flows have the same two Alfvén radii, but each flow has only one fast point (and only one Alfvén point). The close-ups in Figures 6.3 and 6.4 show this more clearly.

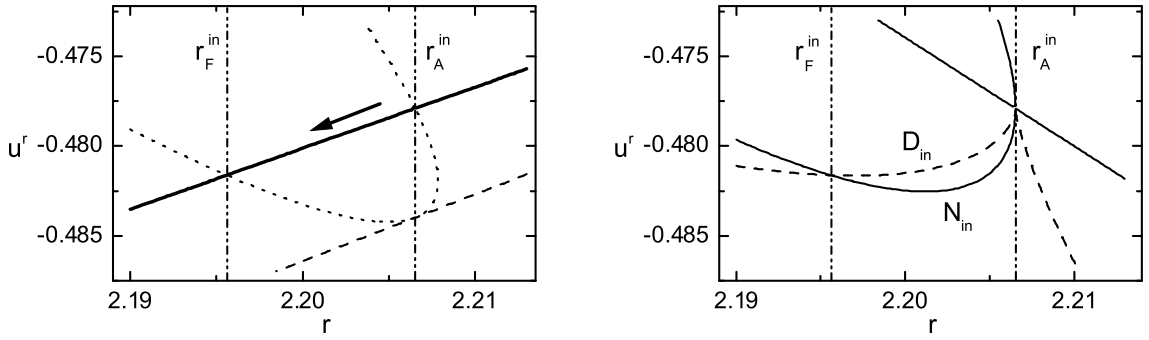


Figure 6.3: A close-up view of Figures 6.1 and 6.2 at the inner Alfvén point. The flow that does not go through ($r_A^{\rm in}$, $r_F^{\rm in}$) is indicated by the dashed line on the left.

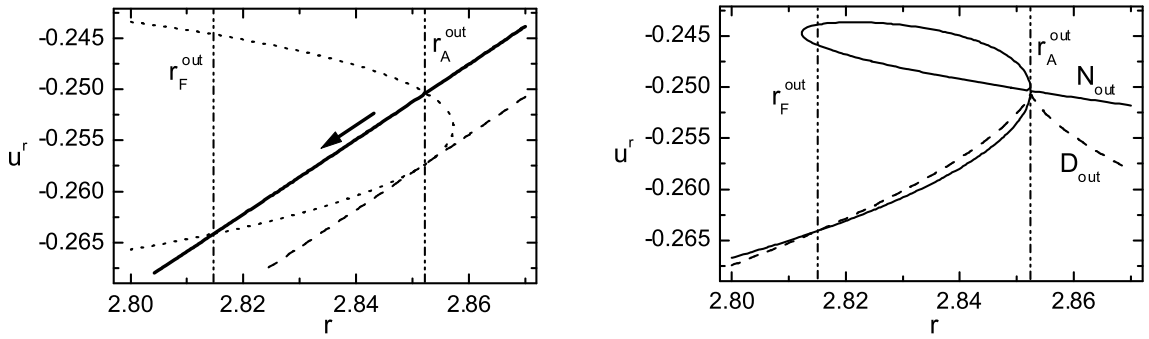


Figure 6.4: A close-up view of Figures 6.1 and 6.2 at the outer Alfvén point. The flow that does not go through ($r_A^{\rm out}$, $r_F^{\rm out}$) is indicated by the dashed line on the left.

Although we are considering only two separate flows, there are three distinct shock regions. For $\eta^{\rm out}$ the shock region extends from r_I to $r_A^{\rm out}$; for $\eta^{\rm in}$ it is from r_I to $r_A^{\rm in}$. However, the latter flow can be subdivided by the outer Alfvén radius. Although this point is not a critical point for the flow, it has a physical significance. Note that ζ changes from greater than to less than one, indicating a change in shock category. As we move

inward from r_I to $r_A^{\rm in}$ the flow goes through the categories Imi3 $\rightarrow$ Imi2 $\rightarrow$ Imi1 (see Table 3.1). Several quantities change sign across $r_A^{\rm out}$, including the magnetization and the toroidal component of the magnetic field. Thus, at $r_A^{\rm out}$ we have $B_{\phi 1} = 0$. So this is an example of a shock solution, discussed in Chapter 3, in which the magnetic field plays no role. The shock is equivalent to a hydrodynamic shock at this one point.

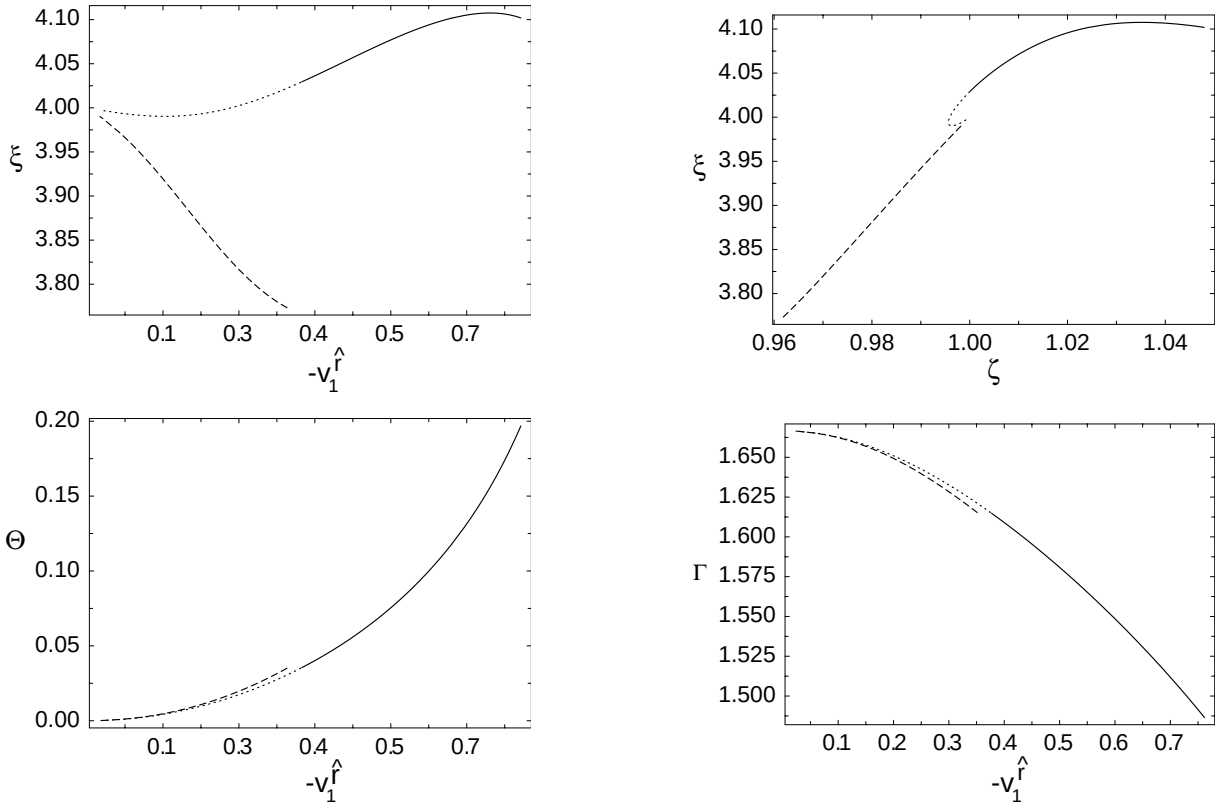


Figure 6.5: Shock solutions for the two flows given in Table 6.1. They differ only in the value of η. The solid and dotted curves correspond to 'Inner' flow and their intersection occurs at the outer Alfvén radius. The 'Outer' flow (dashed) has the outer Alfvén radius as its Alfvén point. Because of this, the 'Outer' flow produces weaker shocks and lower postshock temperatures.

The results for slow shocks occurring for each flow are shown in Figure 6.5. As expected, the shock quantities vary smoothly across $r_A^{\rm out}$. Flows going through $r_A^{\rm in}$ attain a large radial velocity and from experience we expect these flows to have a larger com-

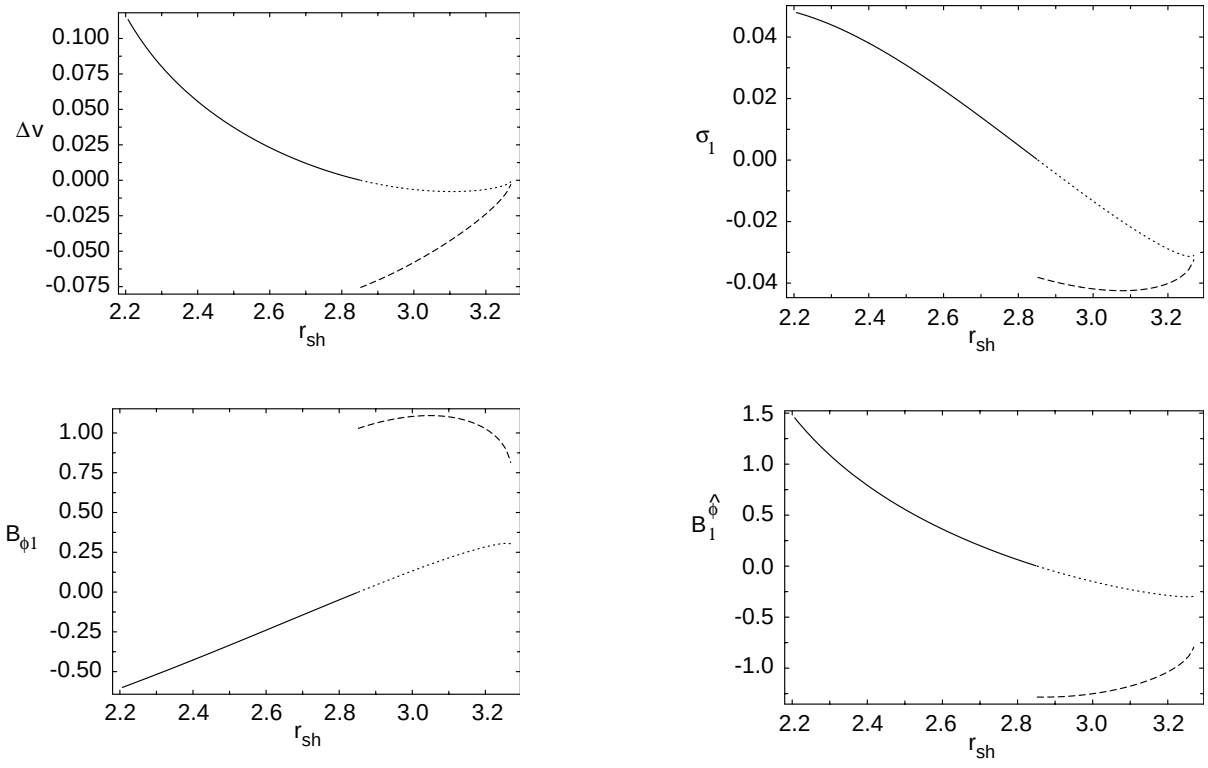


Figure 6.6: Additional results for shock data for the two flows. The difference $\Delta v \equiv v_2^{\hat{\phi}} - v_1^{\hat{\phi}}$ gives the change in the plasma's toroidal velocity across the shock, as seen by the ZAMO.

pression ratio and larger temperature. From the figures we see that this is the case. We discussed the interaction of the flow with the field and its affect on shock behavior in Chapter 4. For this more complicated case the behavior is still consistent.

Figure 6.6 displays additional quantities for the same set of shocks. The sign of $v_2^{\hat{\phi}} - v_1^{\hat{\phi}}$ is less than zero if the shock takes place outside $r_A^{\rm out}$, greater than zero inside. The same holds true for the preshock magnetization. This means that the fluid is accelerated across the shock by the field inside $r_A^{\rm out}$, but decelerated outside. Furthermore, the greater $B_{\phi 1}$, the more negative $B_1^{\hat{\phi}}$, the more negative σ_1, and the greater the deceleration.

One more item about these flows should be mentioned. Why is $\eta^{\rm out} > \eta^{\rm in}$? The initial conditions force the relation $\alpha(r_A^{\rm in}) < \alpha(r_A^{\rm out})$ which in turn implies that $M_1(r_A^{\rm in})^2 <$

Table 6.2: Parameter set for Type I MIAP shocks. All flows have $m\Omega_F = 0.2066$, $\tilde{L} = 1.006$, and $\theta = 30.74°$. Black hole spin is $a/m = 0.5034$.

Shock	Type	E/μ_1	L/μ_1	$\mu_1\eta$	r_A/m	r_1/m
1	Imo	0.7699	0.7751	0.3639	2.8524	4.4198
2	Imi3	0.7581	0.7632	0.1769	2.2065	3.8983
3	Imi1	0.7581	0.7632	0.1769	2.2065	3.8983
4	Imo	0.6568	0.6613	1.3065	2.8524	2.9012
5	Imi3	0.6624	0.6669	0.2195	2.2065	2.9321
6	Imi1	0.6624	0.6669	0.2195	2.2065	2.9321

$M_1(r_A^{\rm out})^2$. This reduces to

$$\frac{\eta_{\rm in}}{\eta_{\rm out}} = \left(\frac{u^r_{\rm out}}{u^r_{\rm in}}\right)\left(\frac{G^{\rm in}_t}{G^{\rm out}_t}\right)\left(\frac{B^r_{\rm in}}{B^r_{\rm out}}\right) \ . \tag{6.5}$$

Each term on the right hand side of equation (6.5) is less than one, showing that $\eta_{\rm in} < \eta_{\rm out}$. Another way to view this is from the definition of η, equation (2.32). Evaluating both flows at $r_A^{\rm out}$ we obtain

$$\frac{\eta_{\rm out}}{\eta_{\rm in}} = \frac{n_{\rm out}|u^r_{\rm out}|}{n_{\rm in}|u^r_{\rm in}|} > 1 \ . \tag{6.6}$$

This means that the flow with the greater mass flux reaches the Alfvén speed first.

So far we have looked at MIAP flows with a fixed energy and angular momentum. Now we ask what happens if we generalize the flows, keeping $\tilde{L}$ fixed as before but allowing E and L to change. The parameters for two pairs of Type I MIAP shocks are listed in Table 6.2. A comparison of the compression ratio and temperature for these shocks is presented in Figures 6.7 and 6.8, respectively. There are a number of interesting features for increasing E (and L): (1) First, the injection point moves outward (compare shock #1 with #4). This makes sense because $r_{\rm inj}$ is the solution of $E - \Omega_F L = \alpha^{1/2}$, the quantity $E - \Omega_F L$ increases with increasing energy (for $\tilde{L}$ constant), and α is an increasing function

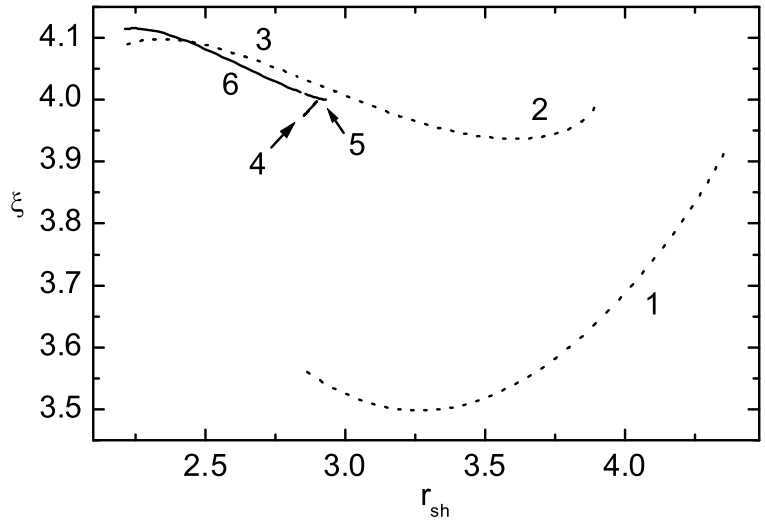


Figure 6.7: The compression ratios of two MIAP slow shocks with parameters given in Table 6.2. The separation between shocks #2 and #3 occurs at $r_A^{\rm out} = 2.8524$.

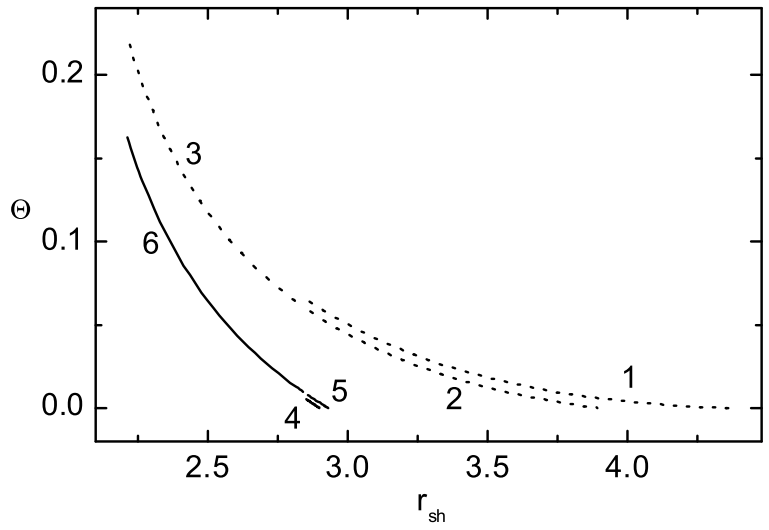


Figure 6.8: The postshock temperatures of two MIAP slow shocks with parameters given in Table 6.2.

of r. (2) The minimum compression ratio decreases significantly for the Imo flow. These flows are similar, in defining characteristics, to Type IIc flows, which we saw in Chapter 4 tend to produce weak shocks. The relatively large toroidal velocity means an oblique shock—the flow receives a "glancing blow" rather than a direct hit. Shock #1 has a larger angular momentum, L, and thus larger $v^{\hat{\phi}}$ than shock #4, resulting in a smaller compression ratio. (3) The larger energy flows have a smaller η. The defining equation for the Mach number, (2.33), the Alfvén point condition, equation (2.38), and the fact that the radial velocity is larger for the bigger energy flows, taken together imply that η must be smaller for these flows. (4) The maximum velocities, both radial and toroidal, increase for larger E and L. This is not surprising, of course. Also, the larger toroidal velocity gives a larger toroidal magnetic field component. (5) The postshock temperature is still highly correlated with radial velocity but the small change in parameters alters the location for a given temperature considerably.

Under most circumstances, a change in one or more of the conserved quantities does not significantly alter the shock parameters, if the change still permits a shock. In the case of MIAPs it is remarkable that a change in just one of the conserved quantities can produce fundamentally different solutions. With a change in the direction of the Poynting flux comes a large change in the compression ratio, temperature, adiabatic index and shock location. Reducing η extends the shock range, allows for larger radial velocities and reversed Poynting flux.

Switch-Off Shocks

The examples of slow shocks presented in Chapter 4 approached the switch-off shock solution as the shock location neared the Alfvén point (see, for example, Figure 4.13, where the postshock toroidal magnetic field becomes very small for a shock near the Alfvén point). The existence of such shocks has been debated. Lichnerowicz (1967) claimed that limit shocks, a class in which switch-off shocks belong, cannot exist in relativistic MHD. This would make relativistic MHD systems qualitatively different from Newtonian MHD. However, Komissarov (2003) found numerical solutions of such shocks and claims to have found an error made by Lichnerowicz. Also, Punsly & Coroniti (1990b) concluded that a switch-off shock is required in their model. We will continue under the assumption that switch-off shocks do exist.

In this section we first define the switch-off shock and then present an analysis of this special case. We then compare shock solutions occurring near the Alfvén point, computed according to the equations of Chapter 2, to the properties of switch-off shocks having the same set of conserved quantities. This is a significant and useful check for our numerical procedures. As we have seen, shock quantities often change dramatically as r_{sh} approaches r_A. Numerical quantities can approach the form 0/0, so it is important to have an independent analysis. With this technique we show that these rapidly changing quantities, such as the compression ratio, approach known finite values.

A switch-off shock is a limiting case of a slow shock in which the magnetic field is "switched-off" by the shock. In our model this means that the toroidal component of the postshock flow is zero, $B_{2\phi} = 0$. As the name implies, for a switch-off shock we

require $B_{1\phi} \neq 0$. So a switch-off shock does not occur at the outer Alfvén radius, where $B_{\phi 1} = B_{\phi 2} = 0$. Takahashi (2002b) has derived the necessary equations that apply at the Alfvén point. We begin with equation (2.107), repeated here for convenience:

$$1 - \frac{u_2^t}{u_1^t} = \sigma_1(q-1) - \frac{\Gamma}{\Gamma - 1}\frac{g_{rr}(u^r/u^t)_1^2(u_2^t)^2}{\xi}\Pi \ . \tag{6.7}$$

For a switch-off shock, the ratio of the time component of the four-velocities and the pressure in the above equation can be rewritten as

$$\left(\frac{u_2^t}{u_1^t}\right)_A = \frac{\xi_A S}{\sqrt{\xi_A^2 J + H}}, \tag{6.8}$$

$$\Pi_A = I - \frac{(M_2^2)_A}{\alpha_A} = I - \frac{\zeta_A}{\xi_A}. \tag{6.9}$$

with

$$S \equiv (1+\sigma_1)_A = \frac{(h\rho_\omega)_A}{G_{\phi A} E f_{1A} + (h\rho_\omega)_A} \ , \tag{6.10}$$

$$J \equiv \frac{E^2(-k)_A}{h_A^2}(u_1^t)_A^2 S^2 = \left(\frac{E}{\mu_c}\right)^2 (-k)_A = (1+u_p^2)_A + \left(\frac{E}{\mu_c}\right)^2 \alpha_A f_{1A}^2 \ , \tag{6.11}$$

$$H \equiv (u^r u_r)_{1A} S^2 \ , \tag{6.12}$$

$$I \equiv 1 - \frac{1}{2}\left(\frac{E}{\mu_c}\right)^2 \left[\frac{(1-\Omega_F\rho_\omega f_1)^2\rho_\omega^2}{(u^r u_r)_1 g_{\phi\phi}}\frac{(\Omega_1 - \Omega_F)}{(\Omega_F - \omega)}\right]_A \ , \tag{6.13}$$

$$= 1 - \frac{1}{2}\left(\frac{E}{\mu_c}\right)^2 \left[\frac{(X_{fluid})_1^2\rho_\omega^2\sigma_1\alpha}{(u^r u_r)_{1A} S^2}\right]_A \ , \tag{6.14}$$

$$\zeta_A \equiv \left[1 + G_\phi G_t \frac{f_1}{\rho_\omega}\right]_A^{-1} \ , \tag{6.15}$$

$$X_{fluid} \equiv 1 - X_{em} \ , \tag{6.16}$$

$$X_{em} \equiv -\frac{\Omega_F B_\phi}{4\pi\eta E} = \rho_\omega \Omega_F f \ , \tag{6.17}$$

where we use the relation $(u_1^t)_A = (h_a/\mu_c)(1/S)$ and

$$f \equiv -\frac{G_\phi + G_t(L/E)}{\rho_\omega(M^2 - \alpha)} \ . \tag{6.18}$$

Then, for the switch-off shock, equation (3.4) can be rewritten as

$$\xi_A^2(\xi_A^2 J + H) = \left[\xi_A^2 J + H + \frac{\Gamma}{\Gamma - 1}\frac{H}{S}(\xi_A I - \zeta_A)\right]^2 \ . \tag{6.19}$$

Thus we obtain a polynomial of "fourth" degree in ξ_A. The polytropic index Γ is a postshock quantity but for convenience can be set to some constant value. The final unknown quantity is the poloidal velocity $u^r u_r (= -u_p^2)$ which can be reduced to

$$u^r u_r = g_{rr}(u^r)^2 = g_{rr}\left(\frac{M^2 B^r}{4\pi\mu\eta G_t}\right)^2 \ . \tag{6.20}$$

For the preshock flow, at the Alfvén point, we obtain

$$(u^r u_r)_{1A} = \frac{\alpha_A^2 (B^r B_r)_A}{(4\pi\mu_c\eta)^2 G_{tA}^2} \ . \tag{6.21}$$

When we give a parameter set (E, L, Ω_F, η) under a given magnetic field configuration, where $u^\theta = B^\theta = 0$ are assumed, we obtain a compression ratio ξ_A at the switch-off location.

There are two immediate applications for these results. First, we can investigate the conditions under which a switch-off shock can occur. To see the parameter dependence for each of the parameters on ξ_A we can plot X vs. ξ_A diagrams, where X is one of (E, L, Ω_F, η). If there is a maximum (or minimum) value of each parameter X for the switch-off shock it will be caused by some restrictions on the shock condition. Here we should note that the numerical calculation of f_{1A} may cause a numerical error or give an incorrect value because $f_{1A} = 0/0$ at r_A. So, for example, we only give E, L and Ω_F along with a function $F_B \equiv B^r/B_0$. Then f_{1A}, which is related to the toroidal magnetic field $(B_\phi)_{1A}$, is a parameter to be set directly. By using the poloidal equation and the definition of the Mach number, we can obtain the remaining conserved quantity η

$$\tilde{\eta} \equiv -\frac{4\pi\mu\eta}{B_0} = \frac{M^2 F_B}{u^r G_t} \ , \tag{6.22}$$

where

$$(u^r u_r)_{1A} = 1 + \left(\frac{E}{\mu_c}\right)^2 (\alpha_A f_{1A}^2 + k_A) \ . \tag{6.23}$$

Figure 6.9 shows the dependence of ξ on the other conserved quantities for a particular shock solution. For example, the E vs. ξ curve gives the switch-off shock compression ratio for variable energy but fixed Ω_F, L, and η. It is not yet clear how useful this approach can be. For example, the figure indicates a maximum L in order to have a switch-off shock, but this is for fixed E and Ω_F. Changing these values slightly may produce a much different picture. Nevertheless, a consistency check can be made. For a known shock occurring close to the Alfvén point, Figure 6.9 shows the conserved quantities and

compression ratio. In every case, the data point lies close to the switch-off shock solution.

A second application is to use these results as an independent check of shock solutions based on the derivations presented in Chapter 2. We can take a shock with given (E, L, Ω_F, η) and use the computed $\Gamma(r_{sh} \approx r_A)$ as a reasonable approximation. Substituting these values into equation (3.4) gives ξ_A. In addition, the limit equations presented in Appendix C can be used to calculate the quantities (q, ζ, σ_1, Π, Θ, u^r), all evaluated at r_A. These results can be compared with the those obtained from the general situation. Any major discrepancies will indicate a problem.

Let us apply this technique to a shock solution from Chapter 4 (see Table 4.3), specifically the Type I, spin $a = 0.95$ case. Table 6.3 lists several quantities, evaluated using both methods. The values of q and $B_{\phi 1}$ show how close the shock was to being a switch-off shock. The general agreement and consistency confirm our previous results.

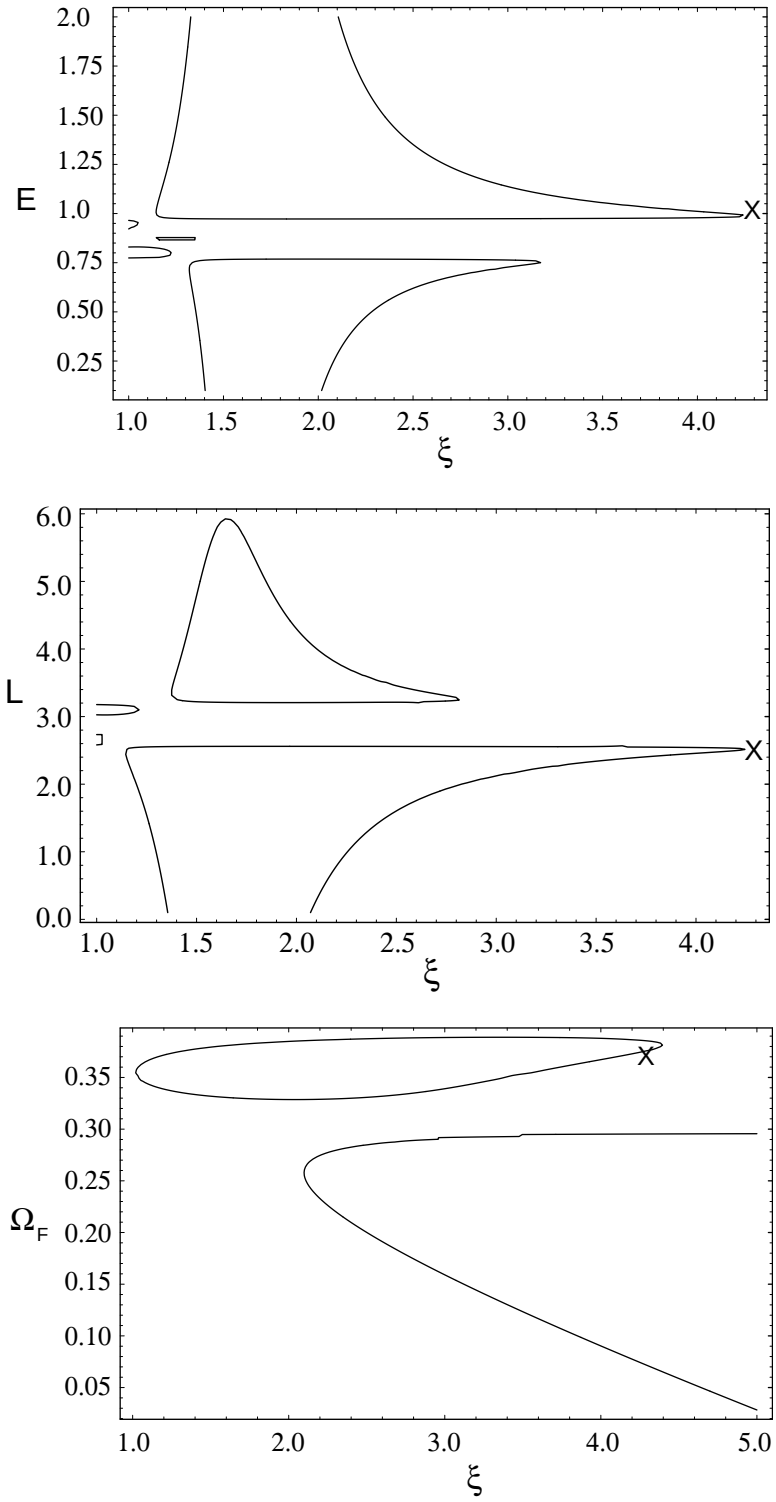


Figure 6.9: Parameter space for switch-off shocks. The solid line in each plot indicates the switch-off shock value for that parameter, given that the other conserved quantities are held fixed. For comparison the "X" indicates the actual conserved quantities for a slow shock occurring very close to the Alfvén point and thus, almost a switch-off shock.

Table 6.3: Comparison of the switch-off shock solution to the general solutions for the Type I, $a = 0.95$ shock discussed in Chapter 4, (see Table 4.3). In the first row, the "r" indicates the shock location in the left column and the Alfvén point in the right column. The apparent precision of the values does not represent the number of significant digits, it is only to indicate the level of disagreement between the two methods. (Assuming, of course, that there is sufficient precision to make the comparison.)

Variable	General	Switch-Off
r	1.335358	1.335345
Γ	1.461097	1.4610
ξ	4.28	4.07
ζ	1.12656	1.12675
M_{1A}	0.050748	0.050748
u_1^r	-0.13904	-0.13904
Π	0.768	0.723
Θ	0.2565	0.2551
σ_1	0.12665	0.12675
$B_{1\phi}$	-0.00036	NA
q	0.00077	NA

CHAPTER 7

FAST MAGNETOSONIC SHOCKS

'The race doesn't always go to the swiftest.' – Unknown

Introduction

Except for a brief analysis of fast shock categories in Chapter 3, this work has been restricted to the study of slow magnetosonic shocks. But the theory of MHD shocks developed in Chapter 2 applies to both slow and fast shocks. Once the machinery for solving the jump conditions for slow shocks has been developed it can then be adapted to fast shocks without too much difficulty. For the fast shock to occur the accreting plasma must pass through the magnetosonic fast point. Inside that point there is an opportunity for a fast shock. In our model this kind of shock does occur and in this chapter we will present a few fast shock solutions, look at some of their properties, and discuss the implications.

Research on non-relativistic fast shocks has been extensive. Because of their importance in our neighborhood, fast shocks occurring in the earth's magnetosphere (and/or vicinity of the sun) have been investigated both theoretically and observationally. But very little research has been done on relativistic fast shocks and there have been few applications in astrophysics. These applications consist mainly of jets from AGN and supernovae. But there have been no detailed studies of fast magnetosonic shocks taking place in a curved spacetime. Punsly briefly discussed the relative importance of fast and

slow shocks for accreting flows in the ergosphere (Punsly, 2001). In his model, plasma streams toward the equatorial plane where the toroidal component of the magnetic field is zero. Thus, slow shocks, specifically switch-off shocks, were much more important. On the other hand, slow mode shocks are considered to be ineffective particle accelerators (see discussion in Chapter 8); thus, an investigation into fast mode shocks is warranted.

Fast Shock Results

In our model, the significant *extrinsic* difference between fast and slow magnetosonic shocks is their location. Given the same, or similar set of initial conditions, a fast shock must take place closer to the black hole ($r_F < r_A$). With widely different initial conditions, of course, there is no correlation between their locations. For example, a fast shock can occur outside the ergosphere but a Type IIb shock can take place within the ergosphere. But it is extremely unlikely for a fast shock in an accreting plasma to exist at a large distance from the hole. More about this later.

Before presenting shock solutions, we should consider two aspects of fast shocks in our model that may be in competition. We have found that, generally, the larger the radial velocity of the flow, the greater the strength of the shock, as measured by the compression ratio or postshock temperature. Although this tendency was found for slow shocks we expect it to hold for fast shocks as well. Because the fast shock location is expected to be very close to the horizon, it seems reasonable to expect large preshock radial velocities. The competing characteristic is that for fast shocks, the toroidal component of the magnetic field must increase across the shock. Therefore, a fast shock converts

some of the flow's kinetic energy to magnetic energy so heating of the postshock plasma is expected to be correspondingly smaller.

The actual situation, as usual, turns out to be very complicated. The radial velocities are not necessarily large. The compression ratios are relatively insensitive to the velocity, being small regardless of the velocity. Amplification (q) of the magnetic field is typically not large but, contrary to what might be expected, the greatest heating of the plasma is at a maximum q.

Now we present fast shock results. Fast shock solutions for all categories, (see Table 3.5, page 62) were obtained. Figures 7.1–7.5 show a few shock curves for the three main types of flows. Also included is a solution for the special Type II {a1,a2,a3} subcategories that involve a negative preshock magnetization. All solutions are typical shocks with a wide range of initial parameters but always with a spin $a \geq 0.7$; this insured all flow types were included. All accreting flows were restricted to the equatorial plane, partly for simplicity, partly to enable comparison with previous results.

Because of the widely varying range of initial conditions across the flow types, no attempt will be made to make detailed comparisons; only broad features will be mentioned. We will look at only the qualitative similarities and differences of the various types of fast shocks. For this reason, the values of the conserved quantities and initial conditions will not be given. Due to the varying ranges of shock location a normalized shock location, x_{sh}, is used. This point is scaled by the fast point and the light cylinder: $x_{sh} \equiv (r_F - r_{sh})/(r_F - r_L)$. The light cylinder is used because shocks cannot form within the inner light cylinder, the Alfvén wave speed becomes imaginary.

As expected from the discussion of shock categories in Chapter 3, the compression

ratio remains small for almost every fast shock solution. It is somewhat larger for Type III flows and nearly four for Type IIa3 flows. The shock location is close to or within the ergosphere for all situations, a little farther out for the counter-rotating magnetosphere (Type III). The radial velocities are not large, in general. This is because the separation region, the source of the incoming plasma, is also close to the black hole. So the fluid has not "fallen" far enough to acquire a large speed. The total velocity, as measured by β_1 (the radial three-velocity of the fluid measured by the ZAMO, $\beta \equiv [(v^{\hat{r}})^2 + (v^{\hat{\phi}})^2]^{1/2}$), is quite significant due to large toroidal velocities. The angle between the flow direction and the shock normal is then also large. The small radial velocities and the large angle both tend to produce shocks with small compression ratios. Another indicator of strong shocks, a large preshock magnetization, does not happen. The postshock adiabatic index is generally near 5/3 and the temperature is usually quite small.

The exception to most of these results is the shock that occurs when the flow is Type IIa3. For this flow, radial velocities are large ($r_{\rm I}$ is relatively far from the hole and $r_{\rm L}$ is close to the horizon), the adiabatic index is close to 4/3 and the postshock heating is significant, $\Theta \approx 0.5$. The reason for this can be seen in the magnetic energy component, (Figure 7.4). The preshock energy has only a 2% magnetic component; most of the energy is kinetic. This gives a flow direction and field direction nearly aligned with the shock front, producing a strong shock. An interesting aspect of these shocks is that flows that are Type IIa3 everywhere do not produce strong shocks nor significant heating. This is probably because the initial conditions required to obtain a negative magnetization allowed for high radial velocities and a small magnetic energy component.

A final point is that for slow shocks the special case of a switch-off shock (see Chapter 6)

could and did exist in our model. For fast shocks there is the equivalent special case of the switch-on shock, in which the preshock toroidal magnetic field is zero but the postshock toroidal field is non-zero. This would give $q \to \infty$ but from Figure 7.3, it is evident that such a case does not occur. Under no circumstances did a fast shock ever approach the switch-on case. It may be that our model does not allow the proper initial conditions for this case.

The question of fast shock relevance has, for the most part, been answered. We have presented representative fast shock solutions and shown that they occur at a maximum distance of, say, $r_{\rm sh}^{\rm max} \approx 4$. With an exhaustive search of initial parameters it may be possible to extend this range a little. But it has also been shown that the fast shocks that do not occur near the horizon are weak. Although in this chapter we investigated only fast shocks in the equatorial plane, it seems plausible that the same reasoning will hold in for non-equatorial flows. Once again, we must conclude that it is unlikely for fast shocks to play an important role with respect to hot spots.

Comparison with Previous Results

Before closing the chapter on fast shocks, we would like to discuss the behavior of fast shocks in our model with results from previous research. The derivation (Chapter 2) for adiabatic magnetosonic shocks in a Kerr spacetime is an extension of a derivation by AC88 for relativistic shocks in a flat spacetime. In their article, Appl & Camenzind determined many properties of fast magnetosonic shocks. We would be remiss to leave the subject of fast shocks without comparing their results with ours. As we have mentioned before,

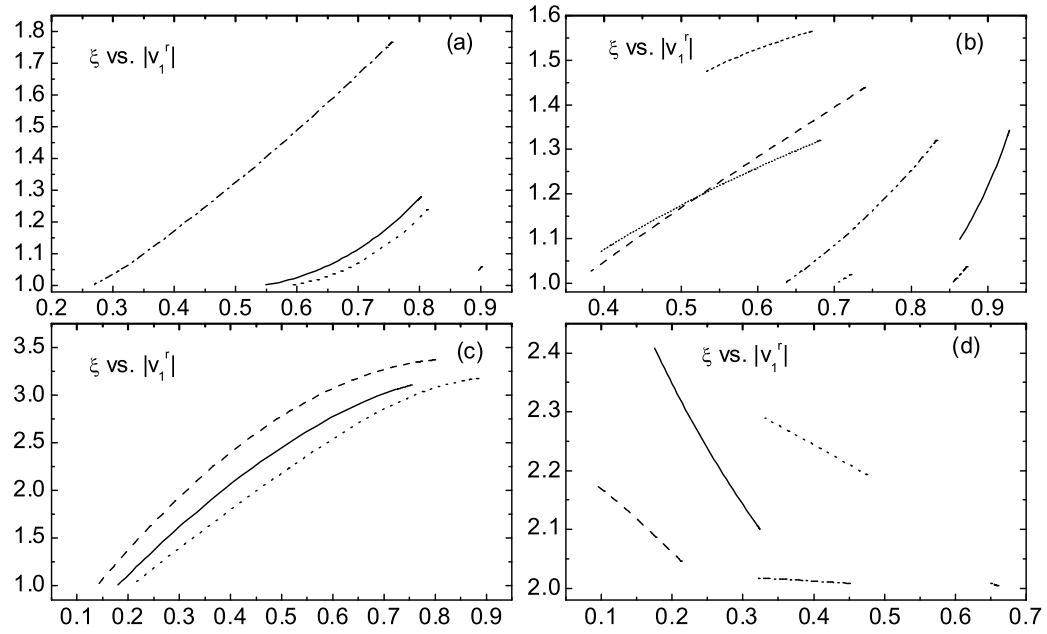


Figure 7.1: Compression ratio vs. radial flow velocity curves for the flow types: (a) Type I, (b) Type II, (c) Type II ($\sigma_1 < 0$), (d) Type III. Note that stippling is used to identify particular shocks for a given flow type; there is no correlation, for example, of the dotted curve in panels (a) and (c). However, the stippling is consistent for all figures in this chapter. For example, the solid curve in panel (d) for Figures 7.1–7.6 correspond to the same shock solution.

our model is much more complicated than their model. The results we have obtained are more difficult to interpret and will, depending on initial conditions (i.e., flow types), both agree and disagree with AC88. Their results are enumerated below, along with our own findings.

1. "the shock becomes weaker with increasing magnetization"

   For a given flow we find just the opposite: an increasing magnetization results in a stronger shock. It is not a large effect in that the magnetization is small and the shock is weak; there is not much change in either quantity. This is not a contradiction of AC88 though. They were able to assign a constant magnetization to a particular

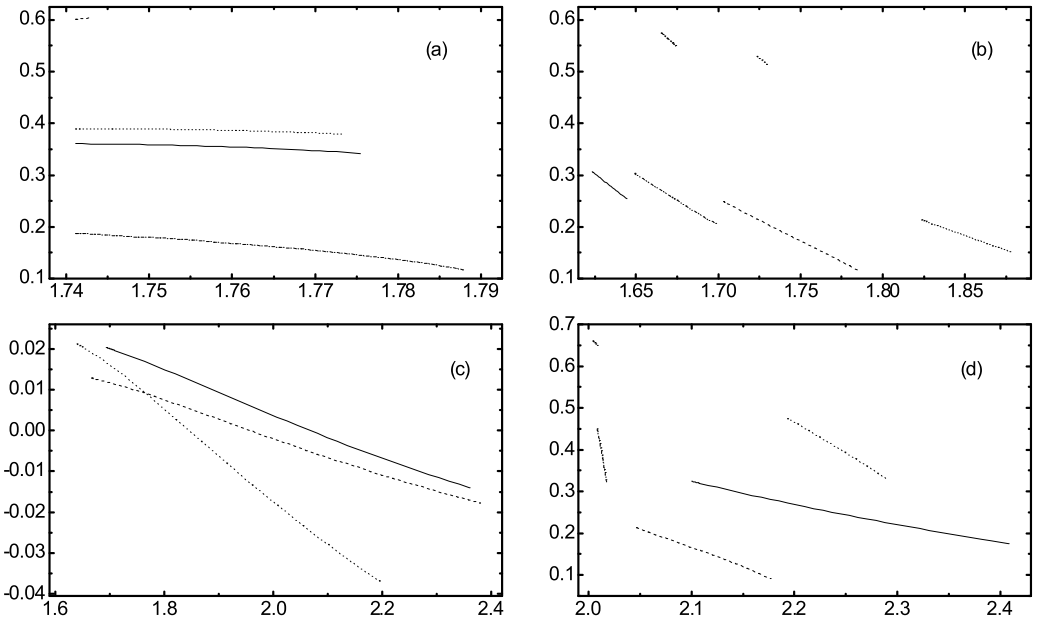


Figure 7.2: Preshock magnetization vs. shock location (σ_1 vs. r_{sh}) curves for the flow types: (a) Type I, (b) Type II, (c) Type II ($\sigma_1 < 0$), (d) Type III.

flow while we cannot. Other effects taking place during accretion make it difficult to isolate the effect of magnetization. However, for a given flow type, a larger magnetization does tend to produce a weaker shock. Furthermore, the strongest shocks occur for flows with a negative initial magnetization and evolving into a very small positive magnetization, a situation AC88 had no need to consider.

2. "Already a moderate magnetic field leads to weak shocks..."

   We find that a moderate magnetic field, measured by the relative magnetic energy in the ZAMO frame (Figure 7.4), does lead to weak shocks. A 2% magnetic component can still give strong shocks but with only a 10% magnetic component, fast shocks are weak.

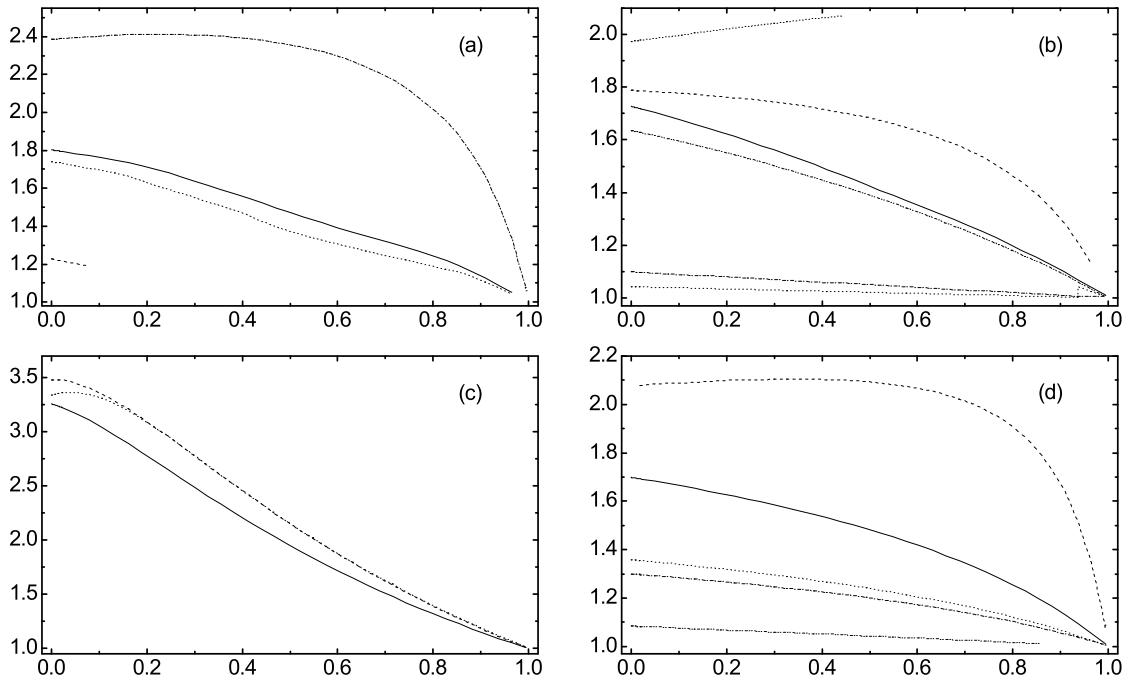


Figure 7.3: Amplification of the toroidal magnetic field (q vs. x_{sh}) across the shock for the flow types: (a) Type I, (b) Type II, (c) Type II ($\sigma_1 < 0$), (d) Type III.

3. "for small angles the toroidal component of the magnetic field in the jet will be strongly amplified in the shock transition."

   A&C are saying that q is large for small angles. The angle they are referring to is the angle between the magnetic field and the propagation direction in the comoving frame. They give their result indirectly and unfortunately, only in an unreadable graph. In our model we cannot keep the same angle constant. However, we observe that q is largest (a factor of three) when the radial velocity is largest and when the magnetic energy is the smallest. This situation gives a small difference between the field and fluid directions. But the amplification of the field is somewhat misleading. The greatest amplification occurs for the strongest shocks but this is because the preshock toroidal component is so small.

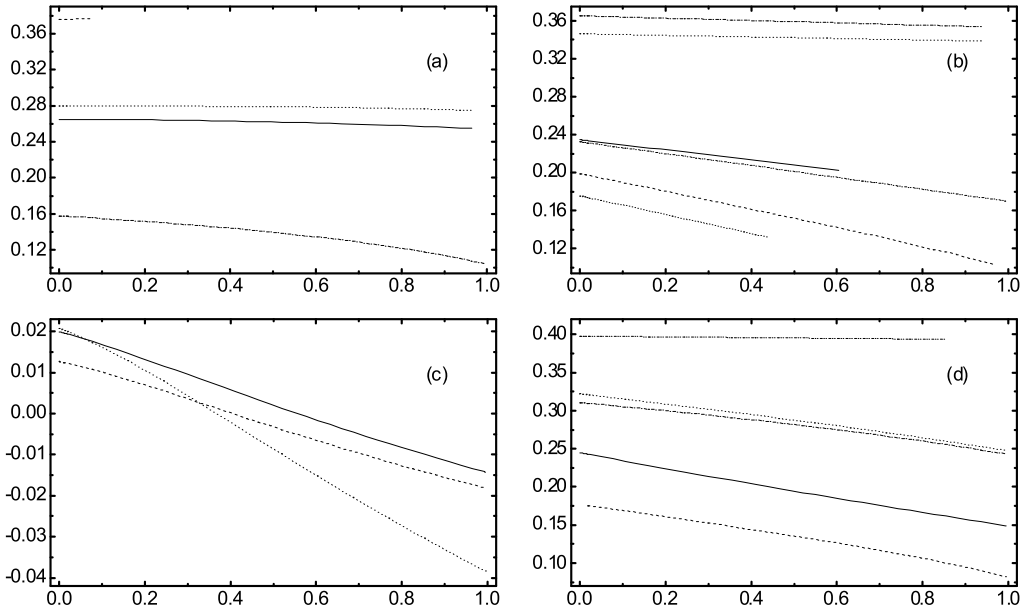


Figure 7.4: Preshock magnetic energy percentage (E^m_{1z}/E_{1z} vs. x_{sh}) for the flow types: (a) Type I, (b) Type II, (c) Type II ($\sigma_1 < 0$), (d) Type III.

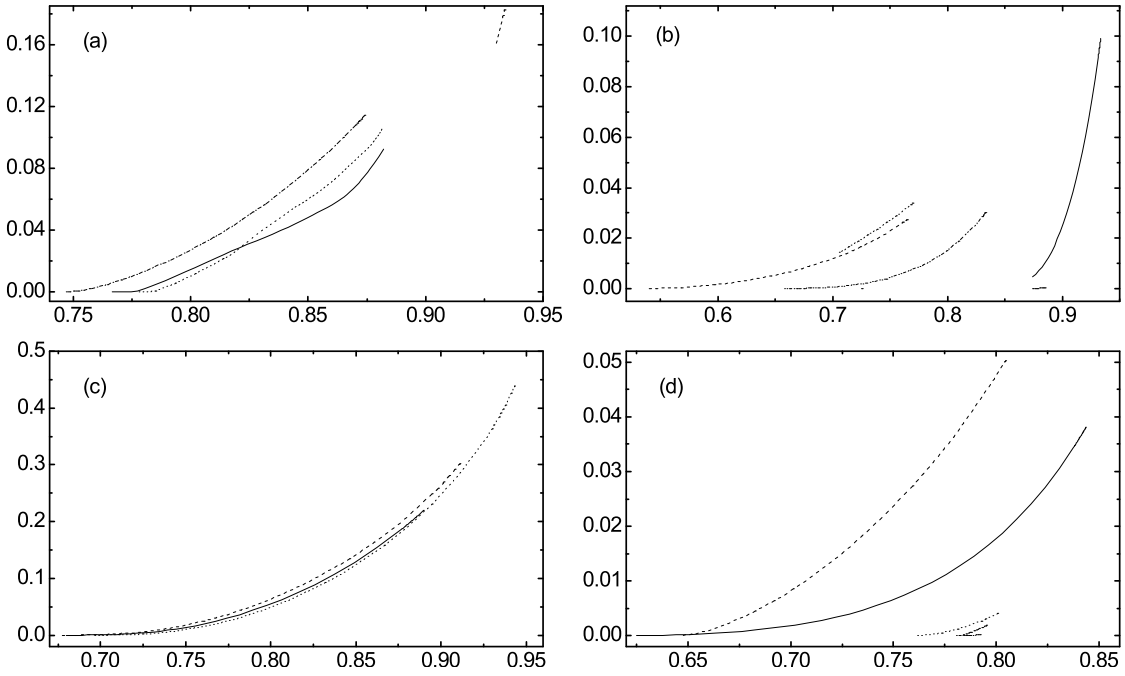


Figure 7.5: Temperature of postshock flows (Θ vs. β_1) for the flow types: (a) Type I, (b) Type II, (c) Type II ($\sigma_1 < 0$), (d) Type III.

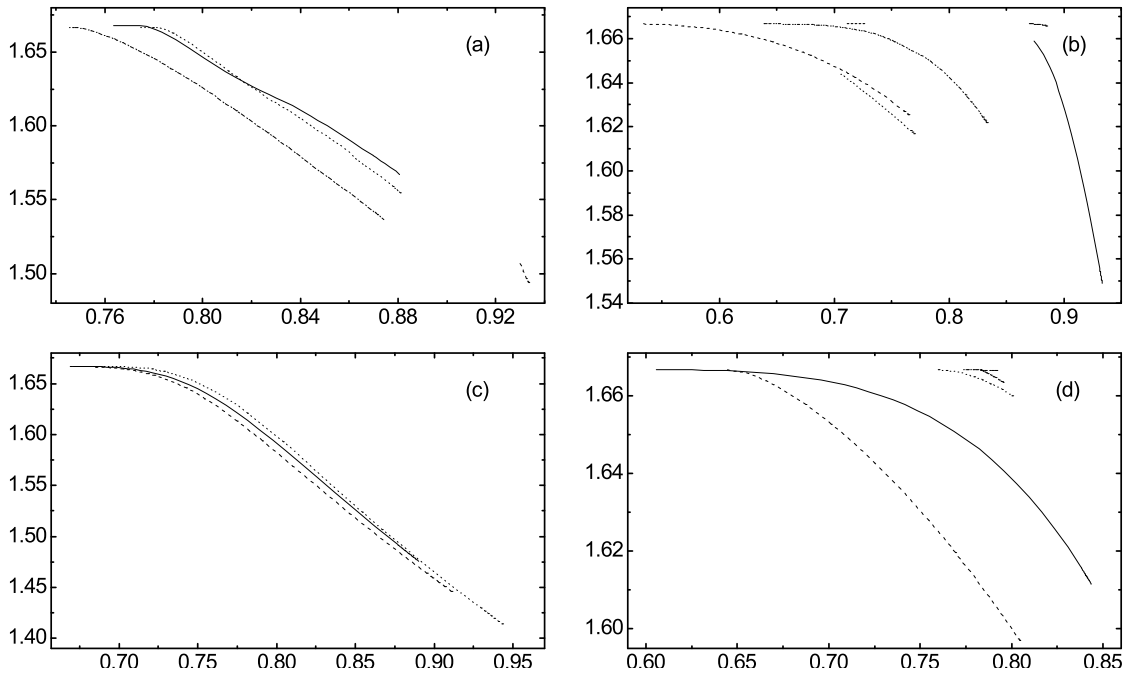


Figure 7.6: Polytropic index of postshock flows (Γ vs. β_1) for the flow types: (a) Type I, (b) Type II, (c) Type II ($\sigma_1 < 0$), (d) Type III.

4. "... q exceeds the compression ratio in fast shocks."

   We find that for all fast shocks, $q > \xi$, in agreement with A&C.

5. "The temperature in units of the rest mass turns out to be only marginally affected for the choice of parameters under consideration and does not differ from the [hydrodynamic case]."

   The postshock plasma temperatures produced by fast shocks are generally less than that for slow shocks. This is not surprising – for fast shocks some of the kinetic energy must be converted into magnetic energy while for slow shocks both kinetic and magnetic energy is available for heating. The choice of initial conditions usually has very little effect on the temperatures obtained. The exception is a Type II {a1, a2, a3} flow for which a high temperature can be obtained by choosing parameters

that give both a large radial velocity and a near head-on propagation direction – a more violent "collision" with the shock front causes more heating.

6. "The same applies to the polytropic index, which is a (nonlinear) measure of the temperature. Despite the high temperatures that can be reached at high jet velocities, $\Gamma = 4/3$ is not a good approximation, even for very high β_1."

   We agree with A&C. Even more so than for slow shocks, $\Gamma = 4/3$ is not a good approximation. This is not surprising because the radial velocities for fast shocks are not extremely relativistic.

7. "The thresholds ... come from the fact that for a fast shock to occur the fast magnetosonic Mach number has to exceed unity..."

   The thresholds A&C are referring to are the minimum speeds possible for shocks to take place. For their initial conditions they have the preshock velocity as small as $\beta_1 \approx 0.033$. Because of azimuthal velocities, we generally have a much larger preshock flow threshold, $\beta_1 \geq 0.5$. But our threshold radial velocities are similar to A&C's.

CHAPTER 8

CONCLUSION

'I like to have a thing suggested rather than told in full. When every detail is given, the mind rests satisfied, and the imagination loses the desire to use its own wings.' – T. B. Aldrich

Summary

The launch in 1970 of the x-ray satellite observatory *Uhura* began the era of cosmic x-ray astronomy. Since then, several other satellites including, for example, *ASCA* and *ROSAT*, have truly opened the window to the inner workings of AGN. Our view has been made even more clear in recent years with data from the new x-ray telescopes *Chandra* and *XMM-Newton*. These telescopes have been able to directly observe an x-ray source above an accretion disk surrounding a SMBH, although the precise nature of this source has yet to be determined. Future satellites, such as the *Constellation-X Mission* and *ASTRO-2E*, will have even greater resolution and allow further refinement of the current theories of AGN engines.

The research in this dissertation has focused on the feasibility of standing MHD shocks in the vicinity of a rotating black hole. Using a relatively simple model, both slow and fast magnetosonic shocks were shown to be possible in accreting plasma. While this is by no means evidence of their existence, it is a necessary feasibility check. The modelled shocks can occur over a wide spatial range, both polar and radial. They can also have a

wide range in strength, with the concomitant heating of the shocked flow. The resultant hot spot could be the source of X-rays illuminating the accretion disk.

In addition to verifying the theoretical existence of MHD shocks in the local neighborhood of a SMBH, a detailed analysis of the accretion flow in a Kerr spacetime produced shock categories. These categories are based on the background spacetime and the properties of the preshock flow. By using the flow's conserved quantities, the general properties of the shock, a local phenomenon, can be predicted from the initial conditions of the flow at its source.

Future Work

There is much work that remains to be done to make this model more viable and there are many logical extensions. Of most importance is the extension of our model to include hot plasma flow. Although we accept only valid cold preshock flows, in the sense that they correctly go through the critical points, it is not known if the hot postshock flow is valid. That is, we can not check to ensure that the postshock flow correctly goes through its critical points and arrives at the horizon. Algorithms for this extension have been developed but have not yet implemented. Including this additional step would advance the model in three ways: (1) as mentioned, the hot postshock flow could be checked for consistency, thereby eliminating some of the parameter space and possibly restricting shock locations, (2) perhaps allowing for *invalid* cold preshock flows; this would give accretion solutions that required a shock to occur, (3) both hot preshock and postshock flows could be modelled, the most general condition.

Our model consists only of adiabatic shocks. The model could be extended to isothermal shocks which would allow for radiation to be generated at the shock itself. Xu & Forbes (1991) studied slow-mode MHD shocks in a solar plasma where both thermal conduction and radiation were important. Our model consists of an infinitely thin shock front. Allowing a shock with finite thickness would allow for an investigation of particle acceleration at the shock as in Kirk & Duffy (1999), Kirk et al. (2000) and Isenberg (1986).

A shock stability analysis has not yet been conducted. This is perhaps not a critical issue because the iron line profiles observed have a great deal of time variability. So in the chaotic region near the horizon of a black hole, radiative MHD shocks could form and dissipate intermittently. A rigidly-rotating magnetic monopole magnetosphere has been assumed throughout. Other field configurations, such as a simple dipole, could be assumed. While no simple magnetic configuration would be realistic, qualitative differences could be instructive.

Other considerations include the type of plasma; Hartquist et al. (2000) has a review of recent work on multifluid MHD models of oblique shocks in weakly ionized regions. Krolik (1999) discusses the general assumptions that went into our model, including axisymmetry and stationarity. He concludes that both of these symmetries will have to be dropped to obtain a realistic description of the inner regions of a magnetosphere. But he also concludes that the assumption of purely hydrodynamic flow is always inappropriate.

Based on the topics mentioned in this section, it appears likely that any realistic model of MHD shocks in an accreting plasma around a SMBH will necessarily be a numerical model. But there are modifications, both simple and complicated, that can extend the usefulness of our approach. So an analytic model should remain a useful benchmark in

the future.

APPENDICES

APPENDIX A

DERIVATION OF TYPE II SHOCK PROPERTIES

Appendix A

DERIVATION OF TYPE II SHOCK PROPERTIES

In Chapter 2, categories for types of accretion flows and shocks for those flow types were discussed. Here a detailed derivation of those properties for Type II shocks is given.

1. For slow shocks: $q < 1$.

2. Given $1 - \zeta = \sigma_1(q - 1)$ then

$$\sigma_1 > 0 \rightarrow \zeta > 1$$

$$\sigma_1 < 0 \rightarrow \zeta < 1 \ .$$

3. A slowly rotating magnetosphere ($\Omega_F < \omega_H$) means $B_\phi > 0$. From

$$B_\phi = 4\pi\eta \frac{E}{M^2 - \alpha}(G_\phi + G_t\tilde{L}),$$

we have, with $M^2 - \alpha < 0$,

$$E > 0 \rightarrow G_\phi + G_t\tilde{L} > 0$$

$$E < 0 \rightarrow G_\phi + G_t\tilde{L} < 0 \ .$$

4. From

$$\sigma = \frac{B_\phi}{4\pi\eta\mu u^t}\frac{G_\phi}{\rho_\omega^2} \ ,$$

we have

$$\sigma_1 > 0 \rightarrow G_\phi > 0$$

$$\sigma_1 < 0 \rightarrow G_\phi < 0 \ .$$

5. By definition, $G_\phi \equiv g_{t\phi} + g_{\phi\phi}\Omega_F = g_{\phi\phi}(\Omega_F - \omega)$ with $g_{\phi\phi} < 0$ due to the metric signature. Then

$$G_\phi > 0 \rightarrow \Omega_F < \omega$$

$$G_\phi < 0 \rightarrow \Omega_F > \omega \ .$$

6. The magnetization parameter can be written as

$$\sigma = \frac{B_\phi^2}{4\pi\mu n (u^t)^2} \frac{-g_{\phi\phi}(\Omega_F - \omega)}{(\rho_\omega^2)^2(\Omega_F - \Omega)} \ .$$

Then

$$\sigma_{1,2} > 0 \rightarrow \Omega_F < \Omega_{1,2}$$

$$\sigma_{1,2} < 0 \rightarrow \Omega_F > \Omega_{1,2} \ .$$

7. From $\Omega_2 = \Omega_F + (q/\xi)(\Omega_1 - \Omega_F)$ we obtain $\Omega_2 - \Omega_1 = (\Omega_F - \Omega_1)(1 - q/\xi)$. But

$q/\xi < 1$ giving $(1 - q/\xi) > 0$. So

$$\Omega_F > \Omega_1 \rightarrow \Omega_2 > \Omega_1$$

$$\Omega_F < \Omega_1 \rightarrow \Omega_2 < \Omega_1 \ .$$

There is now enough information to put Type II slow shocks ($q < 1$, $\Omega_F < \omega_H$, $B_\phi > 0$) with $a \geq 0$ into three categories, determined by the sign of G_ϕ, a function of geometry and magnetosphere angular velocity only (the special case of $G_\phi = 0$ is obvious):

1. $G_\phi > 0$: Then $\zeta > 1$, $\sigma_{1,2} > 0$ and $0 < \Omega_F < \Omega_2 < \Omega_1 \gtrless \omega < \omega_H$.

2. $G_\phi < 0$: Then $\zeta < 1$, $\sigma_{1,2} < 0$ and $0 < \omega < \Omega_F < \Omega_2 < \Omega_1 < \omega_H$.

3. $G_\phi = 0$: Then $\zeta = 1$, $\sigma_{1,2} = 0$ and $\omega = \Omega_F$.

APPENDIX B

SWITCH-OFF SHOCKS

Appendix B

SWITCH-OFF SHOCKS

Switch-off shocks were discussed in Chapter 6. This appendix lists the equations, derived by Takahashi (2002b), used to calculate the results listed in Table 6.3. In the switch-off shock case, $M_1^2 \to \alpha_A$, $(r_{sh} \to r_A)$ but $M_2^2 < \alpha_A$. In this limit[1] the following limits for shock parameters are obtained:

$$q \equiv \frac{B_{\phi 2}}{B_{\phi 1}} = \frac{M_1^2 - \alpha}{M_2^2 - \alpha} \to 0 \ , \tag{B.1}$$

$$\zeta = \frac{e - hM_2^2}{e - hM_1^2} q \ \to \left[\left(\frac{L}{E} \right) G_{tA}^2 \left(\frac{-f_1}{\rho_w} \right)_A + 1 \right]^{-1} \equiv \zeta_A \ , \tag{B.2}$$

$$\xi = \frac{M_1^2}{M_2^2} \zeta \to \frac{\alpha_A}{(M_2^2)_A} \zeta_A \equiv \xi_A > \zeta_A \ , \tag{B.3}$$

$$\sigma_1 = -\frac{e - h\alpha}{e - hM_1^2} \to \frac{-G_{\phi A} E f_{1A}}{G_{\phi A} E f_{1A} + (h\rho_w)_A} \ , \tag{B.4}$$

$$\Pi \equiv \frac{P_1 - P_2}{n_1 \mu_1 (u^r u_r)_1} = \left(1 - \frac{M_2^2}{M_1^2} \right) - \frac{(q^2 - 1)\sigma_1}{2} \left(\frac{u_t}{u^r} \right)_1^2 \frac{\rho_w^2 (\Omega_1 - \Omega_F)}{g_{rr} g_{\phi\phi} (\Omega_F - \omega)} \tag{B.5}$$

$$\to \frac{\alpha_A - (M_2^2)_A}{\alpha_A} + \frac{1}{2} \left(\frac{E}{\mu_c} \right)^2 \left[\frac{(1 - \Omega_F \rho_w f_1)^2 \rho_w^2}{(-u_r u^r)_1 g_{\phi\phi}} \frac{(\Omega_1 - \Omega_F)}{(\Omega_F - \omega)} \right]_A \equiv \Pi_A \tag{B.6}$$

$$\Theta = (-u_r u^r)_1 \left(\frac{u_2^t}{u_1^t} \right) \frac{\Pi}{\xi} \to (-u_r u^r)_{1A} \left(\frac{u_{2A}^t}{u_{1A}^t} \right) \frac{\Pi_A}{\xi_A} \equiv \Theta_A \tag{B.7}$$

[1] It is not certain that the jump conditions are still satisfied in the limit of a switch-off shock. Therefore, the equations presented in this appendix may give only the tendency of shock behavior in this limiting case.

APPENDIX C

KERR SPACETIME, ZAMO'S AND UNITS

Appendix C

KERR SPACETIME, ZAMO'S AND UNITS

This appendix describes the Kerr spacetime, defines ZAMOs and gives a table of the dimensions of many variables in natural units.

Kerr Geometry

The Kerr metric in Boyer-Lindquist coordinates, signature {+,-,-,-} and $c = G = 1$ is

$$ds^2 = (1 - \frac{2mr}{\Sigma})dt^2 + \frac{4marsin^2\theta}{\Sigma}dtd\phi - \frac{Asin^2\theta}{\Sigma}d\phi^2 - \frac{\Sigma}{\Delta}dr^2 - \Sigma d\theta^2 \quad , \tag{C.1}$$

where $\Delta \equiv r^2 - 2mr + a^2$, $\Sigma \equiv r^2 + a^2cos^2\theta$, $A \equiv (r^2 + a^2)^2 - a^2\Delta sin^2\theta$. This metric is stationary and axisymmetric about the polar axis, $\theta = 0$. The square root of the determinant is $\sqrt{-g} = \Delta \sin\theta$. The outer horizon, r_H is given by

$$r_H = m + \sqrt{m^2 - a^2} \ , \tag{C.2}$$

and the static limit, or outer boundary of the ergosphere, is the solution of $g_{tt} = 0$ and given by

$$r_{\rm st} = m + \sqrt{m^2 - a^2\cos^2\theta} \ . \tag{C.3}$$

Between the static limit and the horizon lies the ergosphere. Within this region a static observer (with zero angular velocity with respect to the "fixed stars") cannot exist. A side view of the ergosphere is shown in Figure B.1. (Note: the standard schematic of

an ellipse tangent to a circle that is usually shown is incorrect.)

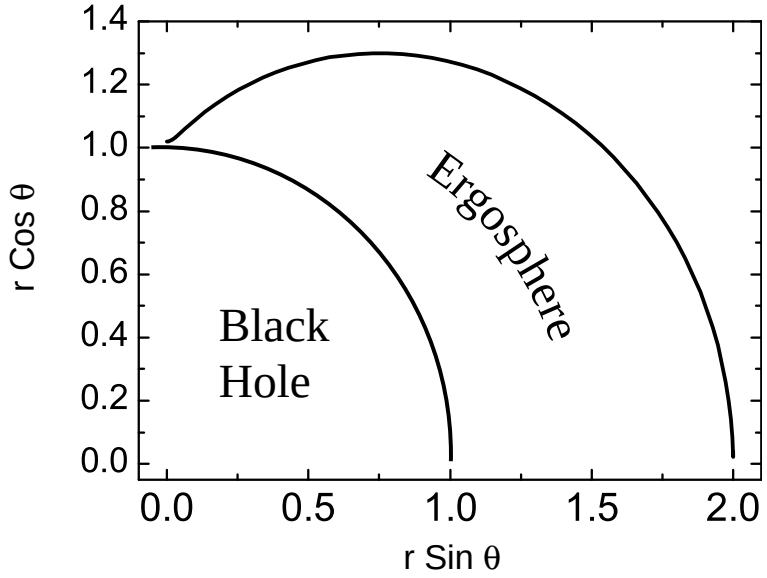


Figure C.1: The ergosphere for $a = 0.9998$. At the polar axis, the static limit curve is tangent to the horizon.

The locally nonrotating frame (LNRF) introduced by Bardeen (1970) forms the basis for a zero angular momentum observer (ZAMO). The ZAMO's worldlines are r = constant, θ = constant, $\phi = \omega\ t +$ constant. Such an observer will have an angular momentum $\omega = u^\phi/u^t = -g_{t\phi}/g_{\phi\phi}$, relative to infinity. The orthonormal tetrad carried by such an observer at the point (t, r, θ, ϕ) is given by

$$e_{\hat{t}} = A^{1/2}(\Delta\Sigma)^{-1/2}[1, 0, 0, \omega] \tag{C.4}$$

$$e_{\hat{r}} = [0, \Delta^{1/2}\Sigma^{-1/2}, 0, 0] \tag{C.5}$$

$$e_{\hat{\theta}} = [0, 0, \Sigma^{-1/2}, 0] \tag{C.6}$$

$$e_{\hat{\phi}} = [0, 0, 0, A^{-1/2}\Sigma^{1/2}\sin^{-1}\theta] \tag{C.7}$$

The time component of the four-velocity can then be read directly (or obtained from

four-velocity normalization)

$$u_z^t = \left(\frac{A}{\Delta\Sigma}\right)^{1/2} \quad . \tag{C.8}$$

A ZAMO will measure the energy of the fluid to be

$$E_z = u_z^t(E - \omega L) \ , \tag{C.9}$$

where the subscript (or superscript) 'z' will be used to denote a ZAMO quantity. This energy is positive definite so that $E > \omega L$.

The total energy and angular momentum of the accreting fluid, defined in Chapter 2, equations (2.30) and (2.31), can be separated into fluid and magnetic components and written in the ZAMO frame:

$$E = \mu u_t - \frac{\Omega_F B_\phi}{4\pi\eta} \qquad E_F = \mu u_t \qquad E_M = -\frac{\Omega_F B_\phi}{4\pi\eta} \tag{C.10}$$

$$L = -\mu u_\phi - \frac{B_\phi}{4\pi\eta} \qquad L_F = -\mu u_\phi \qquad L_M = -\frac{B_\phi}{4\pi\eta} \tag{C.11}$$

The fluid and magnetic components for both the preshock and postshock flow are then

$$E_{F1}^z = \mu_1 u_z^t(u_{t1} + \omega u_{\phi 1}) \qquad E_{M1}^z = u_z^t\left(\frac{\Omega_F B_{\phi 1}}{4\pi\eta}\right)(\omega - \Omega_F) \tag{C.12}$$

$$E_{F2}^z = \mu_2 u_z^t(u_{t2} + \omega u_{\phi 2}) \qquad E_{M2}^z = u_z^t\left(\frac{\Omega_F B_{\phi 2}}{4\pi\eta}\right)(\omega - \Omega_F) \tag{C.13}$$

The fractional energy components are then E_{Fi}^z/E_z and E_{Mi}^z/E_z where $i = (1, 2)$ refer to the preshock and postshock flows, respectively.

Table C.1: Dimensions of many quantities.

Fluid Quantities				
$[n] = cm^{-3}$	$[\mu] = cm$	$[\rho] = cm^{-2}$	$[P] = cm^{-2}$	$[m_p] = cm$
$[u^t] = 1$	$[u^r] = 1$	$[u^\theta] = cm^{-1}$	$[u^\phi] = cm^{-1}$	
$[u_t] = 1$	$[u_r] = 1$	$[u_\theta] = cm$	$[u_\phi] = cm$	
$[T^{tt}] = cm^{-2}$	$[T^{tr}] = cm^{-2}$	$[T^{rr}] = cm^{-2}$		
$[T^{t\theta}] = cm^{-3}$	$[T^{t\phi}] = cm^{-3}$	$[T^{r\theta}] = cm^{-3}$	$[T^{r\phi}] = cm^{-3}$	
$[T^{\theta\phi}] = cm^{-4}$	$[T^{\theta\theta}] = cm^{-4}$	$[T^{\phi\phi}] = cm^{-4}$		
$[\Gamma] = 1$	$[\Omega] = cm^{-1}$	$[\sigma] = 1$	$[\Theta] = 1$	
Metric and Related Terms				
$[g_{tt}] = 1$	$[g_{rr}] = 1$	$[g_{\theta\theta}] = cm^2$	$[g_{\phi\phi}] = cm^2$	$[g_{t\phi}] = cm$
$[g^{tt}] = 1$	$[g^{rr}] = 1$	$[g^{\theta\theta}] = cm^{-2}$	$[g^{\phi\phi}] = cm^{-2}$	$[g^{t\phi}] = cm^{-1}$
$[\Delta] = cm^2$	$[\Sigma] = cm^2$	$[A] = cm^4$	$[\rho_w^2] = cm^2$	$[g] = cm^4$
$[\omega] = cm^{-1}$	$[\alpha] = 1$	$[G_t] = 1$	$[G_\phi] = cm$	$[m_{BH}] = cm$
Magnetosphere Quantities				
$[F_{tr}] = cm^{-1}$	$[F_{t\theta}] = 1$	$[F_{t\phi}] = cm^{-1}$	$[F_{r\theta}] = 1$	$[F_{r\phi}] = 1$
$[F_{\theta\phi}] = cm$	$[F^{tr}] = cm^{-1}$	$[F^{t\theta}] = cm^{-2}$	$[F^{t\phi}] = cm^{-3}$	$[F^{r\theta}] = cm^{-2}$
$[F^{r\phi}] = cm^{-2}$	$[F^{\theta\phi}] = cm$			
$[B_t] = 1$	$[B_r] = cm^{-1}$	$[B_\theta] = 1$	$[B_\phi] = 1$	$[B_p] = cm^{-1}$
$[B^t] = 1$	$[B^r] = cm^{-1}$	$[B^\theta] = cm^{-2}$	$[B^\phi] = cm^{-2}$	$[B_I] = cm^{-1}$
Shock Variables				
$[\xi] = 1$	$[\zeta] = 1$	$[q] = 1$		
Conserved Quantities				
$[E] = cm$	$[L] = cm^2$	$[\Omega_F] = cm^{-1}$	$[\eta] = cm^{-2}$	

BIBLIOGRAPHY

Bibliography

Anderson, J. 1982, *Modern Compressible Flow, with Historical Perspective* (McGraw-Hill)

Anile, A. M., Miller, J. C. & Motta, S. 1983, Phys. Fluids, 26, 1450

Appl, S. & Camenzind, M., 1988, A&A, 206, 258

Ardavan, H. 1976a, ApJ, 203, 226

Ardavan, H. 1976b, ApJ, 206, 822

Babul, A., Ostriker, J., & Mészáros, P. 1989, ApJ, 3437, 59

Bardeen, J. 1970, ApJ, 162, 71

Begelman, Blandford & Rees 1984, Rev. Mod. Phy., 56, 255

Bekenstein, J. D. & Oron, E. 1978, Phys. Rev. D, 18, 1809

Beskin, V. S., Istomin, Ya. N. & Par'ev, V. I. 1992 Sov. Astron. 36, 642

Beskin, V. S. 1997, Phys. Uspekhi, 40, 659

Beskin, V. S., Kuznetsova, I. V. & Rafikov, R. R. 1998, MNRAS, 299, 341

Beskin, V. S., Kuznetsova, I. V. 2000, Il Nuovo Cimento B, 115, 795

Beskin, V. S., Istomin, Ya. N. & Par'ev, V. I. 1992, Astronomicheskij Zhurnal, 69, 1258

Blandford, R. D. & Znajek, R. L. 1977, MNRAS, 179, 433

Blandford, R. D. & McKee, C. F. 1976, Phys. Fluids 19, 1130

Bondi, H. 1952, MNRAS, 112, 195

Bregman et al. 1990, ApJ, 352, 574

Camenzind, M. 1986a, A&A, 156, 137

Camenzind, M. 1986b, A&A, 162, 32

Camenzind, M. 1987, A&A, 184, 341

Camenzind, M. 1989, in *Accretion Disks and Magnetic Fields in Astrophysics*, ed. G. Belvedere (Dordrecht: Kluwer), P.129

Chang, K. & Ostriker, J. 1985, 288, 428

Chakrabarti, S. K. 1989, ApJ, 347, 365

Chakrabarti, S. K. 1990a, ApJ, 350, 275

Chakrabarti, S. K. 1990b, MNRAS, 246, 134

Christodoulou, R. & Ruffini, R. 1971, Phys. Rev. D, 4, 3552

De Sterck, H., Low, B.C. & Poedts, S. 1998, Phys. Plasmas, 5, 4015

De Sterck, H. & Poedts, S. 2000, Phys. Rev. Lett., 84, 5524

Draine, B. T. 1993, Ann. Rev. Astron. Astrophys., 31, 373

Emmering, R. T. & Chevalier, R. A. 1987, ApJ, 321, 334

Fendt, C. & Greiner, J. 2001, A&A, 369, 308

Fukue, J. 1987, PASJ, 39, 309

Gammie, C., Shapiro, S., McKinney, J. 2003, astro-ph/0310886

Ghisellini, G., Haardt, F. & Svensson, R. (1998), MNRAS, 297, 348

Goldreich, P. & Julian, W.H. 1969, ApJ, 157, 869

Haardt, F. & Maraschi, L., ApJ, 413, 507

Hartquist, T. W., Dyson, J. E. & Williams, R. J. R. 2000, Astrophysics and Space Science, 272, 163

de Hoffman, F. & Teller, E. 1950, Phys. Rev., 80, 692

Heinrich, F. & Rohde, C. 2003, Physica D, in press

Helfer, H. L. 1953, ApJ, 117, 177

Hirotani, K., Takahashi, M., Nitta, S. & Tomimatsu, A., 1992, ApJ, 386, 455

Hirotani, K. & Okamoto, I. 1998, ApJ, 497, 563

Horiuchi, L., Mestel, L., & Okamoto, I. 1995, MNRAS, 275, 1160

Isenberg, P. A. 1986, J. Geophys. Res., 91, 1699

Israel, W. 1963, J. Math. Phys., 4, 1163

Iwasawa, K., et al. 1996, MNRAS, 282, 1038

Johnson, H. E. & Axford, W.I. 1971, ApJ, 165, 381

Karas, V. 1989, Phys. Rev. D, 40, 2121

Khanna, R. 1998a, MNRAS, 294, 673

Khanna, R. 1998b, MNRAS, 295, L6

Jüttner, F. 1911, Ann. Phys., 34, 856

Kennel, C. F., Fujimura, F., Okamoto, I. 1983, Geophys. Astrophys. Fluid Dyn., 26, 147

Kennel, C. F. & Coroniti, F. V. 1984, ApJ, 283, 694

King, A. R., Lasota, J.P. & Kundt, W. 1975, Phys. Rev. D, 12, 3037

Königl, A. 1980, Phys. Fluids, 23, 1083

Kirk, J. G. & Duffy, P. 1999, J. Phys., G25, R163

Kirk, J. G., Guthmann, A. W., Gallant, Y. A., & Achterberg, A. 2000, ApJ, 542, 235

Koide, S. 2003, Phys. Rev. D, 67, 104010

Komissarov, S.S. 2001, MNRAS, 326, L41

Komissarov, S.S. 2003, MNRAS, 341, 717

Kormendy, J. & Richstone, D., ARA&A, 33, 581

Krolik, J. 1999, ApJ, 515, L73

Kundt, W. & Krotscheck, E. 1982, Astron. Astrophys. 206, 258

Kuwahara, F. 1989, Prog. Theor. Phys. 81, 549

Landau, L. D. & Lifshitz, E. M. 1959, *Fluid Mechanics* (Oxford: Pergamon Press)

Landau, L. D. & Lifshitz, E. M. 1985, *Electrodynamics of Continuous Media, 2ed.* (Oxford: Pergamon Press)

Lanza, A., Miller, J.C. & Motta, S. 1985, Phys. Fluids, 28, 97

Lichnerowicz. A. 1967, *Relativistic Hydrodynamics and Magnetohydrodynamics* (New York: Benjamin Press)

Liang, E.P.T. 1977, ApJ, 211, 361

Lightman, A. P., Press, W. H., Price, R. H. & Teukolsky, S. A. 1975, *Problem Book in Relativity and Gravitation* (Princeton: Princeton University Press)

Lu, J.-F. 1986, Gen. Rel. Grav. 18, 45

Lu, J.-F., Yu, K. N., Yuan, F. & Young, E. C. M. 1997, A&A, 321, 665

Lu, J.-F. & Yuan, F. 1998, MNRAS, 295, 66

Maia, M.A.G., Machado, R.S. & Willmer, C.N.A., RevMexAA, 14, 77

Maraschi, L. & Haardt, F. 1996, in *IAU Colloquium 163: Accretion Phenomena and Related Outflows*

McCrea, W. H. 1956, ApJ, 124, 461

Merloni, A. & Fabian, A. C., MNRAS, 342, 951

Michel, F. C. 1969, ApJ, 158, 727

Michel, F. C. 1973a, ApJ, 180, 207

Michel, F. C. 1973b, ApJ, 180, L133

Moderski, R. & Sikora, M. 1996, MNRAS, 283, 854

Nandra, K., George, I. M., Mushotzky, R. F., Turner, T.J. & Yaqoob, T. 1997, ApJ, 488, 91

Nitta, S., Takahashi, M. & Tomimatsu, A., 1991, Phys. Rev. D, 44, 2295

Okamoto, I. 1992, MNRAS, 254, 192

Papadopolous, K. 1998, Ap&SS, 144, 535

Peterson, B. 1997, *An Introduction to Active Galactic Nuclei* (Cambridge: Cambridge University Press)

Petrucci, P. O., Merloni, A., Fabian, A., Haardt, F. & Gallo, E., MNRAS, 328, 501

Phinney, E.S. 1983, Ph.D. thesis, Univ. Camnridge

Punsly, B. & Coroniti, F. V. 1990, ApJ350, 518

Punsly, B. & Coroniti, F. V. 1990, ApJ354, 583

Punsly, B., 2001, *Black Hole Gravitohydrodynamics* (New York: Springer-Verlag)

Punsly, B. 2003, ApJ, 583, 842

Rankine, W. 1870, Philos. Trans. part II, 160, 277

Rees, 1998, in *Black Holes and Relativistic Stars*, ed. R. M. Wald (Chicago: Univ. of Chicago Press), 83

Reynolds, C. S. & Begelman, M. C. 1997, ApJ, 488, 109

Reynolds, C. S. & Nowak, M. 2003, Physics Reports, 377, 389

Ruffini, R. & Wilson, J. 1975, Phys. Rev. D, 12, 2959

Sakurai, T. 1985, A&A, 152, 121

Schutz, B. 1985, *A First Course in General Relativity* (Cambridge: Cambridge University Press)

Scudder, J.D. 1995, Adv. Space Res., 15, 181

Service, A. T. 1986, ApJ, 307, 60

Shimada, N. & Hoshino, M. 2000, ApJ, 543, L67

Sponholz, H. & Molteni, D. 1994, MNRAS, 271, 233

Synge, J. L. 1957, *The Relativistic Gas* (Amsterdam: North Holland)

Takahashi, M., Nitta, S., Tatematsu, Y. & Tomimatsu, A. 1990, ApJ, 363, 206

Takahashi, M. 2000, Il Nuovo Cimento, 115, 843

Takahashi, M. 2000, in *Highly Energetic Physical Processes and Mechanisms for emission form Astrophysical Plasmas, IAU Symposium 195*, edited by P.C. H Martens, S. Tsuruta and M. A. Weber (ASP Conference Series)

Takahashi, M., Rilett, D., Fukumura, K. & Tsuruta, S. 2002, ApJ, 572, 950

Takahashi, M. 2002, ApJ, 570, 264

Takahashi, M. 2000, private communication

Tanaka, Y., et al. 1995, Nature, 375, 659

Taub, A. H. 1948, Phys. Rev., 74, 328

Taylor, B. 1995, *Guide for the Use of the International System of Units* , NIST Spec. Pub. 811, US Govt. Printing Office, Washington, DC

Thorne, K. S. 1973, ApJ, 179, 897

Thorne, K. S. 1974, ApJ, 191, 507

Thorne, K. S., Price, R. H. & Macdonald, D. A., eds. 1986, *Black Hole: The Membrane Paradigm* (New Haven: Yale Univ. Press)

Tokar, R.L., Aldrich, C.H., Forslund, D.W. & Quest, K.B., Phys. Rev. Lett., 56, 1059

Tomimatsu, A. & Takahashi, M. 2001, ApJ, 552, 710

Tomimatsu, A., Matsuoka, T. & Takahashi, M. 2001, Phys. Rev. D, 64, 123003

Uchida, T. 1997, Phys. Rev. E, 56, 2181

Uchida, T. 1997, Phys. Rev. E, 56, 2198

Wald, R. M. 1974, Phys. Rev. D, 10, 1680

Wald, R. 1984, *General Relativity* (Chicago: University of Chicago Press)

Weber, E. & Davis, L. 1967, ApJ, 148, 217

Williams, R. J. R., Dyson, J. E. & Hartquist, T. W. 1999, Astron. Astrophys., 344, 675

Wilms, J., Reynolds, C., Begelman, M., Reeves, J., Molendi, S., Staubert, R., Kendziorra, E., 2001, 328, L27

Wilson, J. 1972, ApJ, 173, 431

Wu, C.C. & Kennel, C.F. 1992, Phys. Rev. Lett., 68, 56

Xu, P. & Forbes, T. G. 1991, Sol. Phys., 139, 315

Yokosawa, M. 1993, PASJ, 45, 207

Yokosawa, M. 1994, PASJ, 46, 73

Zhang, X.-H. 1989, Phys. Rev. D, 39, 2933

Znajek, R. L. 1977, MNRAS, 179, 457